Experimental and Computational Study of High-energy Radiotherapy Effects on Cardiac Implantable Electronic Devices with CR39 and MCNP

Tesi di Laurea Magistrale in
Nuclear Engineering - Ingegneria Nucleare

Author: **Antonella Mele**

Student ID: 944929
Advisor: Prof. Marco Caresana
Co-advisor: Dott. Matteo Bolzonella
Academic Year: 2020-21

Abstract

Cardiac Implantable Electronic Devices (CIEDs) are nowadays widely used as therapy for patients suffering from cardiovascular diseases. However, it has been experimentally observed that the secondary phototoneutron field produced by linear accelerators (LINACs) during high-energy radiotherapy treatments (>10 MV) can induce serious malfunctions in them.

The purpose of the present thesis work is, therefore, to characterize the secondary radiation field generated by two different LINACs (Varian Clinac DHX™ and Elekta Synergy®) through measurements of thermal neutron fluence in the region where the cardiac device is usually implanted. Accordingly, an experimental measurement campaign was carried out at the 'Ospedale di Circolo e Fondazione Macchi' in Varese (IT) where a *Varian Clinac DHX* is installed, at the 'Azienda sanitaria universitaria Giuliano Isontina (ASUGI)' in Trieste (IT) and at the 'San Luca' hospital in Lucca (IT), both housing a *Elekta Synergy 3028* linear accelerator. Realistic treatment plans were simulated on a BOMAB-like phantom inside which nuclear track detectors in CR39 coupled to boron carbide converters with 99% B-10 enrichment were arranged and used to estimate the quantity of interest. In addition to that, some measurements were performed aimed at studying the spatial distribution of neutron fluence along the axis of the phantom.

At the same time, a computational model of the *Elekta Synergy* accelerator head and the treatment room of ASUGI was extended with the addition of a phantom designed to reproduce the one used in the experiments and aimed at simulating the patient's body. This model is based on the Monte Carlo MCNP 6.2 code.

From the comparison between experimental results and data reported in the literature, it appears that the thermal neutron fluence, to which a patient is exposed during a complete course of radiotherapy, does not reach values for which it is has been experimentally demonstrated that there may be a permanent damage to the cardiac device ($\sim 10^9 \frac{\text{n}}{\text{cm}^2}$), at least in the treatments investigated in this work. Moreover, it has been shown both experimentally and through computer simulations that the neutron spectrum does not significantly vary if measured at different points within the phantom, even modifying the

irradiation conditions.

Keywords: CIED, radiotherapy, LINAC, solid-state nuclear track detectors, CR39, MCNP.

Estratto in lingua italiana

I dispositivi cardiaci elettronici impiantabili, noti con l'acronimo di CIED, sono oggigiorno largamente utilizzati come terapia per i pazienti con malattie cardiovascolari. È stato, tuttavia, osservato sperimentalmente che il fascio fotoneutronico secondario prodotto dagli acceleratori lineari (LINACs) durante trattamenti radioterapici ad elevata energia (>10 MV) può indurre in essi malfunzionamenti che mettono a rischio la vita dei pazienti.

L'obiettivo del presente lavoro di tesi è, quindi, quello di caratterizzare il campo di radiazione secondaria generato da due diversi LINAC (Varian Clinac DHX™ed Elekta Synergy®) tramite misure di fluenza neutronica termica nella regione in cui il dispositivo cardiaco è solitamente impiantato. Per tale scopo è stata condotta una campagna di misure sperimentali presso l'Ospedale di Circolo e Fondazione Macchi (Varese), nel quale è installato un acceleratore dell'azienda *Varian Medical Systems* modello *Clinac DHX*, presso l'Azienda Sanitaria Universitaria Giuliano Isontina (ASUGI, Trieste) e l'Ospedale San Luca (Lucca), entrambi ospitanti un LINAC *Elekta Synergy 3028*. Sono stati, quindi, simulati dei realistici piani di trattamento su un fantoccio tipo BOMAB all'interno del quale rivelatori a tracce in CR39 accoppiati a convertitori di carbonato di boro arricchiti al 99% in ^{10}B sono stati disposti e adoperati per la stima della grandezza di interesse. Inoltre, sono state condotte delle misure volte allo studio della distribuzione spaziale della fluenza neutronica lungo l'asse del fantoccio.

Contestualmente, è stato ampliato un modello computazionale della testata dell'acceleratore *Elekta Synergy* e della sala di trattamento dell'ASUGI con l'aggiunta di un fantoccio atto a riprodurre quello utilizzato durante gli esperimenti e volto a simulare il corpo di un paziente. Tale modello si basa sul codice Monte Carlo MCNP 6.2.

Dal confronto tra i risultati sperimentali e i dati riportati in letteratura risulta che la fluenza neutronica termica, a cui un paziente è esposto durante un completo ciclo di radioterapia, non raggiunge valori per cui si è dimostrato sperimentalmente che si possano avere danni permanenti al dispositivo cardiaco ($\sim 10^9 \ \frac{\text{n}}{\text{cm}^2}$), perlomeno nei trattamenti indagati in questo lavoro. Oltre a ciò, è stato dimostrato sia sperimentalmente che tramite simulazioni al calcolatore che lo spettro neutronico non subisce importanti variazioni se

misurato in diversi punti all'interno del fantoccio, pur variando le condizioni di irraggiamento.

Parole chiave: CIED, radioterapia, LINAC, rivelatori a tracce, CR39, MCNP.

Contents

Abbiamo occhi troppo piccoli per le stelle,
eppure grandi per le singole particelle.
Tarek Iurcich

1 | Introduction

Cardiovascular disease and cancer are among the main causes of death in the world, leading to the death of tens of millions of individuals every year, according to the World Health Organization [1]. It is also quite common for the same person to be diagnosed with both pathologies, as the risk factors – like smoking, physical inactivity, and aging - are shared between the two [2]. Cardiac implantable electronic device (CIED) have been proven to be a valuable mean for treating patients with cardiovascular diseases, while radiotherapy is one of the most common solutions to tackle the spread of a tumor. The purpose of this work is to assess the effects of high-energy radiation therapy on CIEDs to provide guidelines for the treatment of patients suffering from both these pathologies.

This first chapter is the framework for the entire work since it is devoted to the theoretical review of fundamental knowledge required for a better comprehension of the following chapters. Accordingly, Section 1.1 introduces the key topic of the thesis, that is neutron interaction with matter. Section 1.2 contains an overview of radiation therapy, while Section 1.3 illustrates the reasons that have lead to the present work. Finally, Section 1.4 briefly describes a non-destructive imaging technique which exploits neutrons' properties.

1.1. Neutron interaction with matter

In 1932 a particle with roughly the same mass of proton but having no charge was discovered by Professor James Chadwick: the neutron. It is one of the main constituents of nuclei with a mass nearly 1839 times greater than that of electron, that is $1.67493 \cdot 10^{-27}$ kg. When neutrons are not bounded in an atomic nucleus they are unstable and have a mean lifetime of about 14 min. Therefore, they decay via β^- decay into a proton, an electron, and an electronic anti-neutrino:

$$n \rightarrow p^+ + e^- + \bar{\nu} \tag{1.1}$$

Generally, neutrons are subdivided into several categories on the basis of their energy [3]:

- *Thermal neutrons*: $E_n < 0.5$ eV. They are in thermal equilibrium with matter and

have a Maxwellian distribution of velocities, the most probable of which is 2200 m/s at room temperature that corresponds to an energy of 0.025 eV;

- *Epithermal neutrons*: E_n = 0.5 eV ÷ 100 keV;

- *Fast neutrons*: E_n = 100 keV ÷ 20 MeV;

- *High-energy neutrons*: E_n > 20 MeV.

Since neutrons carry no charge, they cannot interact with matter by means of the Coulomb force. However, they can penetrate the electron shell and interact on the level of the nucleus.

Neutron cross section

The neutron-nucleus interaction probability is characterized by a quantity called *nuclear cross-section* σ. It can be interpreted as the *effective cross sectional area* presented by the nucleus to the projectile (i.e. the neutron), hence the larger the effective area, the greater the probability [4, 5].

Let us consider a neutron beam of initial intensity I_0 impinging on a thin slab of material of thickness dz. The variation of $I(z)$ [#/cm²·s] along the z-axis will be described by the following equation:

$$\frac{dI}{dz} = -n\sigma I \tag{1.2}$$

where σ is the total microscopic cross section of all events that can occur, while n is the number density of nuclei in the target. Solving this equation leads to an exponential attenuation of beam intensity (Figure 1.1):

$$I = I_0 e^{-n\sigma z} \tag{1.3}$$

where the initial condition I(z)=0 at z=0 was imposed.

The SI unit of total cross section is m², but in nuclear physics the *barn* (1 b = 10⁻²⁸ m²) is commonly used, since square meter is tremendously large in comparison to the geometrical cross sectional area of a nucleus.

It is possible to derive from the previous equation another quantity known as *macroscopic cross section* Σ [cm⁻¹]:

$$\Sigma = n \cdot \sigma$$

The term 'macroscopic' comes from its physical interpretation, namely the probability (per unit path length traveled) of neutron interaction in a macroscopic slab of material
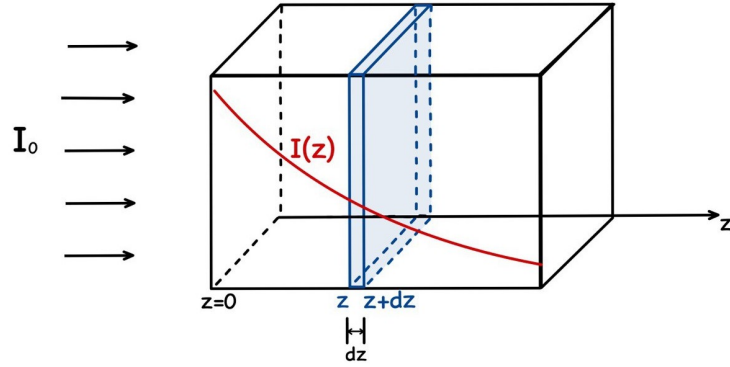
Figure 1.1: Exponential decrease of the intensity of a parallel neutron beam through a thick slab of material.

compared with the 'microscopic' cross section that stands for the probability of interaction with one single nucleus (per unit path length) [4].

Cross sections are strongly dependent on different factors such as the type of incident particle and target isotope as well as on the incoming projectile energy. However, this notion will be analyzed in much more detail in the following sections since it is exploited for neutron detection.

In order to estimate the rate of reactions induced by neutrons, it is convenient to introduce the concept of *neutron flux* φ, a scalar quantity that differs from the intensity since it stands for the number of neutrons crossing a cross-sectional unit area in *all directions* per unit time. It can be calculated multiplying the neutron density n by their velocity v [6].

Thus, the *reaction rate RR*:

$$RR = \varphi \cdot \Sigma \tag{1.4}$$

is the number of interactions taking place in one cubic centimeter per second. This relation can be generalized to include an energy-dependent neutron flux $\varphi(r, E)$ and cross section $\Sigma(E)$ [7]:

$$RR = \int_0^\infty \varphi(r, E)\Sigma(E)dE \tag{1.5}$$

In the frame of this work, a key role is played by the *fluence*, which is the integral of the flux in time or, equivalently, it can be defined as the ratio between the differential number dN of particles impinging on a a sphere centered about a point P and its differential (maximum) cross-sectional area da:

$$\Phi = \frac{dN}{da} \tag{1.6}$$

The fluence can also be correlated to neutron flux, previously defined, since it is its time integral over the exposure duration. Its unit of measure is usually cm^{-2}.

1.1.1.   Neutron interactions

Unlike protons or electrons, neutrons carry no charge hence they do not directly interact with matter through Coulomb force. As a consequence, they overcome the atomic electron shells and undergo reactions with the target nucleus. Depending on the incident particle energy, several reaction channels may open. Thermal neutrons are more likely to interact with nuclei through *elastic scattering* (n,n) and *absorption reactions*. The first process is a billiard ball type of collision in which the system has the same total kinetic energy before and after the collision, hence the nucleus is left in its initial state. Elastic scattering may occur also at higher energies and for all kind of nuclei. It is the main process through which fast neutrons are slowed down, especially when they collide with with nuclei in low-Z targets, such as hydrogen, since the interaction results in a higher energy transfer.

The second process consists in the absorption of the neutron by the target nucleus ^{A}Z and the *compound nucleus* formation $^{A+1}$Z. Thereafter, it can decay in several ways, which are considered to be independent of its formation modality. For example, radiative capture reactions (n, γ) fall in this category: the compound nucleus returns to its ground state by emitting a neutron and one or more γ-rays.

Radiative capture cross sections show a characteristics trend which is largely exploited in the design of neutron detectors, included the one used in this work, and that can be observed in Figure 1.2. We can distinguish three main regions. In the first one, it decreases as the neutron's energy increases following a $1/\sqrt{E}$ trend. This is also known as the *1/v region*, being the neutron speed v proportional to the square root of the energy $\sqrt{E}$. At higher energies, we have the *resonance region* in which the cross-section shows peaks at specific energies of the incident particle, corresponding to the possible excited states of the neutron in the compound nucleus. Finally, the region above resonances is called *smooth region* due to the slowly-varying and smooth trend of the function. Epithermal and fast neutrons have sufficient kinetic energy to overcome the threshold energy of other kind of reactions, such as *inelastic scattering* (n,n'). In inelastic neutron scattering, the nucleus is left in an excited state as, after the compound neutron formation, a neutron of lower kinetic energy than the incident one is emitted. The nucleus will then de-excite usually emitting γ-rays. Lastly, at even higher energies *spallation reactions* may occur. The process is typically divided into two separate steps. At first, the incident neutron directly interact with nucleons inside the nucleus creating an *intranuclear cascade* of high-energy
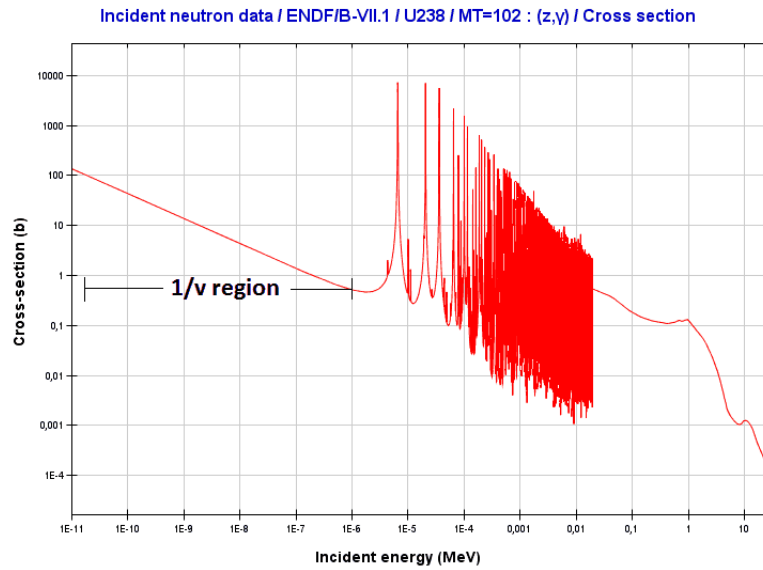
Figure 1.2: (n,γ) absorption cross section of U-238 plotted as a function of the incident neutron energy [8].

particles that can be emitted from the nucleus or they can transfer their energy to it. Then, the de-excitation process, referred to as *evaporation* takes place and particles of different nature are emitted isotropically from the nucleus [6].

For the reasons illustrated above, a neutron detector is typically made up of a converter, a target material where nuclear reactions result in charged particles, such as protons, alpha particles etc., together with one conventional radiation detector. The nuclear detector employed in this work will be described in detail in Section 2.4 but it is useful to start introducing the nuclear reactions exploited to detect the presence of neutrons.

1.1.2. Photoneutrons

Neutrons can be produced in many ways, e.g. from fission reaction in nuclear reactors, (α,n) reactions or by accelerated charged particles. For the purpose of this work (γ,n) reactions will be analyzed.

Photoneutrons are produced in photon-nucleus collisions during which the photon energy is distributed among the nucleons. Two different scenarios may occur. The first one is that a neutron near the nucleus surface acquires enough energy to emerge as an *evaporation neutron*, with an energy equal at most to the excitation energy of the compound nucleus minus the separation energy of the particle. These neutrons are emitted isotropically. The second and last is that in which the photon gives out all its energy to a single neutron that is kicked-out from the nucleus. These neutrons are mostly emitted in the direction

of the incoming photon and are known as *knock-on neutrons* [9, 10].

The evaporation neutron spectra can be modeled by a Gaussian function described by the following equation [11]:

$$\frac{dN}{dE_n} = \frac{E_n}{T^2} exp(\frac{-E_n}{T}) \tag{1.7}$$

Where N indicates the number of photoneutrons, while En is the neutron energy in MeV and T is the nuclear temperature expressed in MeV.

During radiation therapy treatments that use high-energy photon beams, above 10 MV, photonuclear reactions may occur [12]. These are mainly caused by the interaction of high-energy photons, with energy sufficiently large to overcome the neutron binding energy (about 7 MeV in most nuclides), and the high-Z materials of the LINAC head such as the target, the flattening filter, the jaws, the MLC and the head shielding (see Section 2.2) [9, 10]. Tungsten (W) and lead (Pb) have a high energy cross section for (γ, n) reaction, 50 times greater than for low-Z elements, e.g. C, N or O [13]. However, photons are also scattered inside the treatment room and may induce nuclear reactions in the bunker walls or in the patient body itself. These latter photonuclear reactions are a source of photonuclear particles (neutrons, protons, alphas) which deposit their energy directly into the tissue delivering an undesirable additional dose to the patient, other than that required to treat the tumour volume, influencing the relative biological effectiveness (RBE) (see Section 1.2) of the treatment [12].

The NCRP Report n.116 recommends a quality factor of 20 for photoneutrons energy of 0.1–2 MeV produced in radiation therapy with photon beams [14]. It implies a non-negligible contribution in patient effective dose and consequently in radiation-induced fatal cancer risk [15, 16].

It is demonstrated that the main responsible for the production of photoneutrons in the therapeutic energy level is the giant dipole resonance (GDR), a collective vibration motion of protons against neutrons induced by the photon-neutron interaction [17]. This behaviour can be observed in the absorption cross section of all nuclei as an intense peak over the energy range 10–50 MeV. It is schematically shown in Figure 1.3.

The absorption cross section, related to the GDR, σ_{abs} can be approximated by a Lorentzian distribution in spherical nuclei:

$$\sigma_{abs}(E_\gamma) = \frac{4\pi e^2 \hbar}{Mc} \frac{NZ}{A} \frac{1}{\Gamma} \frac{E_\gamma^2 \Gamma^2}{(E_\gamma^2 - E_{GDR}^2)^2 + E_\gamma^2 \Gamma^2} \tag{1.8}$$

where σ_R indicates the maximum of the distribution, E_{GDR} and Γ_{GDR} respectively the

energy (in MeV) and width of the GDR. The other parameters in the formula are: the photon energy E_γ, the atomic number Z, neutron number N and mass number A, while M is the the mass of the nucleus. This trend varies for non-spherical nuclei.
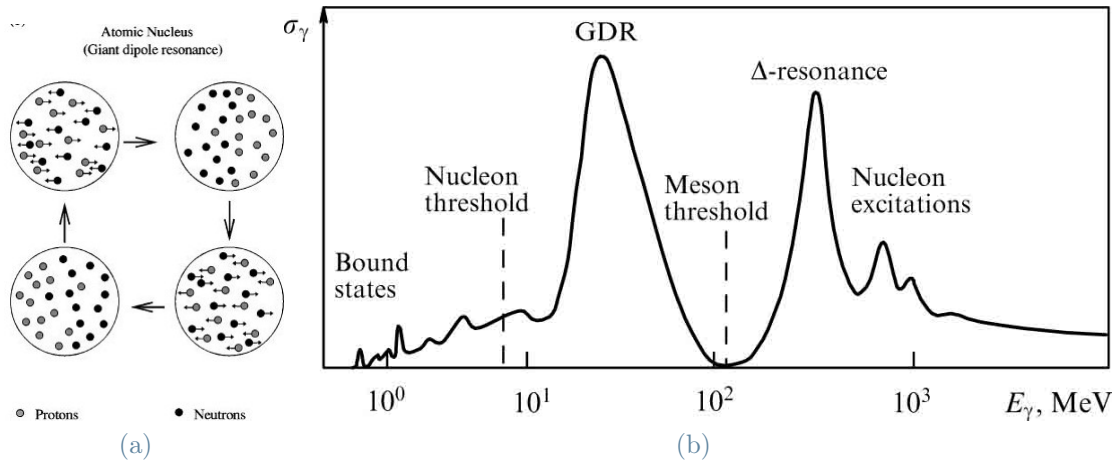

Figure 1.3: Schematic dependence of the cross section of photon absorption by atomic nuclei and free nucleons on the photon energy [18]

1.2. Radiotherapy

Several are the applications of ionizing radiation in medicine,both for diagnostic and therapeutic purposes.

Radiotherapy is a first line treatment for many types of cancers using ionizing radiation [19]. As known, the technique consists in delivering high dose to the tumour target volume, while at the same time preserving the healthy tissue nearby.

For the purpose of this work an overview of *conformal radiotherapy* will be given in the following paragraph including also recent advanced techniques.
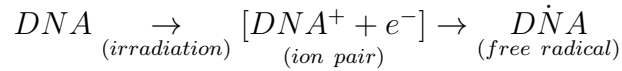
1.2.1. Biological effects of radiation

The discovery of X-rays by the German physicist Wilhelm Conrad Röntgen in the late 1895 is a milestone in the history of oncology medicine. Before that, the only way to cure a patient affected by a tumor was surgery. In a very short time an ever-growing number of doctors started treating malignant diseases with ionizing radiations, above all skin cancers because of the low penetration depth of radiations in tissues. However, the other side of the coin was soon highlighted by Henry Becquerel first and Maria Skłodowska-Curie and her husband Pierre Curie immediately afterward: ionizing radiation may produce side effects

in healthy tissues, among which induce further tumors. Therefore, the following years were devoted to the study of their physical properties and biological effects. Since then, great advances are being made and radiation oncology has become "the art of balancing between destroying the tumour and protecting healthy tissues" [20, 21].
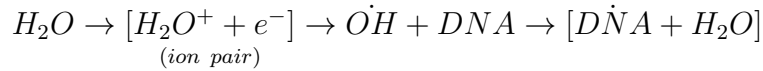
Radiation direct and indirect effects

Radiobiology is the branch of science that deals with studying the effects of the interaction between ionizing radiation and biological matter, specifically the DNA of cells. Those effects may be of two different kind: direct and indirect. In the first case, the damage is a consequence of the direct transfer of energy from the radiation to the atoms of the target element, precisely the DNA, while in the second case it is, generally, due to the absorption of photons by water molecules, this being the main constituent of our body [20, 22].

Direct Effect

$$DNA \underset{(irradiation)}{\rightarrow} [DNA^+ + e^-] \rightarrow \underset{(free\ radical)}{D\dot{N}A}$$
$$\underset{(ion\ pair)}{}$$

Indirect Effect

$$H_2O \rightarrow [\underset{(ion\ pair)}{H_2O^+ + e^-}] \rightarrow \dot{O}H + DNA \rightarrow [D\dot{N}A + H_2O]$$

LET

Let's introduce a physical quantity often used in radiation protection and radiobiology as it allows to describe the quality of ionizing radiation beams [20].

Linear energy transfer, also known through its acronym LET, is defined by the International Commission on Radiation Units & Measurements (ICRU) as the average energy deposited into the medium by a charged particle per unit track length [23]:

$$LET[\text{keV}/\mu\text{m}] = \frac{dE_{tr}}{dl}$$

It strongly depends on radiation energy as well as on the characteristics of the medium, such as its density. As particle energy increases, LET decreases. Consequently, heavy charged particles, e.g. alpha particles, are high LET or densely ionizing radiation while X and γ rays are low LET or sparsely ionizing radiations. The value that allows to distinguish between them is 10 keV/μm. It is important to underline that LET cannot be defined for photons due to the way they interact with matter. However, it is still

common to find in the literature the expression 'gamma LET' which refers to the LET of the secondary electrons set in motion by the gamma radiation [24].

In radiation therapy sparsely ionizing radiation are exploited, such as X rays or electrons, thus almost two thirds of the biological damage is caused by indirect action [25].

The main chemical effect resulting from water exposition to ionizing radiations is the cleavage of chemical bonds, hence the process is known as *radiolysis* (= Radio + lysis = Radiation + to break). Highly reactive molecules are produced in a really short time in the range of 10^{-18}s $- 10^{-15}$s [26] Let's describe a little bit the different stages leading to biological damage because of indirect action of X rays:

- 1st step: Photons interacts with biological matter, transferring part of all their energy to electrons within the medium through the well known photoelectric, Compton or pair production effects. Compton scattering prevails in the therapeutic energy range from 100keV to 10MeV;

- 2nd step: inside the track of the ionizing radiation the so-called *primary radiolytic species* are produced. Under this name fall free radicals, ions and excited molecules whose concentration along the main track of radiation depends on radiation energy, LET and type. Free radicals are fragments of molecules having unpaired electrons;

- 3rd step: Primary species can diffuse outward the track and recombine or interact with the medium leading to the production of *primary radiolytic products*. It is in this phase that free radicals may produce damages as a consequence of their interaction with the DNA;

- 4th step: The chemical bonds breakage in DNA causes biological effects [20].

1.2.2. DNA and RNA damage

The most critical targets in cells are the DNA and RNA.

The DeoxyriboNucleic Acid (DNA) is a polymer made up of two polynucleotide chains shaped as a double helix. The single monomeric unit that repeats along the entire structure contains a phosphate group, a sugar called deoxyribose and one of four nucleobases (cytosine (C), guanine (G), adenine (A) or thymine (T)). Hydrogen bonds connect two nitrogenous bases each one belonging to a different chain following the base pairing rules, i.e. A with T and C with G. The genetic information is enclosed in the sequence of nucleobases.

The RiboNucleic Acid (RNA) is also a polymeric molecule involved in many various

biological processes, the most important of which is protein synthesis since it carries genetic information. Its structure reminds that of the DNA but it is a single-stranded molecule.
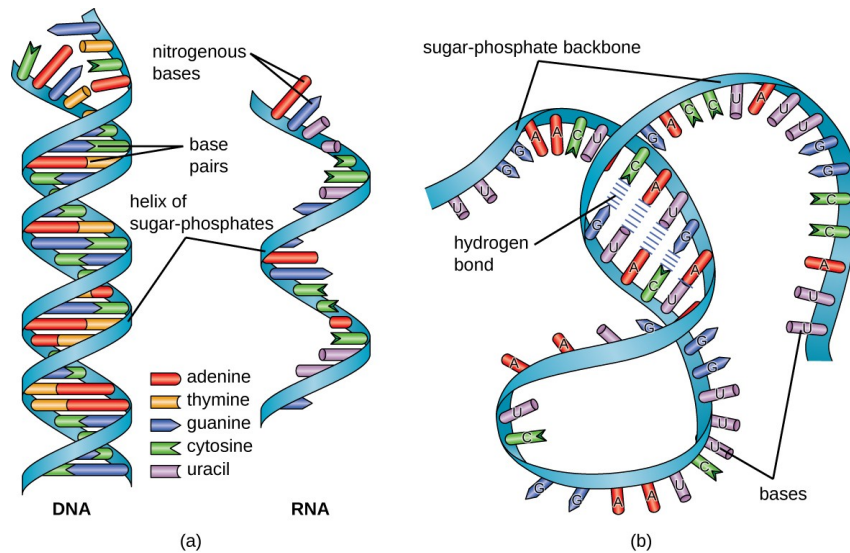

Figure 1.4: DNA and RNA structure [27]

Ionizing radiations may affect their structure by:

- damaging one of the bases;

- damaging a base pair;

- a single strand break (SSB);

- a double strand break (DSB).

The type of damage strongly depends on the particle LET, the higher the energy transferred by radiation per unit path length the worst is the damage.

In radiation therapy the goal is to inactivate cancer cells by means of ionizing radiation. A cell is considered to be dead if it loses a specific function (non-proliferating cells, e.g.muscle and nerve cells) or if it loses reproductive integrity (e.g. stem cells).

Cell Survival curves

In radiobiology it is common to describe the fraction of surviving cells as a function of the absorbed dose. The study of such empirical curves of mammalian cells, known as *cell survival curves*, allows physicists to understand the response of human cells to different type of radiations. Surviving fraction of cells is usually plotted on a logarithmic scale versus dose on a linear scale. Some examples are shown in Figure 1.6.
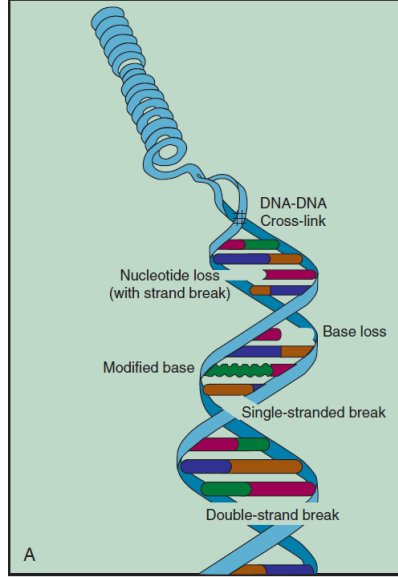
Figure 1.5: Types of DNA damage produced by ionizing radiation [28]

Their shape can be correlated to LET. Low-LET radiation cause damages that are more likely to be repaired by the cell itself, such as SSD. Hence the correspondent dose-response curve has an initial linear slope, followed by a shoulder and then becomes straight again at high doses. This trend differs from the one showed by the high-LET radiation related curve, that is and exponential function of dose [20] [30].

Over the years many mathematical models have been developed with the aim to describe what scientists observed empirically. The **linear quadratic model** assumes that two components are associated to cell kill, the first one is a linear function of dose while the second one is is proportional to the square of dose.This model is therefore based on the idea that either one DSB or two SSBs at short time and space distances are needed to cause cell death. The function describing the cell surviving curve is the following [31]:

$$S(D) = e^{-\alpha D - \beta D^2} \tag{1.9}$$

where S(D) is the surviving fraction of cells at dose D, while $\alpha[Gy^{-1}]$ and $\beta[Gy^{-2}]$ are constants.

When dose approaches a value equal to the ratio α/β the linear and quadratic components coincide.

The second noteworthy model is known as **single-hit, multi-target model**. It is based on the assumption that cell death is caused by the accumulation of single-hit events (radiation deposition of energy) occuring on the N identical targets composing the cell.
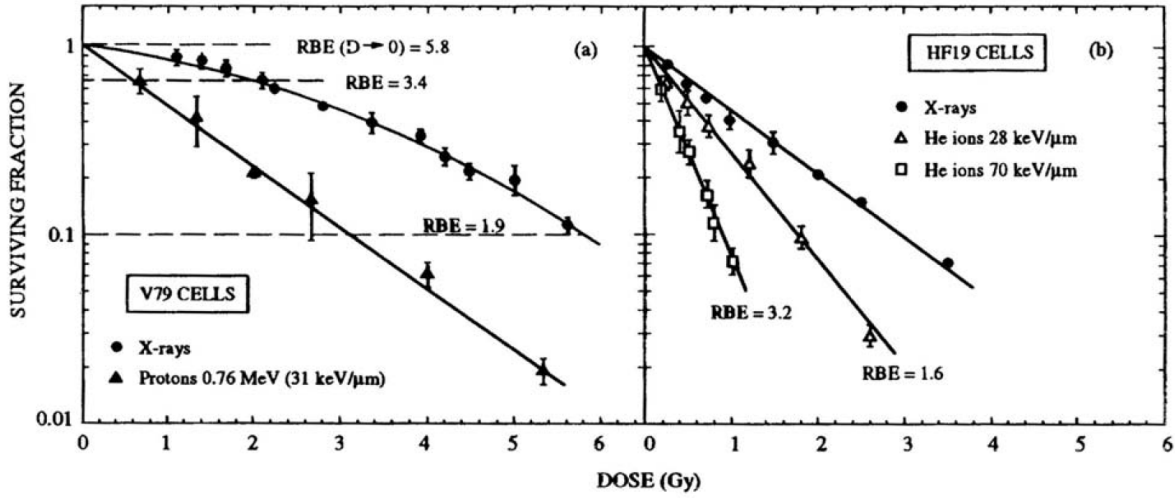
Figure 1.6: Fraction of surviving cells plotted vs dose for irradiation with (A) densely ionizing radiation and (B) sparsely ionizing radiation beams [29].

Each event indeed inactivates the target, but it is not able of killing the cell individually. If a dose D_0 is required to have on average one hit per target, then the probability distribution describing cell surviving is [32]:

$$S(D) = 1 - (1 - e^{-D/D_0})^n \tag{1.10}$$

Where:

D_0 is the *mean lethal dose* (= dose required to inactivate a target in a single event). When $D = D_0$ the fraction of surviving cells is reduced to 37% of its initial value.

n is the *extrapolation number* (= number of events required to inactivate a target). It is obtained extrapolating the exponential part of the curve to zero [31].

1.2.3. Dose-effect curve

The purpose of the use of ionizing radiation in oncological medicine is to provide dose to the tumor in order to destroy it while preserving the healthy tissues, as explained above. So the crucial aspect when planning a radiation therapy treatment plan is to balance risks and benefits to avoid the onset of complications in healthy tissues.The *dose-effect curves* explain this principle graphically.These are two sigmoids representing the tumor control probability (TCP) (curve A) and the normal tissue complication probability (NTCP) (curve B) [20] (Figure 1.8). The requirement is to maximize the TCP and minimize the NTCP. The optimum dose value should stay between a TCP > 0.5 and a NTCP < 0.05. In
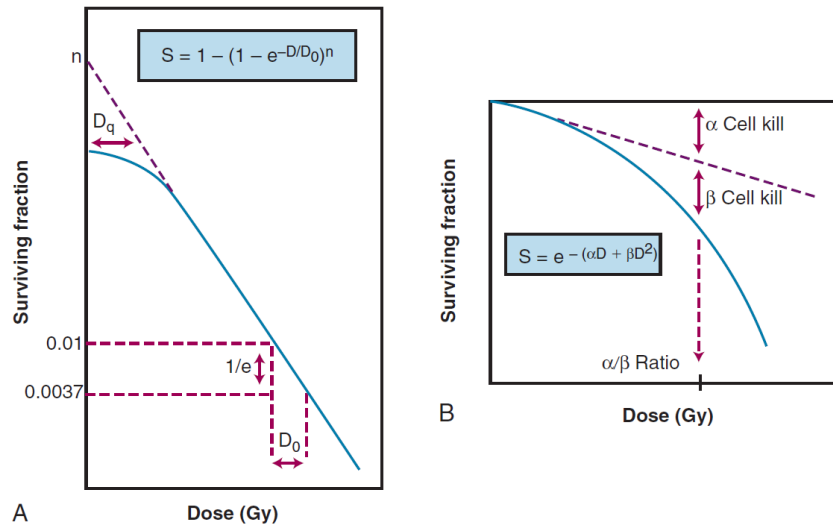
Figure 1.7: Comparison between two different mathematical methods used to describe cell survival curve: the *single-hit, multitarget* model on the left and the *linear-quadratic* model on the right [28].

other words, the so-called **therapeutic ratio** has to be optimized. The latter parameter is given by the ratio:

$$\text{Therapeutic Index } = \frac{TD_{50}}{ED_{50}} \tag{1.11}$$

where ED_{50} is the dose at which tumour is controlled in 50% of the population, while TD_{50} is the dose required to cause adverse effects in 50% of the population [33].
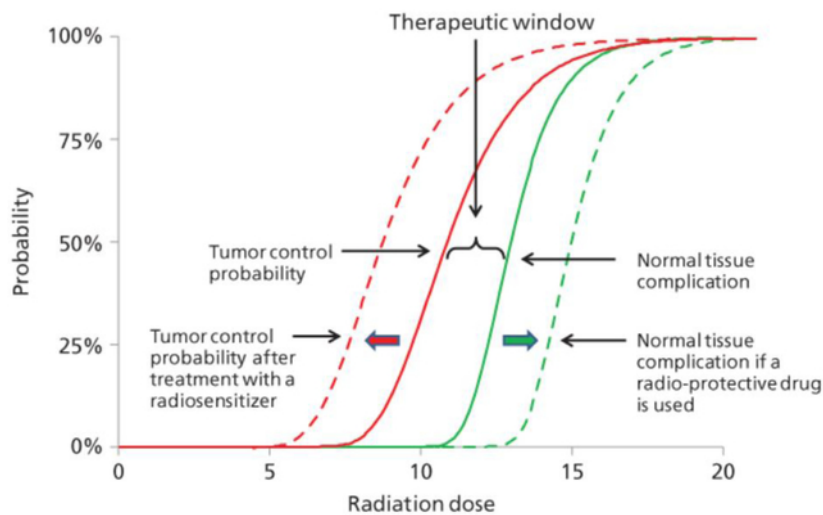
Figure 1.8: Dose-effect curves for (A) tumor control probability and (B) healthy tissue complication probability.

Several factors may influence cellular radio-sensitivity: cell and radiation type, duration

of exposure, organ or tissue exposed and external environment to name a few. Radiation therapy itself exploits the different radio-sensitivity of healthy cells with respect to tumoral ones. The following paragraphs will be thence devoted to their extensive description.

Cell cycle

Cellular radiosensitivity is influenced by the cell-cycle phase in which a cell is during the exposure to ionizing radiation. The cell-cycle consists in a series of events starting with its birth and stopped by its subdivision into two daughter cells. The most sensible phases are mitosis (M) and the gap 2 (G2).In the first one the duplication of DNA occurs before being splitted up into the new born cells, while in the second one the cell carries out a "quality check" of the duplicated chromosomes before proceeding to the next phase. Essentially, cells in the late G2 phase and mitosis are the most radiosensitive, while those in the Synthesis (S) phase are the most radioresistant [34].

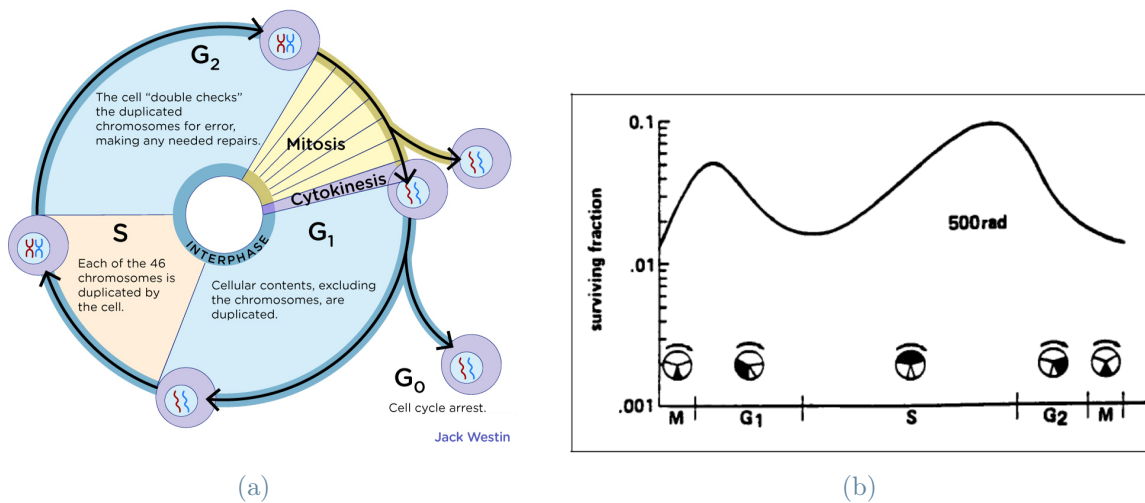Figure 1.9 displays the concept illustrated hereabove.

Figure 1.9: Cell-cycle (a) and dependence of surviving fraction on cell-cycle phase (b)

Oxygen Enhancement Ratio (OER)

The amount of oxygen present in the cell modifies the radiation response. Specifically, cells radiosensitivity is from two to three times higher when the irradiation occurs in an oxygenated environment than in an hypoxic one. It was doctor Gottwald Schwarz back in 1909 who first discovered the reduction in radiation induced skin reactions by just applying a little pressure to the skin, thus reducing oxygen supply [35].

The **Oxygen Enhancement Ratio (OER)** is a quantitative indication of the oxygen

influence on the biological effect of ionizing radiation and it is given by the following ratio [35]:

$$\text{OER} = \frac{\text{dose to produce a given effect without oxygen}}{\text{dose to produce a given effect with oxygen}} \tag{1.12}$$
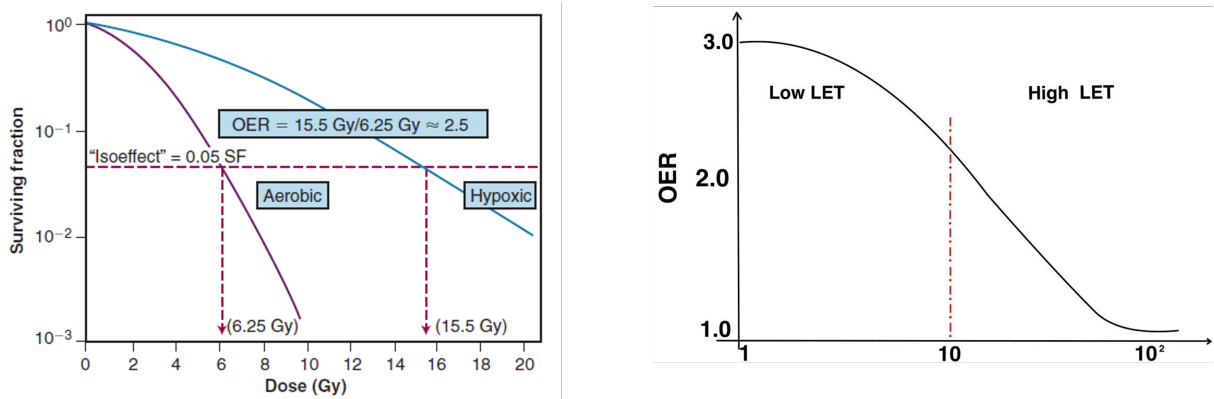

Figure 1.10: Oxygen influence on cell radiosensitivity for irradiation with X-raysn on the left [33], and X-ray OER dependence on radiation LET. The dashed line at 10 keV/μm separates the low LET region to the high LET one, on the right.

OER shows a dependence on radiation LET: it decreases as LET increases approaching OER = 1 at LET = 150 keV/μm as shown in Figure 1.10.

The value of the OER referred to X and gamma rays is, generally, equal to 3, therefore the dose required to inactivate hypoxic cells is three times higher than in the case of oxygenated cells.

On the contrary, there is no difference between the two conditions for high-LET ionizing charged particles, such as carbon ions, since they generate a high ionization density along the track which causes irreparable damages to the DNA (clustered DNA damage) so that the "oxygen effect" becomes superfluous [36, 37].

Relative Biological Effectiveness (RBE)

The **Relative Biological Effectiveness** (**RBE**) is an empirical parameter which allows to compare the biological effectiveness of a given radiation with respect to a standard radiation. Nowadays the recommended standard radiation is cobalt-60 gamma rays, but historically X-ray beam with 250 keV photons were being used [38].

RBE is given by the ratio between the dose of the reference radiation and that of the test radiation to produce the same biological effect:

$$RBE = \frac{\text{dose to produce a given biological effect from standard radiation}}{\text{dose to produce a given biological effect from test radiation}} \qquad (1.13)$$
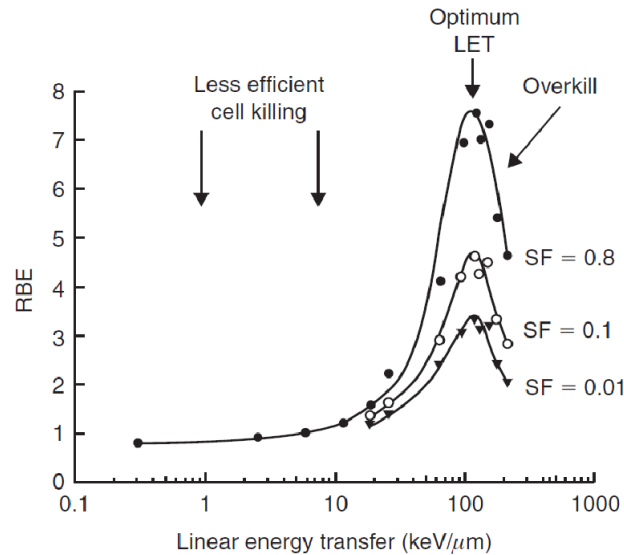

Figure 1.11: Relative Biological Effectiveness (RBE) as a function of the LET. Curves are associated to different survival fractions (SF) [39]

RBE shows a dependence on various parameters: type of radiation, total dose and dose rate, fractionation, type of cell or tissue. As already done previously in the chapter, also in this case it is necessary to study the RBE trend as a function of the radiation quality factor, strictly linked to the LET. As illustrated in Figure 1.11, it shows a bell-shape reaching a maximum corresponding to an LET of about 100 keV/μm. This can be associated to the more severe damages caused to biomolecules when using high-LET radiations since they deposit a greater amount of energy per unit path length if compared to the low-LET ones [33].

Furthermore, using high-LET radiations, the probability of causing cell death as a result of the accumulation of sublethal damage is considerably reduced, as well as that the cell can independently repair the damage. In survival curves this causes a reduction or disappearance of the shoulder.Another aspect that remains to be analyzed is linked to the LET value at which the maximum radiobiological effectiveness is observed: the main hypothesis is that, at this ionization density, clusters of ion pairs are produced along the particle track at a distance comparable to the diameter of DNA double helix ($\sim$2nm) thus causing DSBs with the highest probability. Once this value is exceeded, a reduction in radiobiological efficacy is observed as the locally deposited energy is higher than that necessary to kill a cell, therefore lost. The phenomenon is known as the *over-killing effect* [33].

Fractionation and dose rate

The total dose for a complete radiation therapy cycle is administered to patients in daily fractions for a period of approximately 4 weeks, rather than in a single session. The rationale behind this choice is enclosed in the key radiobiological phenomena known as '*four Rs*' of radiotherapy [40]:

- **Repair**: DNA sublethal damages may be repaired through complex process fullfilled by enzyme;

- **Repopulation**: if the distance between two fractions exceeds the length of the cell cycle, more and more cells will be able to reach the stage of mitosis and thus complete the division into two new daughter cells. This is vital for the healthy cells to recover; besides it does not affect the anti-tumor effect as tumor cells are less capable to repair sub-lethal damages;

- **Redistribution**: cells exhibit a different radiosensitivity depending on their cycle phase. Fractionated radiotherapy allows cells in radioresistant phases to reach the most sensible ones;

- **Reoxygenation**: it results in an increase in radiosensitivity of the tumour hypoxic cells. As it was shown in Figure 1.10, for the same dose the survival probability for cancer cells can be reduced by a factor up to three in aerobic conditions compared to hypoxic's.

Using, for example, the linear-quadratic model to describe the dose-response relationship, the effect of a multifraction regimen is clear (Figure 1.12): the shoulder is reproduced with each fraction, therefore there is an increase in cell survival, even higher as the dose per fraction is reduced.

1.2.4. Modern Radiation Therapy

Over the past decades relevant advances in radiation planning and delivery have been achieved allowing to improve the therapeutic ratio by shaping the radiation beam more accurately to the tumor volume. Besides, less acute and late toxicity are observed which has significant impact on quality of life in patients undergoing radiotherapy [41]. To name a few, 3D Conformal Radiation Therapy (3D-CRT), Intensity-Modulated Radiation Therapy (IMRT), Stereotactic Radiotherapy and Brachytherapy are the state-of-art modern treatment modalities. In the frame of this work, only 3D-CRT and IMRT will be described in detail.
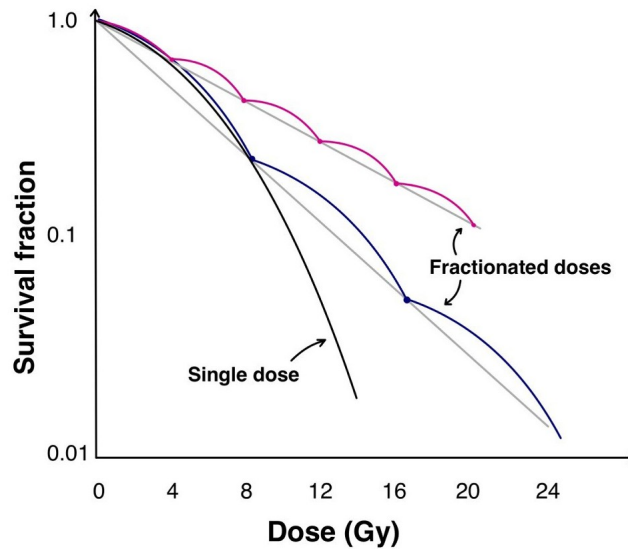
Figure 1.12: Effects of fractionation on cell survival curves (Adapted from [39]).

It should be noted that this was feasible thanks to the continuous technological innovations in medical imaging techniques. Magnetic Resonance Imaging (MRI), Computed Tomography (CT), Positron Emission Tomography (PET) and Single Photon Emission Computed Tomography (SPECT) play a fundamental role during the treatment planning procedure [41, 42]. The latter indeed requires as a first step the definition of target volumes starting from previously acquired anatomical images. The radiation oncologist therefore has to identify and draw the different target regions as reported by ICRU Reports No. 50 and 62 on the scanning and graphically sketched in Figure 1.13.

After that he can move to the actual planning phase conducted through the use of modern and sophisticated simulation software, known under the name of *Treatment Planning Systems* (TPS). Those programs help to compute parameters such as the patient treatment position, treatment field geometry or the expected dose distribution in the target complying with imposed tolerances on normal tissues. The TPS represents the key of modern radiotherapy since an ever growing complexity on iterative mathematical calculations is observed and extremely precise information are required by computer-driven treatment delivery systems.

3D Conformal Radiation Therapy (3D-CRT)

3D Conformal Radiation Therapy is a new sophisticated way of treating cancers which employs uniform intensity X-rays beams shaped to conform to the geometrical projections of the tumor [20]. As explained above, to design the clinical plan a complete 3D data set is necessary which is usually obtained from 3D images previously acquired, e.g. CT
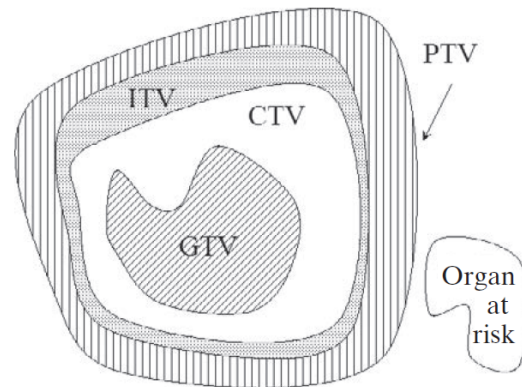
Figure 1.13: Volumes of interest defined by ICRU Reports No.50 and 62. The *Gross Tumour Volume* (GTV) is the area inside which it is demonstrated the presence of a malignant growth through the acquisition of CR,MR,PET etc. images or physical examinations by the oncologist. The *Clinical Target Volume* (CTV) is the area to be treated as it contains the GTV and other sub-clinical microscopic malignant disease. The *Internal Target Volume* (ITV) contains the CTV and additional margin needed to account for possible physiological movements, such as breathing, which would cause variations in the size, shape and position of the CTV during therapy. The *Planning Target Volume* (PTV) in turn includes the CTV plus an additional margin necessary to take into account set-up uncertainties, machine tolerances and intra-treatment variations. The *organ at risk*, at last, are those organs that could be located in the vicinity of the region to be treated, but must be kept out of the primary radiation beam as much as possible as they are particularly radiosensitive [20].

images. Nowadays, 3-D CRT has become a mainstream practice in radiation oncology [43].

Intensity Modulated Radiation Therapy (IMRT)

Intensity Modulated Radiation Therapy (IMRT) is an innovative advanced form of 3-D conformal radiation therapy. The main X-rays beams is subdivided in multiple beamlets of varying intensity each pointed in a different direction to better shape the area to be treated. The main advantage is the greatly increased tumor control probability as it allows to customize the dose distribution to each patient [44].

IMRT is clinically delivered by computerized medical linear accelerators. The external beam provided from those devices can be accurately controlled and shaped to the tumor with a collimation system made up of a dynamically controlled multileaf collimator and
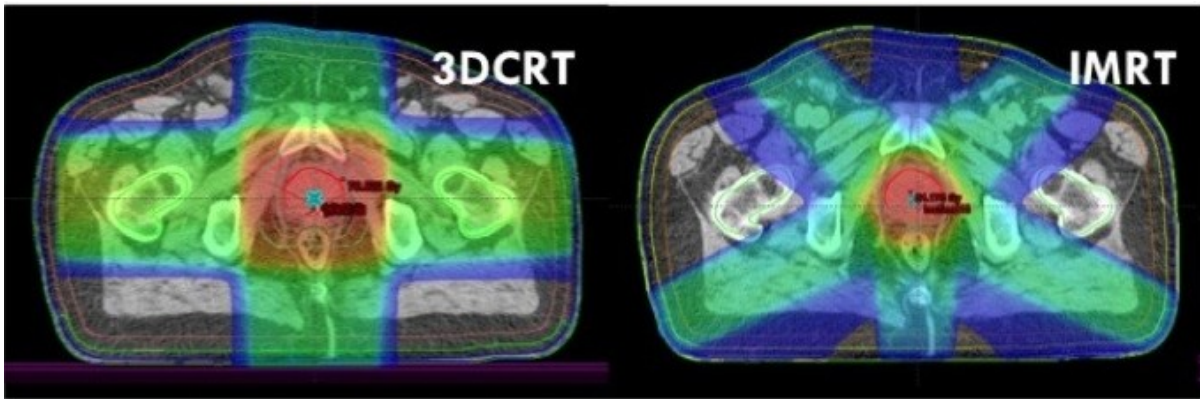
Figure 1.14: Comparison between treatment plans for 3D CRT and IMRT [45].

jaws (see Chapter 2).

IMRT is currently the best option in circumstances where organs-at-risk are not well separated from the tumor or the latter has a complex shape that cannot be treated using uniform intensity beams without giving dose to healthy tissues.

Nevertheless the extreme precision of this technique can be a drawback. First, the definition of organs at risk and tumor volume has to be highly accurate and this requires advanced imaging techniques, such as MRI and CT. Second, organ movements became a critical issue as well as patient immobilization. Third, IMRT is more expensive than 3D-CRT and requires slightly longer daily treatment times.

1.3. Cardiac Implantable Electronic Devices (CIEDs)

The heart is the fundamental organ of the cardiovascular system whose major role is pumping blood throughout the entire human body providing oxygen and nutrients to cells. It is made up of four chambers: two upper atria and two lower ventricles. The heart beat is initiated by a small group of cells at the sinoatrial node, named the heart's *natural pacemaker* which produces an electric signal able to reach the ventricle and make it to contract.

However, there may be some cases in which the normal sequence of electrical impulses sent is altered causing the heart to beat following an irregular pattern. This, in turn, will affect the operation of the vast majority of organs since blood will not be properly pumped anymore. Arrhythmia is the name given to the clinical condition in which the normal heart rate or regularity of the heart rhythm is lacking. If the heartbeat is too fast, above 100 beats per minute, it is called tachycardia (or tachyarrhythmias) while if it is

too slow, less than 60 beats per minute, it is called bradycardia (or bradyarrhythmias) [46].

(a)   (b)
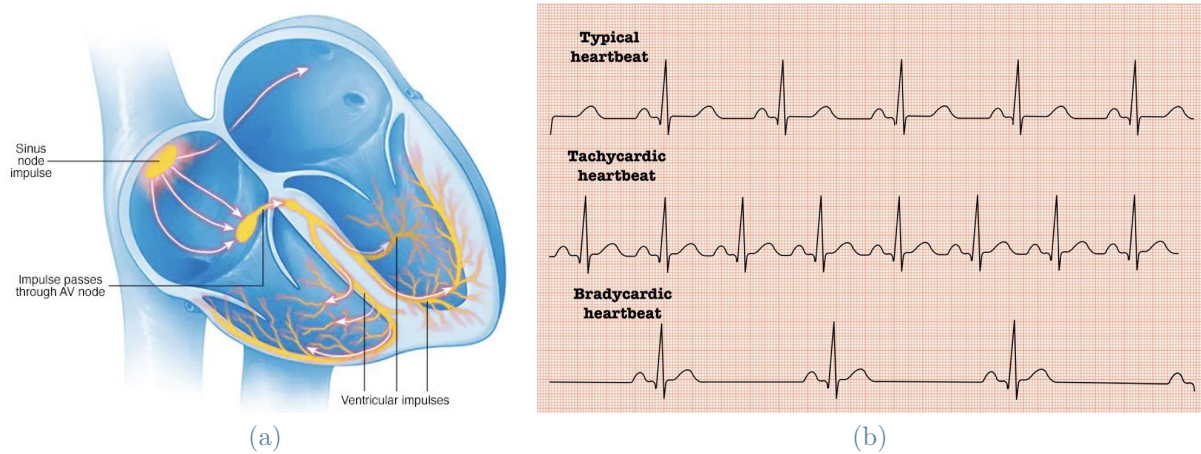
Figure 1.15: (a) Anatomy and function of the heart's electrical system [47] (b) Electrocardiogram (ECG) for a normal, tachycardic and bradycardic heartbeat. It is evident that what characterizes the traces during an arrhythmia is the different distance between the peaks (QRS complex) which will be smaller in the case of tachycardia and greater in the case of bradycardia.

Cardiac implantable electronic devices (CIEDs) is the umbrella name for a family of life-saving devices for treating ventricular tachyarrhythmias, bradyarrhythmias, and advanced systolic heart failure. It is possible to subdivide them into three main categories:

1. Permanent pacemakers (PPM);

2. Implantable cardioverter defibrillators (ICD);

3. Cardiac resynchronization therapy (CRT) devices (PPM or ICD).

They are usually implanted in the left clavicular region programmed according to patient's needs. For instance, they can provide electrical stimuli to restore a normal rhythm or voltage shocks to defibrillate the heart [48].

An illustration of CIEDs structure is shown in Figure 1.16. Generally, they are made up of three components: the pulse generator, leads and electrodes. The impulses are generated by a small battery contained inside a metal box. They are transmitted to the heart through electrically insulated wires that start from the generator and reach into the heart through a vein in the chest. At the end of each of them there is an electrode. Cardiac activity is constantly monitored and when the heart rate and rhythm are outside normal limits, the device activates [49].
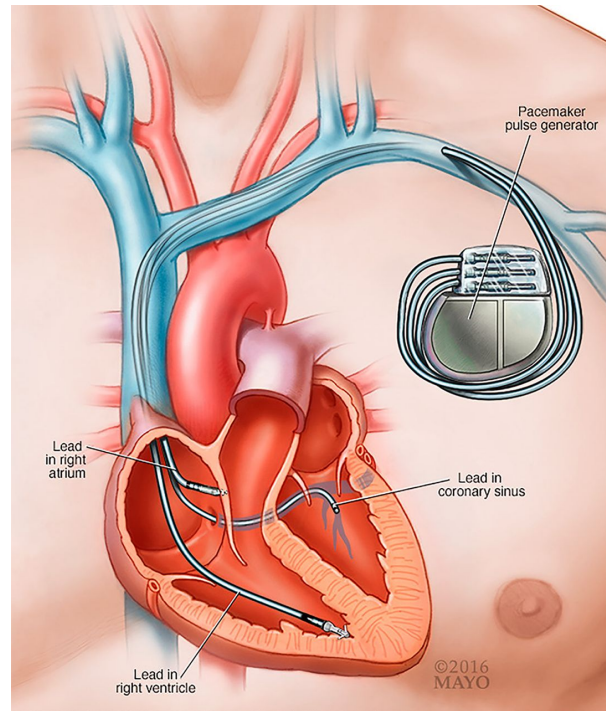
Figure 1.16: The drawing shows the typical structure and size of a CIED. It is usually placed in the chest, just below the collarbone, and connected to the right ventricle through a vein [47].

There is considerable evidence of improved quality of life in patients with CIEDs and in many cases a reduction in mortality. However, nowadays the management of patients with a cardiac implantable electronic device that have to undergo radiotherapy treatment is still challenging. It is widely recognized that malfunctions may be indeed induced directly by exposure to ionizing radiation and indirectly by secondary particles produced in the treatment room [50, 51]. These include electromagnetic interference, battery depletion, soft erros, reset, loss of diagnostics, or permanent damage to the device components [50–52].

In recent years, the direct effects of ionizing radiation on CIEDs have been extensively studied and several guidelines have been produced. However, at the state of the art, limited attention has been paid to the possible damages to cardiac devices caused by indirect exposure to photoneutrons which are inevitably produced by the linear accelerator in the treatment room during irradiation with high-energy photon beams. In particular, situations in which the tumor is located in a distant region from where the generator is implanted are to be investigated. For istance, this is the case of pelvic or iliac tumors.

In previous studies [51, 53] a possible correlation between software and hardware errors and the presence of boron-10 in the protective layers of the electrical circuits and/or

Figure 1.17: Bar chart summarizing the information obtained after the neutron radiography performed on 99 CIEDs at the NEUTRA facility. The diagnosis system reported that almost 30% of the interrogated devices were damaged, while in less than 10% there was a variation of working parameters or a sensible decrease in battery life [53].

lithium in batteries emerged. A sample of 99 devices were irradiated at the NEUTRA thermal neutron radiography station at the Paul Scherrer Institut by a thermal neutron flux of $\sim 10^7 \frac{\text{n}}{\text{cm}^2 \cdot \text{s}}$ for 2 to 10 minutes each. CIEDs were tested before and after irradiation: about half of them presented defects that eventually would have lead to their replacement in a real circumstance (Figure 1.17) [53]. The purpose of this work is therefore to investigate the thermal neutron fluence integrated over the various treatment sessions at the device location following simulated RT treatments and to verify whether this value is comparable with the one for which it has been demonstrated experimentally that damage can occur.

1.4. Neutron radiography

Neutron radiography is a non-destructive imaging technique comparable to X-rays radiography but that exploits neutron interaction with matter to visualize on photographic films the internal structures of the inspected object (Figure 1.19). X-rays are more likely to be attenuated by high-Z and dense materials, such as titanium or lead, while, on the contrary, neutrons may easily pass through heavy materials and instead strongly interact with light materials, e.g. hydrogen, boron or lithium. Figure 1.18 gives an idea of how different can be the absorption cross section for X-rays and neutrons for several materials.

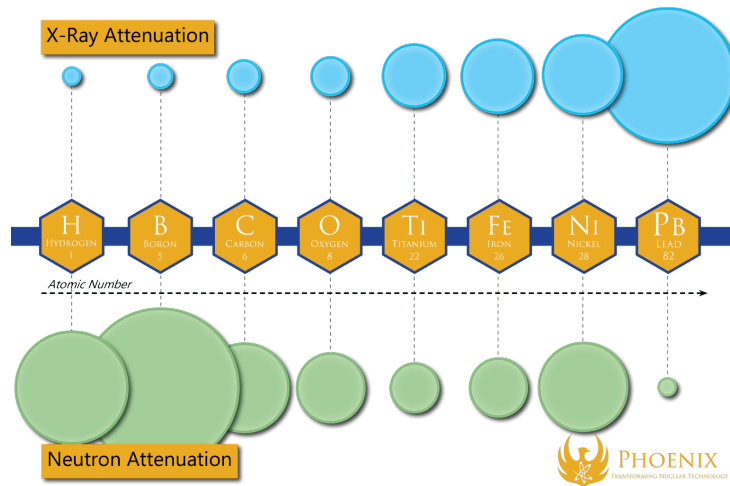In the previously cited work by Ferrante et. al [53] a neutron radiography analysis was

Figure 1.18: The image shows the different degree of attenuation of X-Rays and neutrons depending on the atomic number of the material they are interacting with. The larger the bubble, the more likely the interaction will be. Therefore, neutron beams with high probability will pass through high dense, high-Z materials without being attenuated, while X-rays weakly interact with low-Z elements, e.g. hydrogen or boron [54].

Figure 1.19: Neutron and X-ray radiography of four bullets. One of them has a different internal structure which cannot be distinguished in the second image as X-ray are equally attenuated. The neutron radiography yields different, yet complementary, information to x-ray radiography.

made to verify the presence of boron in CIEDs' components.

2 | Materials & Methods

This chapter is dedicated to the detailed description of the facilities and devices involved in this thesis.

2.1. The ESTHER facility

2.1.1. Am-Be source

Am-Be is one of the most used neutron sources due to its long half-life (432 y) and its spectrum approximately covering energies from 0.1 to 11 MeV, of particular interest for multiple applications in dosimetry [55]. The nuclear reaction exploited for the production of neutrons is the following:

$$
{}_{2}^{4}\alpha + {}_{4}^{9}\text{Be} \rightarrow {}_{6}^{12}\text{C} + n \tag{2.1}
$$

which has a positive Q-value of 5.71 MeV, meaning that it is an exothermic reaction.

The source is usually fabricated encapsulating in two stainless steel cylindrical envelopes a compacted mixture of americium oxide (AmO_2) and beryllium metal powder. This configuration maximizes the neutron production yield (about $2.2 \cdot 10^6$ neutrons per second per Ci) and reduces the amount of energy lost by alpha particles before encountering beryllium nuclei. The latter phenomenon, in fact, causes the continuous energy distribution to be lowered at higher energies, as it can be observed in Figure 2.1.

For safety reasons, since very high activities are involved, those cylinders are welded separately and some space is left between them to accommodate the helium gas formed in the reaction.

2.1.2. Expanded Source-based THERmal neutron field (ESTHER)

The ESTHER (Expanded Source-based THERmal neutron field) neutron facility at Politecnico di Milano is an experimental facility hosting a $2.2 \cdot 10^6$ s^{-1} (nominal emission rate) ^{241}Am-Be source of 1Ci from Eckert and Ziegler Cesio s.r.o. The radioisotope source
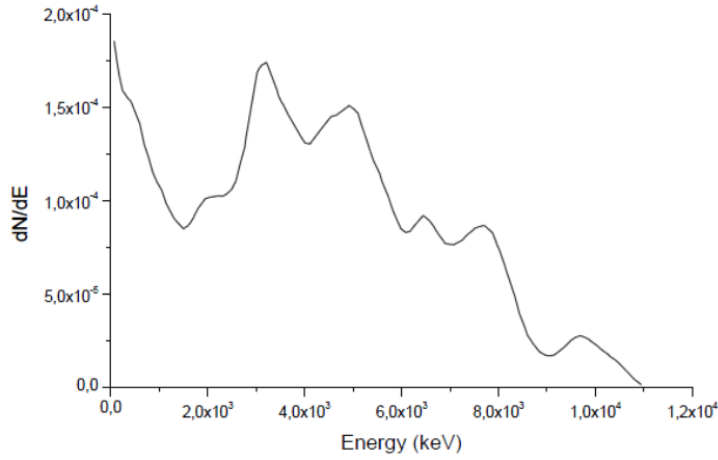
Figure 2.1: Normalized AmBe energy spectrum according to ISO 8529-1:2001 [55]

is enclosed within two co-axial polyethylene cylinders with the purpose of thermalizing the fast neutrons produced. A lead disk is also present inside the outermost cylinder and above the innermost one, allowing to shield the gamma radiation emitted by the americium during its decay. In this way, a uniform thermal neutron field is obtained.

The geometrical structure of the facility can be observed in Figure 2.2, while Figure 2.3 shows the actual facility.

Some FLUKA simulations were previously runned to test the facility, and verify the dependence of fluence rate on the measuring position. The results stated that it is quite constant along the radius of the cylinder with a variation of 0.2% up to 9 cm from the center and 0.9% up to 12 cm from the center. While it has been observed that the variation of the reference height inside the measuring chamber causes a 2% reduction of the thermal flux per cm.

In Figure 2.4 it is possible to observe, in blue, the actual energy spectrum of neutrons emitted by the source, while, in red, the energy spectrum inside the measuring chamber in two different positions along the radius of the cylinder. The thermal component is predominant although some fast and epithermal contributions are present ($E_n > 0.5$ eV: 13%). Figure 2.4 also shows the simulated energy spectra obtained for two different measuring heights in the chamber.

The average parameters computed with FLUKA simulations at 5cm from lead disk are summarized in Table 2.1 and compared to the experimental ones.
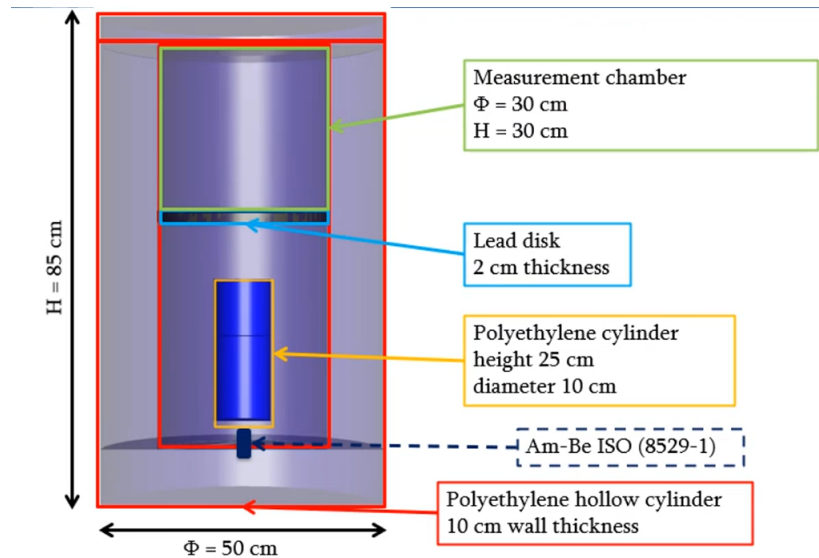
Figure 2.2: Schematic drawing of the thermalized neutron source housed in the ESTHER facility at Politecnico di Milano. [3]

Figure 2.3: Thermalized neutron source held at Politecnico di Milano. On the left it is possible to observe the external polyethylene cylinder used to thermalize neutrons emitted by the Am-Be source contained inside, as well as to shield radiations. While, on the left, the lead disk is visible together with some neutron detectors.
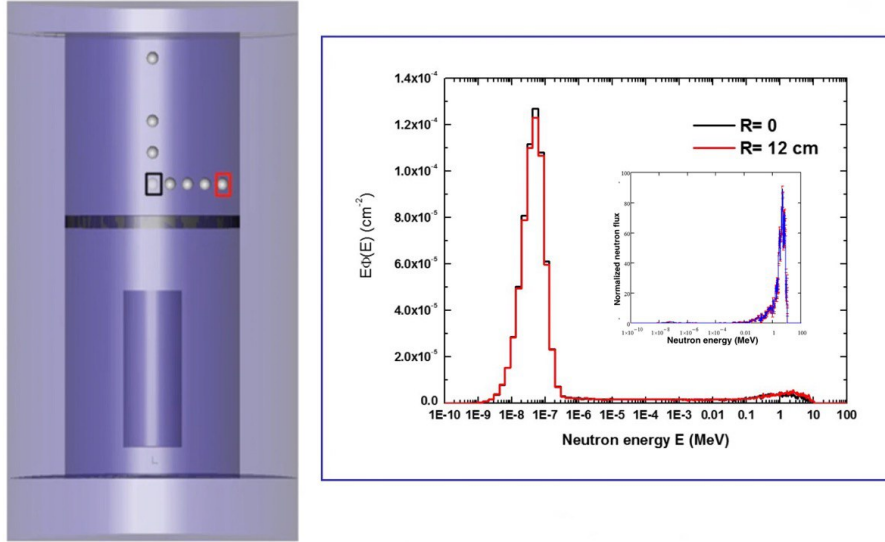
(a)
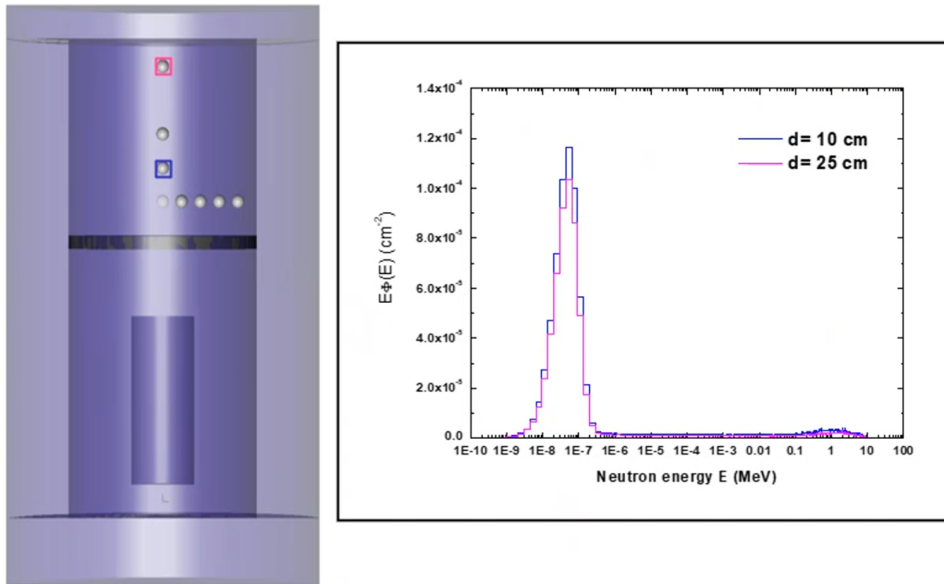
(b)

Figure 2.4: Energy spectrum of neutrons emitted by the Am-Be source computed using the FLUKA software (a) in the middle of the lead disk (R = 0) and at 12 cm from the axis (R = 12) and (b) at two distinct heights from the disk in the measuring chamber (d = 10 cm and d = 25 cm).

Radial position [cm]	FLUKA simulation		Experiments
	Total fluence rate [cm⁻²s⁻¹]	Thermal fluence rate [cm⁻²s⁻¹]	Thermal fluence rate [cm⁻²s⁻¹]
0	525	457 ± 8	447 ± 9
9	526	456 ± 8	450 ± 9

Thermal / Total ratio: 87%

Table 2.1: Comparison between simulated and measured fluence rates from the neutron source used in this work to characterize the neutron detectors.

In the frame of this study, the thermal neutron field produced by the ESTHER facility was used with the aim to calibrate the neutron detectors response in well-known conditions. The experimental procedure is described in more detail in Chapter 3.

2.2.   Linear accelerators (LINACs)

The term linear accelerator refers to a device in which particles, typically electrons, are accelerated along a linear path due to time-dependent electromagnetic fields. Specifically, they exploit radiofrequency (RF) electromagnetic fields with a harmonic time dependence [56]. Rolf Wideröe was a pioneer in this subject matter demonstrating experimentally the idea of RF linear accelerators back in 1927 [57]. However, it was only after World War II that their realization was made possible thanks to the developments in microwave technology. The Wideröe working principle of a linear accelerator is illustrated in Figure 2.5. A series of conductive cylindrical drift-tubes, or electrodes, are alternately connected to
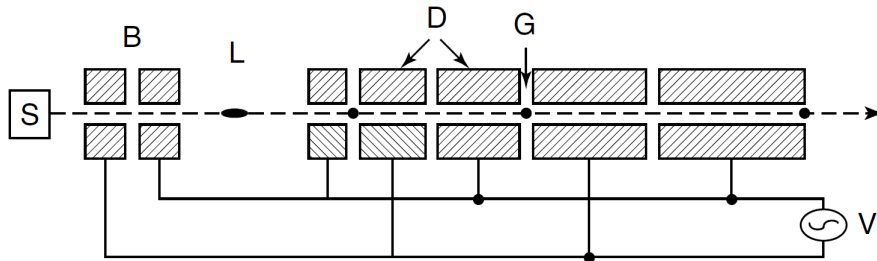
Figure 2.5: Schematic representation of the Wideroe first linear accelerator's design. S is the source of ions, continuously injected into the RF gap B in order to be bunched together before entering the accelerating structure made up of drift tubes D and gaps G. Lastly, V is the alternating voltage source, while L is the drift space necessary to let ions acquire the required spatial bunching [56].
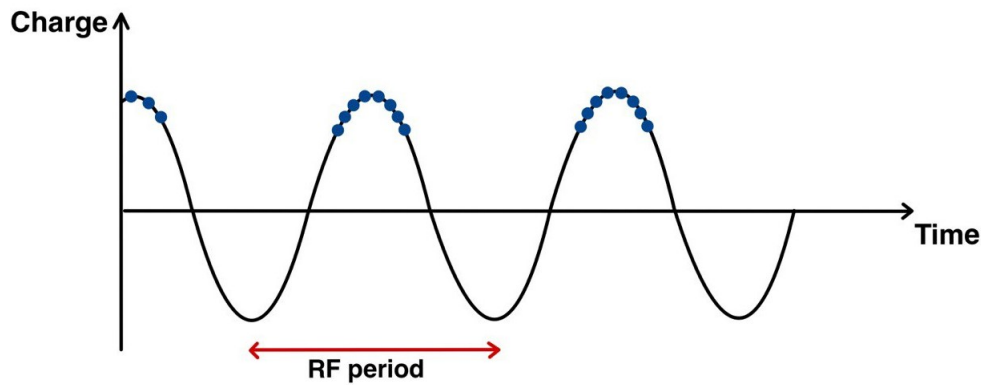
Figure 2.6: RF electromagnetic field oscillating in synchronism with movement of the particles to accelerate them in a RF linear accelerator.

the opposite polarity of an AC supply. For this reason, in the gaps between them there is a potential difference which will create the electric field able to accelerate the electrons. Conversely, inside the cylinders they maintain a constant speed since there is a constant potential. A source of particles is required and, usually, it consists in a tungsten filament which is heated and emits electrons due to thermionic effect. In order to optimize the acceleration efficiency it is necessary to group particles into bunches and to inject them into the LINAC with specific periodicity. In this way, they will experience the maximum voltage drop (Figure 2.6).

The last detail in this linac design is the characteristic increasing length of drift-tubes. This is related to the need to make the particle travel a greater distance between one gap and the other as its speed increases, or otherwise it would not meet the appropriate conditions for its acceleration.

Drift tube linac (DTL) was the first RF LINAC design. Later, some changes were made although the basic idea has been preserved.

The main problem of the original structure was that light charged particles, such as protons or electrons, approach the speed of light when accelerated by RF waves. Thus, they would require impractically large drift-tubes and distances between accelerating gaps. Some years later, Chodorow et al. [58] suggested to introduce perforated metal disks inside the cylinders to reduce electrons' velocity. This structure, called the *disk-loaded* or *iris-loaded waveguide*, is still used today in the construction of modern accelerators together with other advanced solutions.

Let us now focus on medical linear accelerators used for external radiation therapy treatments. Those devices are designed to accelerate electrons to energies from 4 to 25 MeV depending on the depth at which tumor is located.
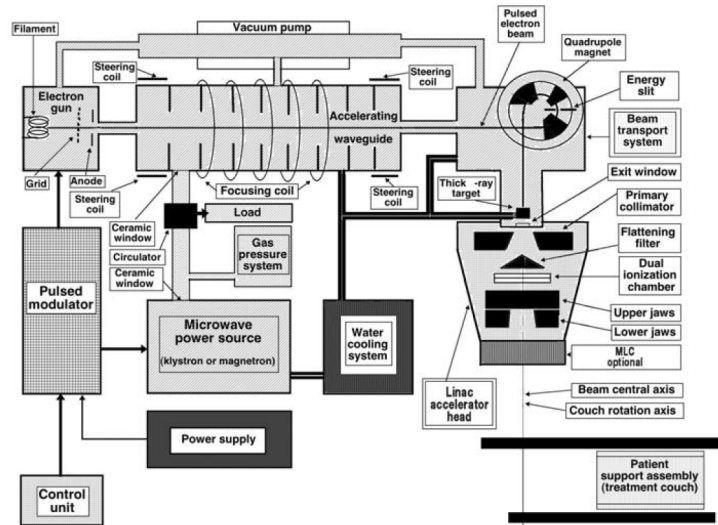
Figure 2.7: Cross-sectional view of a medical LINAC showing the main components described in this section of the accelerating structure and treatment head [20].

The essential components of a typycal modern LINAC are:

- Electron gun;

- Magnetron/Klystron;

- Waveguide;

- Quadrupole magnets and focusing coils;

- Treatment head.

Their general layout depends on the manufacturer and also on the final X-rays beam energy, however a schematic cross-sectional view can be observed in Figure 2.7.

Electrons are emitted from a heated cathode due to thermionic effect, focused into a pencil beam and directed towards the accelerating waveguide passing through the anode. This first part of the accelerator constitutes the injection system and it is called *electron gun*. Commercially it is possible to find two different kind of electron guns: diode type or triode type. The main difference between them is a grid introduced between cathode and anode in the triode one. Electrons require high power RF fields to be accelerated. Those are provided by either a *magnetron* or a *klystron*.

The first one is commonly used in *Elekta* accelerators while the second in *Varian* and *Siemens* accelerators [59]. Once generated, RF waves are injected into the waveguide, an evacuated cylindrical pipe containing a series of metal disks perforated in the center called *irises* and able to slow down electrons to the velocity that matches that of the wave.

Low-energy LINACs (4-6 MeV) can be mounted isocentrically since the accelerating tube is sufficiently short, thus having electrons already directed perpendicularly to the treatment head. In reverse, in intermediate to high-energy LINACs (8-20MeV) the accelerating structure is parallel to the gantry axis of rotation. It follows hence that the electron beam has to be deflected before entering the treatment head. It is made possible by 3 pairs of quadrupole magnets inside the *beam transport system* connecting the waveguide and the gantry head. The electron beam is bended to follow either a slalom-shaped path or a 270° loop according to the producer [59, 60].

Linac Treatment Head

The linac treatment head is structured as shown in Figure 2.8 where it is possible to distinguish the following main components:

1. Retractable X-ray target;

2. Primary collimator;

3. Flattening filter and electron scattering foils;

4. Ionization chambers;

5. Secondary collimator (jaws);

6. Multileaf collimator (MLC);

First, electrons are converted into photons due their Coulomb interaction with nuclei of the target material, usually tungsten. The result is a continuous Bremsstrahlung spectrum ranging from 0 to the maximum energy of the incident particle. Moreover, some characteristic line may superimpose to it [20]. The X-ray production efficiency defined as the ratio between the emitted energy as X-ray per energy deposited by electrons is given by [62]:

$$\text{Efficiency} = 9 \times 10^{-10} Z \cdot V \tag{2.2}$$

where V is the value corresponding to the applied voltage expressed in volts, while Z is the atomic number of target material. The accuracy of Equation (2.2) is limited to a few MV.

High-energy X rays are emitted in every direction from the target, hence the primary collimator helps to confine the beam absorbing photons outside the treatment field that would provide undesirable dose to the patient's body. Accordingly, after this stage we have a cone shaped beam since only forward directed photons could pass through. A flattening filter is now inserted in the beam path to uniform the beam intensity profile
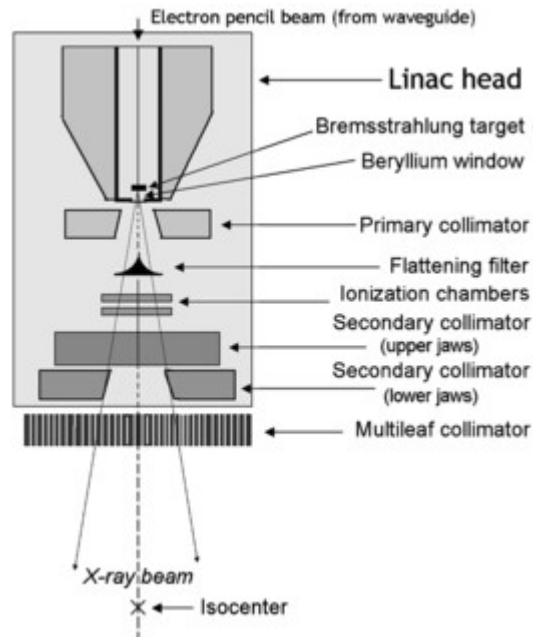
Figure 2.8: Geometry of a typical medical linear accelerator's head in the photon beam configuration [61].

and make it suitable for a clinical use. It has a conical shape and it is, usually, made up of lead, tungsten or lighter materials, such as aluminium.

The following component is a pair of independent ionization chambers which are used for dose measurement and beam quality monitoring. The first dosimeter is used to measure Monitor Units (MUs) delivered by the accelerator, where, usually, "*1 MU corresponds to a dose of 1 cGy delivered in a water phantom at the depth of dose maximum on the central beam axis when irradiated with a 10 × 10 cm² field at a source to surface distance (SSD) of 100 cm* " [20]. Note that for the purposes of this work it has been assumed that 100 MU = 1Gy.

The physician sets the MUs on the terminal connected to the accelerator according to the prescribed dose the patient should receive but it is the ionization chamber that shuts the LINAC down when that dose has been delivered. The second ionization chamber is used to monitor whether failures occur in the first one. They are also used to verify if the radial and transverse sections of the radiation beam as well as its symmetry and energy comply with the quality criteria [20]. The last two components are the secondary collimator and the MLC which are both used to further shape the beam. Specifically, the two independent jaws constituting the secondary collimator provide a rectangular or square field with a maximum dimension of 40 × 40 cm². On the contrary, MLC consists in 80 or 120 motorized leaves each moved independently from the others to conform the
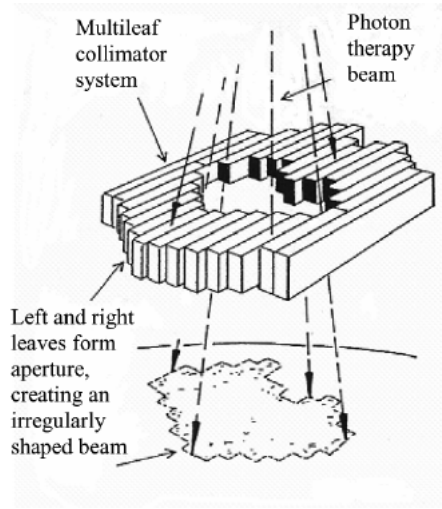
Figure 2.9: A multileaf collimator (MLC) system used in conformal radiotherapy and Intensity Modulated Radiation Therapy, providing conformal shaping of the beams to match the borders of the tumour [63].

beam's shape to the prospective view of the target volume for a specific irradiation angle (Figure 2.9). It is one of the most advancement in medical LINACs technology and it is fundamental for 3-D Conformal Radiotherapy and Intensity Modulated Radiation Therapy.

It was previously mentioned in Chapter 1 that photoneutrons production mainly take place inside the LINAC head. More precisely, it is due to (γ,n) reactions with high-Z materials, i.e. W, Pb, Cu etc., constituting the accelerator head and the beam collimation system. Several studies are reported in literature with the aim to study the photoneutrons fluence spectra and to estimate the out-of-field dose around the medical LINAC accelerators using a combination of both computational codes and measuring techniques [64–66].

According to IAEA 47 [68], there are three main contributions to total fluence in air at isocenter per 1Gy of X-ray: direct (Φ_d), scattered (Φ_{sc}) and thermal neutrons (Φ_{th}) and they are given by the following expression [68].

$$\Phi[\text{cm}^{-2}] = \Phi_d + \Phi_{sc} + \Phi_{th} = \frac{Q_N}{4\pi d^2} + \frac{5.4 Q_N}{S} + \frac{1.26 Q_N}{S} \tag{2.3}$$

where:

- Q_N is the neutron source strength in terms of neutrons emitted from the treatment head per 1Gy of photon to the isocenter;
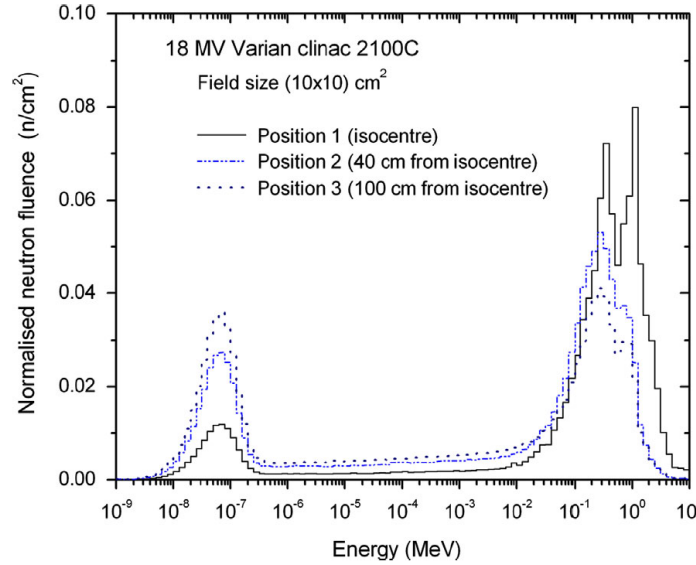
Figure 2.10: Photoneutrons spectra in air from a 18MV Varian clinac 2100C [67]. Even if taken from a specific study, this trend is typically observed around medical linacs.

- d is the distance between the source and the measuring point, given in cm;

- S is the total area of the treatment room, except for the maze area which rapresents the total surface exposed to neutrons.

Figure 2.10 shows how this spectrum might look like. Two main peaks can be observed, the first one at thermal energies (around $10^{-9} - 10^{-7}$ MeV) and the second one in the fast energy region ($10^{-1} - 20$ MeV). Moving from the isocenter to distal points of the patient table, we can see an increase in the thermal contribution and in turn a reduction of the fast one.

This general trend could show small variations depending on the LINAC manufacturer, field size or the measuring point. For example, if the measuring point is placed in a tissue-equivalent phantom, the thermal contribution is greater than the fast one because neutrons are thermalized inside it.

Finally, a useful quantity when talking about electrons impinging on a target, commonly high-Z materials in medical LINACs is the *photoneutron production yield Y* per unit power dissipated on the surface. It is given by the following expression [3]:

$$Y[1/s \cdot kW] = 1.21 \times 10^{11} Z^{0,66} \tag{2.4}$$

In Figure 2.11 is shown its increasing trend against energy of electrons impinging on thick
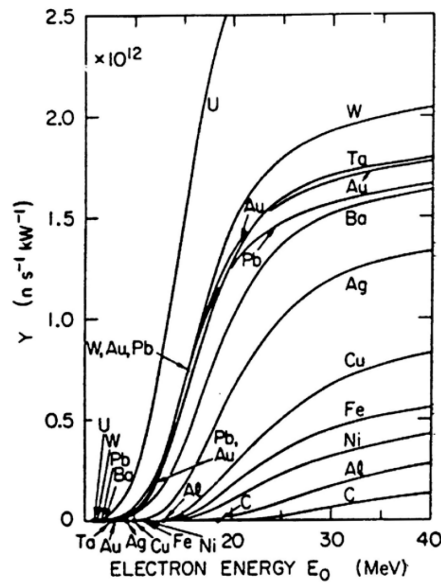
Figure 2.11: Dependence of photoneutron yield on the energy of electrons impinging on targets of various materials [3].

targets of various materials.

The experimental sessions of the present work were carried out in collaboration with:

1. "Ospedale di Circolo e Fondazione Macchi - Azienda Socio Sanitaria Territoriale (ASST) dei Sette Laghi" hospital in Varese housing a **DHX Clinac** by **Varian Medical Systems**;

2. "San Luca - Azienda Usl Toscana nord ovest" hospital in Lucca housing a **Synergy 3028** medical LINAC by **Elekta**;

3. "Ospedale Maggiore -Azienda Sanitaria Universitaria Giuliano Isontina (ASUGI)" hospital in Trieste housing a **Elekta Synergy 3028** linear accelerator.

2.3.   BOMAB-like phantom

During this work, it was necessary to reproduce realistic conditions in which a patient might find himself during real therapy sessions. For this purpose, a BOMAB-like phantom developed at the University of Pisa was used.

The original Bottle-Manikin-Absorption (BOMAB) phantom is made up by ten cylinders in high-density polyethylene and filled with a tissue-equivalent material, commonly water. They have different cross sections (elliptical or circular) and represent the main parts of

(a)   (b)
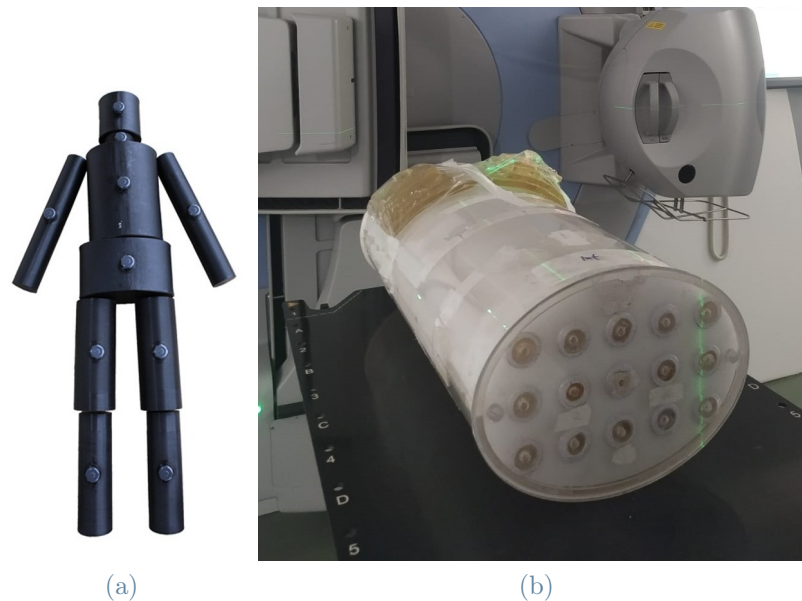
Figure 2.12: The original configuration of a BOMAB phantom on the left vs the BOMAB-like phantom trunk developed by University of Pisa on the right [70].

ICRP 23 Reference Man human body [69]: trunk, head, pelvis, neck, arms and legs (Figure 2.12a). It is, generally, used for calibrating *in vivo* measurement systems, such as the whole body counter (WBC).

Di Fulvio et al. [70] made some changes in the well-known design developing a polymethyl methacrylate (PMMA) phantom with a reduced number of channels, precisely 15 through pipes, in which it is possible to insert dosimeters. Smaller cylinders, made in PMMA as well, can be put inside those channels with the purpose of keeping detectors in specific positions during the measurements. This configuration is pretty accurate and realistic, enough to allow the simulation of clinical treatments.

At first, it was filled with water, however over time the plastic was slightly damaged and this caused leaks. The solution found was therefore to fill it definitively with paraffin, leaving only the measurement channels empty. In this study, only the part simulating the trunk was employed. If necessary, above the phantom it is possible to add two pyramidal structures made of bolus, a material used for the protection of tissues from thermal damage during radiotherapy treatments, to mimic the breast. It is a tissue-equivalent material and allows to reproduce with greater accuracy the conditions in which the cardiac device is found when the radiotherapy treatment is carried out on the breast or in a region nearby. The last configuration can be observed in Figure 2.12b.

Hereinafter some geometrical parameters are listed (Figure 2.13). They were used to

reproduce as faithfully as possible phantom's geometry in the Monte Carlo simulations performed in the second part of the present study (Section 2.5).

2.4.   The detection system

This section introduces the passive neutron detector used for the estimation of thermal neutron fluence during the experimental measurement campaign. It is composed by a solid state nuclear track detector (SSNTD) and a thin layer of boron carbide converter, enriched to 99% in ^{10}B. Section 2.4.1 is fully devoted to the detailed description of the experimental apparatus used in this work. The physical process behind neutron detection will be illustrated in Section 2.4.2. In Section 2.4.3 the Politrack® software for nuclear track analysis is presented, with a focus on the imposed settings and filters.

2.4.1.   Structure and properties

In this work, thermal neutron detection was made possible thanks to the use of a SS-NTD made of poly-allyl diglycol carbonate $(C_{12}O_7H_{18})_n$, commercially known as CR39 in combination with a boron converter, via the ^{10}B(n,α)^{7}Li reaction.

An ion traversing a nuclear track detector similar to the one described above may cause damages at the molecular bonds scale since it creates excitation and ionization along its track. This results in the formation of a *latent track*. A chemical reaction is then started from the track site to make it visible. The type considered in this work is a chemical phenomenon – i.e. chemical etching process- able to enlarge the track to the point they can be observed using an optical system, like a laboratory microscope [71].

This system is insensitive to photons and therefore perfect for use in mixed fields, such as those found around a linear accelerator. However the thermal neutron spectrum extends beyond thermal energies, as shown above. It is therefore necessary to subtract the signal associated with the epithermal and thermal components of the field from the total one. This is possible thanks to the addition of thin plates containing cadmium-113 on the two surfaces of the device. This material, indeed, shows a very steep increase in its absorption cross section for neutrons at energies below 0.5 eV (*cadmium cut-off*), as it can be observed in Figure 2.14. Therefore, if the detection system is enclosed in a cadmium filter, it will be able to record only interaction events with epithermal and fast neutrons. Finally, a subtraction between track densities obtained without the cadmium filter and the one with the cadmium filter is performed, to isolate the thermal contribution.

In Figure 2.15 a rendering of the two configurations, with and without the ^{113}Cd filter, is
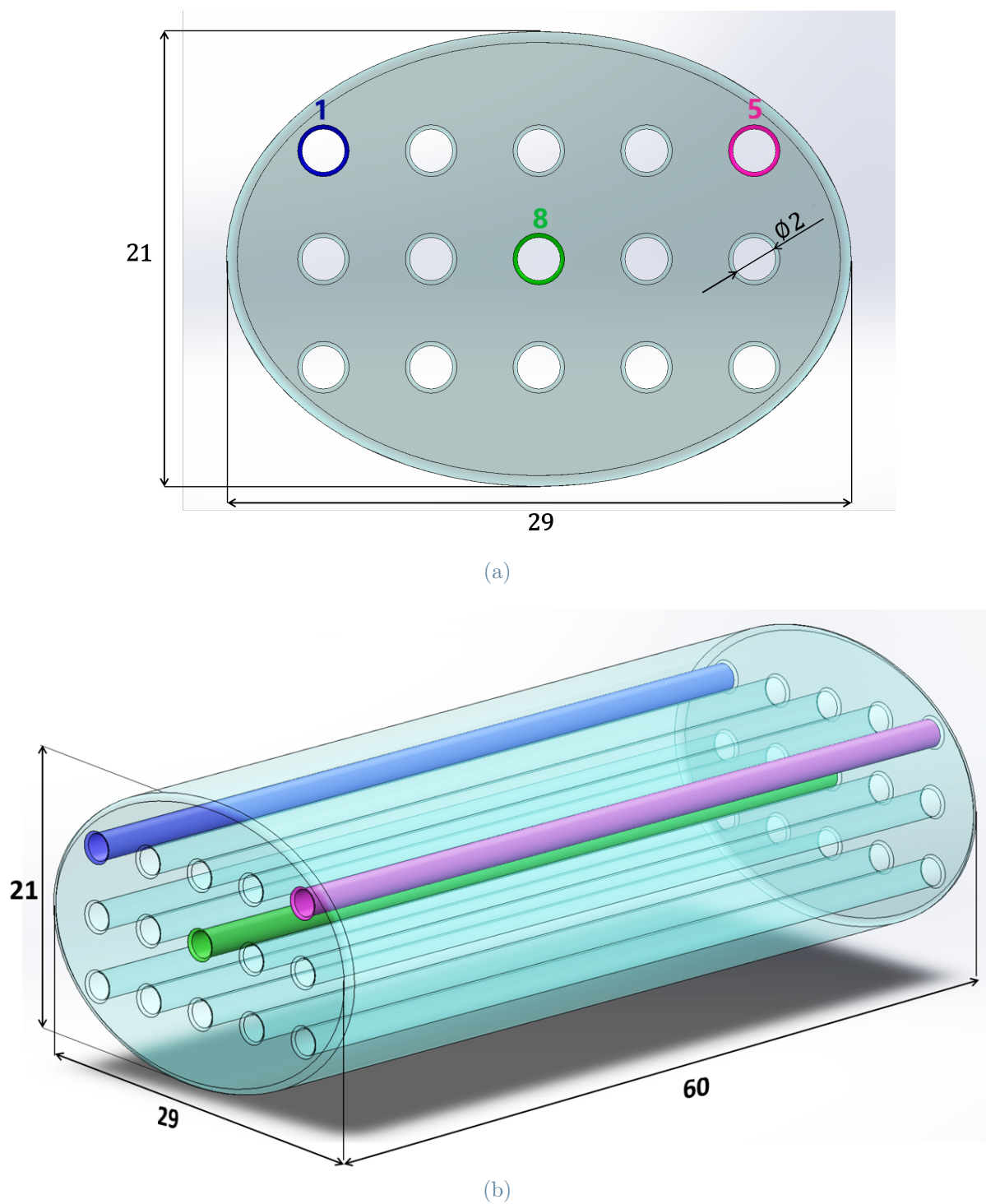
(a)

(b)

Figure 2.13: 3D rendering of a cross-sectional (a) and perspective (b) view of the BOMAB-like phantom developed by University of Pisa. Channel no.1 (in blue), no.5 (in fuchsia) and no.8 (in green) are highlighted since the devices were placed inside them during the experiments described below.
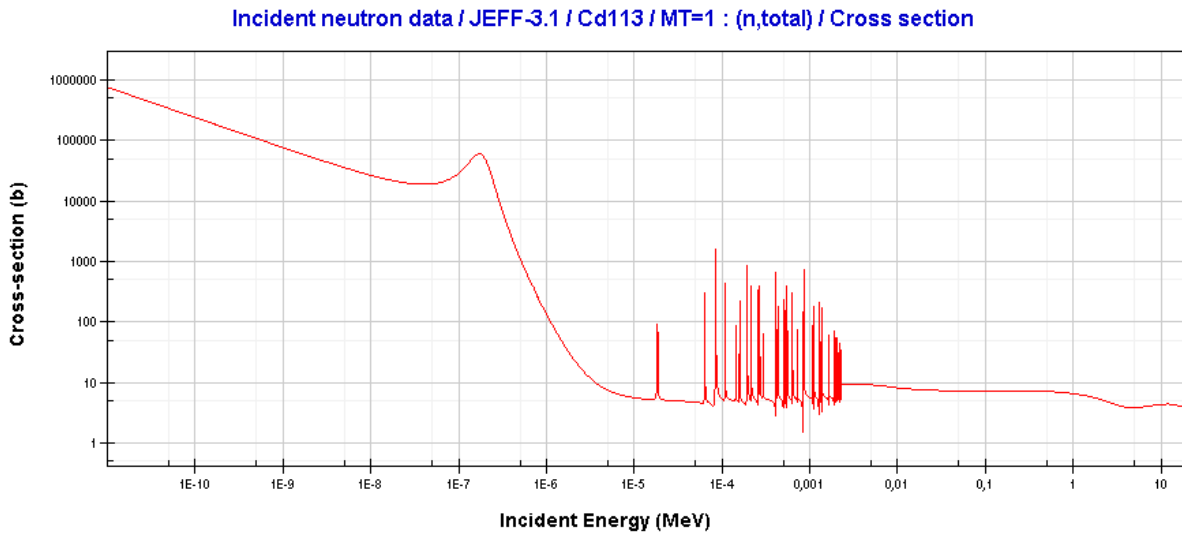
Figure 2.14: ^{113}Cd neutron absorption cross section. Neutrons with energy below 0.5eV, known as *cadmium cut-off* are absorbed with really high probability.

shown.

2.4.2.   The etching process and track formation mechanism

It was introduced in the previous paragraph that excitation and ionization of the molecules constituting the detector are at the basis of the signal formation. In the case of neutrons, since they cannot directly interact with matter through these mechanisms, the secondary charged particles are responsible for producing the tracks in the material and therefore for being detected. It is important to underline that only charged particles with a sufficiently high LET will be able to create tracks that will still be visible after the chemical etching, but we will return to this concept later.

The irradiated dosimeters are then exposed to the action of chemical agents. The main parameters influencing the yield of the etching process are chemical composition, concentration and temperature of the etchant chosen. Those are typically established by the manufacturer depending on the plastic characteristics [71]. For the experiment conducted in this work, CR39 from two different suppliers were used: TASL (Track Analysis System Ltd) and RTP (Reinforced ThermoPlastics) Company. Nonetheless, the etching procedure followed was the same and it consisted in 4 main steps:

- **1st step**: detectors are aligned in a metallic grid (Figure 2.16) and then immersed in an aqueous solution 6.25 mol/L of sodium hydroxide (NaOH) at 97.3 ± 0.1 °C for 40 minutes;
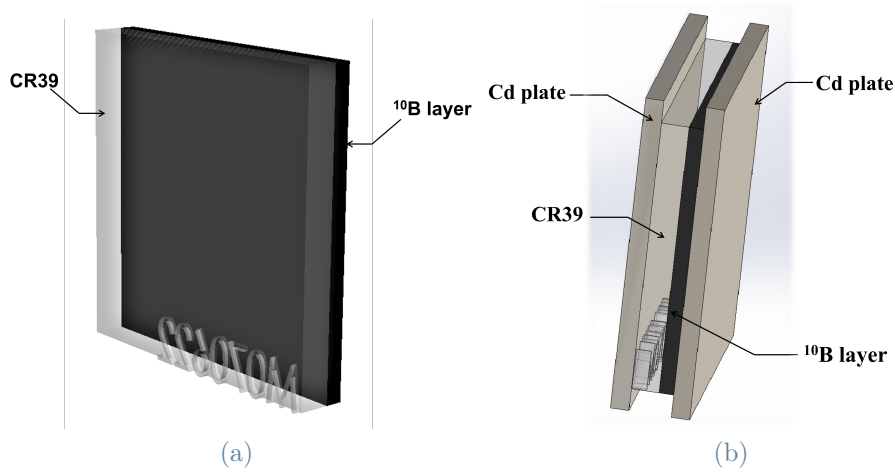
Figure 2.15: 3D rendering of the detection system obtained using the software Solidworks.The SSNTD, on which the identification code is engraved, is coupled to the boron converter and, on the right image, is covered with two cadmium plates.
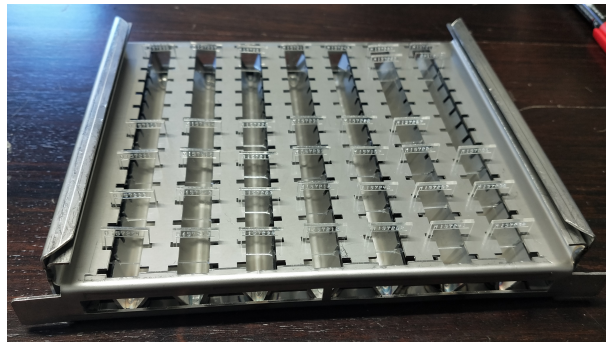
Figure 2.16: Before proceeding with the etching procedure, detectors are arrayed inside the metallic grid showed in figure.

- **2nd step**: detectors are removed from the first basin and put into another one containing an aqueous solution of 2wt% acetic acid (CH_3COOH), to neutralize soda, for 30 to 40 minutes;

- **3rd step**: consists in a bath on distilled water to eliminate acid residues and prevents the risk of halos on the plastic caused by limescale or impurities;

- **4th step**: drying phase.

The track formation mechanism has been widely investigated over the years and several models have been proposed. The one that will be described hereinafter is characterized by two main quantities, firstly introduced by Fleischer et al. [72]:

- the **bulk etch rate** V_B, which is the rate at which the undamaged material (the

bulk) is removed due to the action of the etchant on the molecules of the detector. Consequently, it depends on the specific recipe followed during the chemical process in which a progressive thinning of the material is observed. The removed layer of bulk material is equal to:

$$h = V_B \cdot t \tag{2.5}$$

where t is the *etching time*, so it is defined by the user and it is usually estimated to remove a layer of about 10-15 μm;

- the **track etch rate** V_T, the etching velocity along the particle trajectory. It is a function of the LET of the particle that induced the damage. However, it is usually considered to be constant in many models, including the one implemented in the Politrack® software used for track analysis in this work.

It is now clear that the condition that must be fulfilled for the track to be visible is:

$$V = \frac{V_T}{V_B} > 1 \tag{2.6}$$

In other words, the chemical agent will act faster along the pit of the track, due to the high concentration of reactive radicals in that region. This results in a track having a conical shape and the angle formed with the vertical axis is known as *developing angle δ*, which is a function of V (**etch rate ratio**):

$$\delta = \arcsin\left(\frac{1}{V}\right) \tag{2.7}$$

It is necessary to remind that this is the simplest case of a particle impinging with an angle normal to the detector's surface and with a constant V_T. Much more often a particle will arrive at the detector surface at an angle other than 90°. In the latter case, the cross section of the track will be an ellipse described by its minor axis d and its major axis D (Figure 2.17).

The requirement expressed by the Equation (2.6) is revised and a constraint is added on the complementary of the impinging angle, i.e. the *dip angle θ*. The physical reason always lies in the need to have a greater depth eroded along the track ($V_T \cdot t \cdot \sin\theta$) than in the bulk material ($V_B \cdot t$), or else it would disappear during the chemical treatment. This results in a condition on the dip angle which must exceed a certain critical value, known as *critical angle θ_c* (See Figure 2.18).
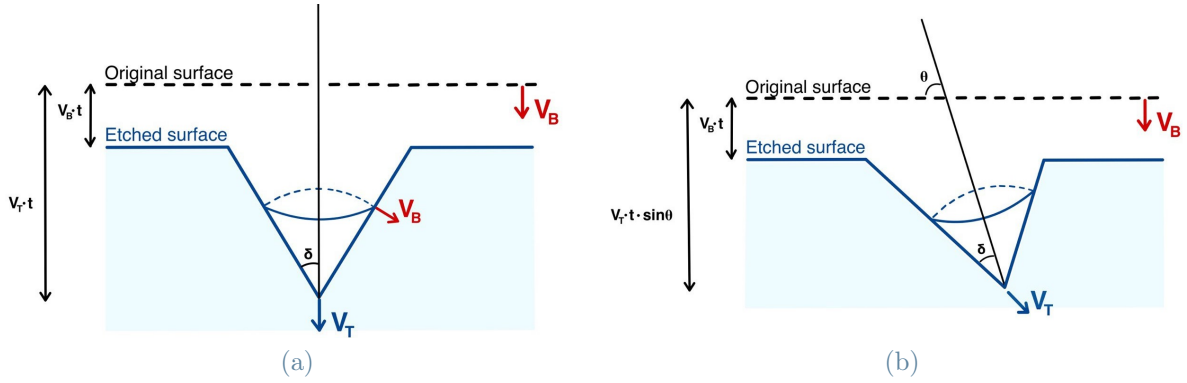
Figure 2.17: Parameters characterizing the track formation mechanism in the case of a particle that impinges the surface perpendicularly or creating an angle θ (*dip angle*) with it.

$$V_T \cdot t \cdot \sin\theta > V_B \cdot t$$

$$\frac{V_T}{V_B} > \frac{1}{\sin\theta}$$

hence,

$$\boldsymbol{\theta} > \theta_c = \arcsin\left(\frac{V_B}{V_T}\right) = \mathbf{arcsin\left(\frac{1}{V}\right)}$$

(2.8)

Therefore, taking up a previously anticipated concept and thanks to the information just illustrated, we can deduce that only particles with a high LET, therefore a high V, can almost always be detected, regardless of the angle of incidence. On the contrary, for particles with low LET, therefore low V, this will not always be possible and some tracks may be lost.

One has to be aware that if the chemical process is too long, the erosion would extend beyond the end of the latent track with the same rate V_B in each direction. After a certain time, the tracks would lose its conical shape and assume a spherical one, as shown qualitatively in Figure 2.19. This way the track becomes totally *over-etched* and leads to such deterioration of the tracks that it can no longer be distinguished from defects in the plastic, which indicates a loss of signal [73].

One important disadvantage of CR39 are *ageing* and *fading* which can affect their sensitivity due to alterations in the plastic before (ageing) and after (fading) the exposure. Specifically, the fading process can be explained by assuming a partial repair of latent tracks and it was demonstrated that it depends on temperature according to the Boltz-
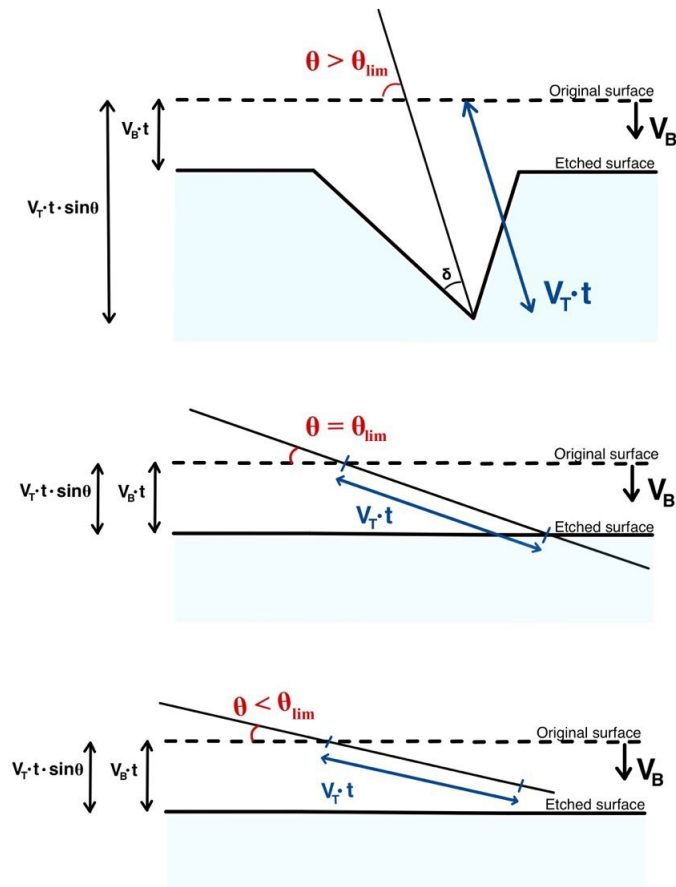
Figure 2.18: Track formation for the case of a dip angle higher, equal and lower than the critical angle.
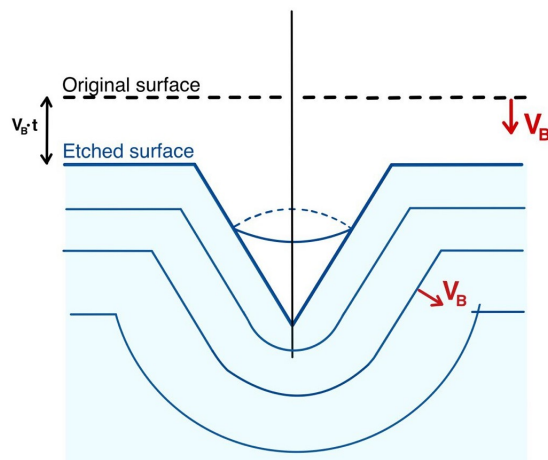
Figure 2.19: Track profiles over time: the initially conical track widens until it becomes a sphere due to total over-etching.

mann equation . They both lead to a reduction in the etching velocity V_T while V_B is unaffected [74]. The solution proposed by Caresana et al. to prevent those effects was to store the detectors in refrigerators before irradiation and to analyse them immediately after [74].

2.4.3. The Politrack® system

Politrack® is an automatic system used for scanning SSNTDs, CR39 and LR115 detectors, and performing a morphological analysis of the tracks. It was developed by the Mi.am S.r.l. company in collaboration with the Department of Energy of Politecnico di Milano with the aim of designing a system which can be used for radon monitoring and neutron dosimetry on an industrial scale as well as for research purposes [75, 76].

The hardware

Figure 2.20a shows the main components of the hardware system, that are:

- a *motorized XY scan table* with dimensions of 205x205 mm^2, installed on a 2550x750x40 mm^3 honeycomb anti-vibration breadboard and hosting a glass plate on which the detectors can be placed for the scanning. The latter can host up to 169 detectors with dimension 15x15 mm^2 in rows of 13 detectors each (Figure 2.20b);

- the *optical system* which consists of a transmission optical microscope coupled with an 8 bit CCD camera with a 1440x900 pixels resolution.The microscope is mounted on a motorized arm that allows movements along the z axis with micrometric precision. A 20x magnifying objective and an optic adaptor are installed for CR-39 fast and thermal neutron analysis. Hence, in this configuration the single frame scanned has an area of 0.08 mm^2. In this work, on an experimental basis, a 10x magnifying objective was used to improve the scanning time, thus the frame area was equal to 0.16 mm^2. A light source is also required so that the microscope can work in transmission mode: a green or amber LED diode are chosen indistinctly, and installed underneath the glass;

- a *computer* on which the software necessary to control the motorized parts of the hardware and to analyze the data is installed.

The software

The Politrack® software presents an interface through which it is possible to manage the hardware described above, to allow, for example, the identification of the optimal focus
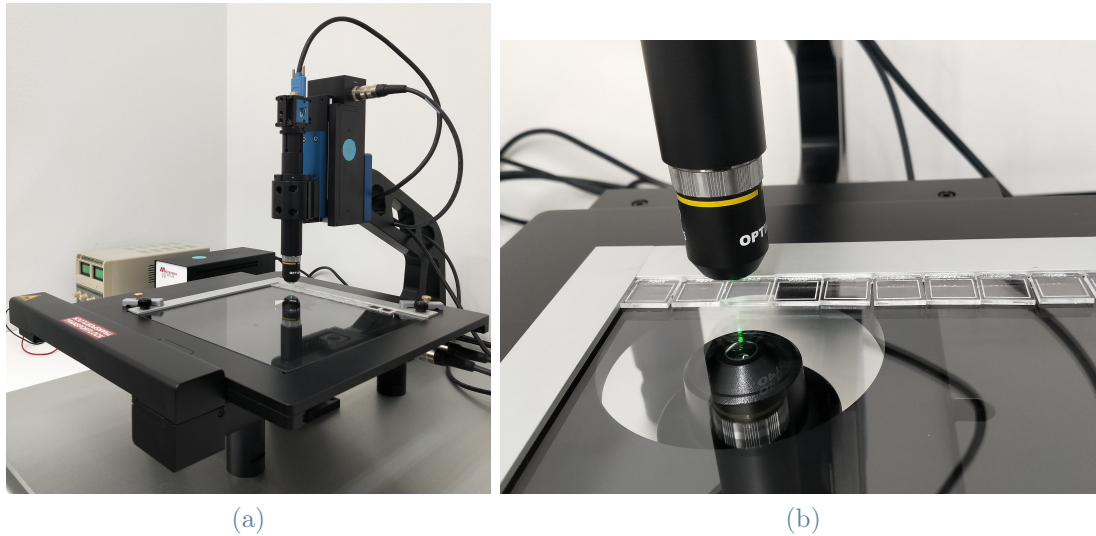
Figure 2.20: On the left, the Politrack® hardware. On the right, CR39 arrangement during the reading.

position on the surface of the detector via an autofocusing routine, or to analyse the morphology of the tracks.

Once the devices to be read have been positioned on the glass plate, the user is asked to set a series of inputs such as:

- type of analysis: fast/thermal neutrons or radon;

- number of detectors to be scanned and their dimensions;

- how many times to scan a single device.

Relevant importance is assigned to the autofocusing routine which must be performed before each reading. This has the purpose, starting from a default coordinate along the Z axis, of searching for the optimal focus position on the surface of the detector. Then, a first rough scan is performed with steps of 10μm, after which, starting from the current position identified as temporary focus, a more accurate reading is carried out with steps of 2 μm.

The last step, before continuing with the actual scan, is the loading of the *Settings* and *Filters* in the respective pages, which can be accessed via the appropriate buttons on the interface. In the *Filter* page, it is possible to activate/deactivate and adjust morphological parameters to allow the software to identify the tracks among what are defined as *objects*, i.e. all the items whose size and gray level exceed a certain threshold, including plastic defects.

The *Settings* page is instead subdivided into 4 sections:

- Digitalization parameters;

- Manual threshold;

- Morphological filters;

- Settings.

The user can then access each of these to set parameters related to the scanning procedure and the morphological analysis of the tracks. Usually, the user has only to select the *Settings* suitable for the type of detectors to be read (CR-39/LR-115) and their size; however, an advanced Politrack® user can manage features related to autofocus, such as the *Autofocus starting position* or the resolution and the speed at which the scanner moves during the autofocusing routine.

Figure 2.21 and Figure 2.22 shows a screenshot of the *Filters* and *Settings* pages containing the parameters which were defined for the correct analysis of the CR39 irradiated in the experimental sessions. They are based on a visual analysis of the objects detected during the scans and on the parameters obtained using the *Frame analysis* tool, which allows you to analyze in real time the objects in the frame under examination and shows which of them meet the imposed morphological requirements. Moving the mouse cursor over a track all its parameters are displayed.

At this point it is possible to start the scan after which the software will return three different *output* files:

- *.trk format file*: it stores all the morphological parameters of the objects that have been identified during the scan. It is mainly used when a post-scan reprocessing is required;

- *Excel format file*: it contains a selection of parameters obtained at the end of the scan and therefore of the morphological analysis. For example, a typical Excel spreadsheet for CR39 Thermal Neutrons analysis contains:

  1. Dosimeter ID;

  2. Tracks/cm^2;

  3. Uncertainty tracks/cm^2;

  4. Covered area, which is given by summing the area of all tracks on the scanned area;
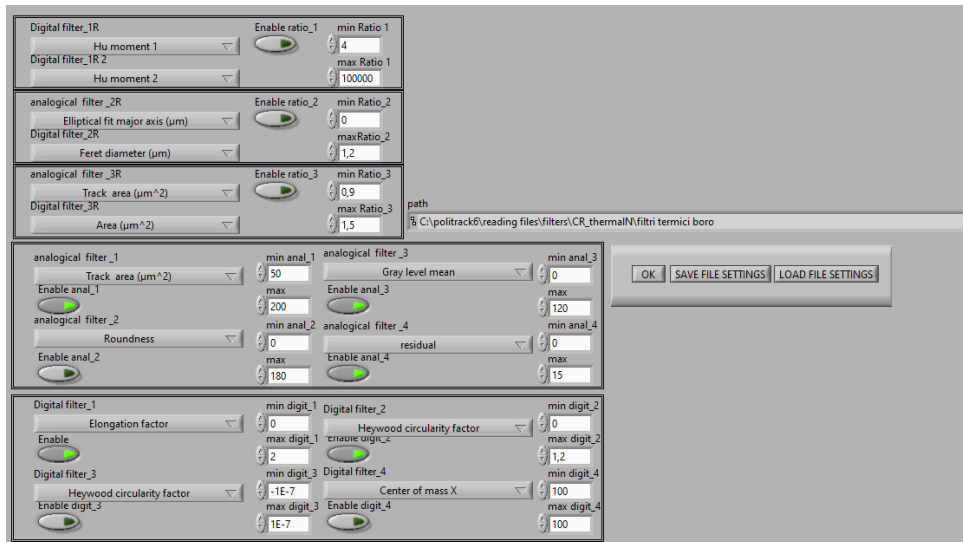
(a)
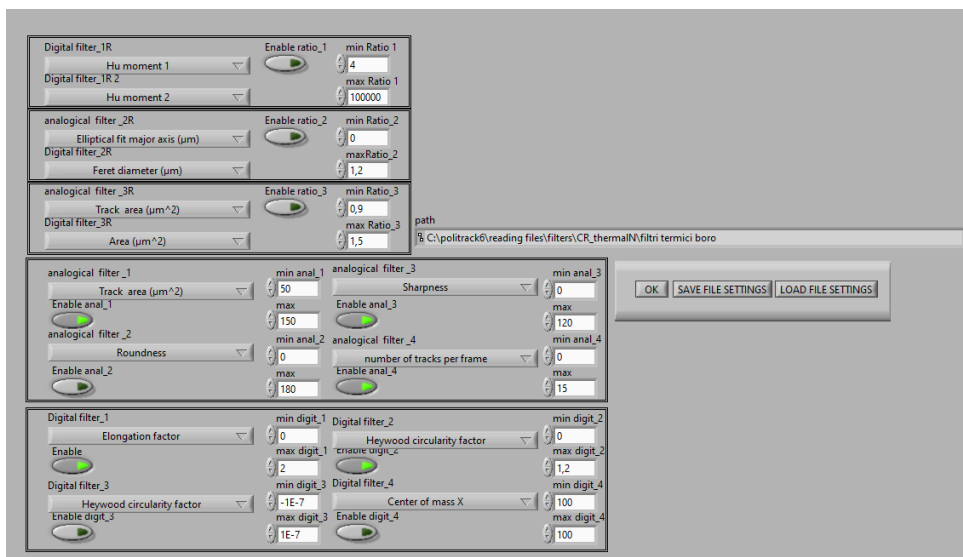
(b)

Figure 2.21: Politrack interface showing the *Filter* page and the values tuned for the TASL (a) and RTP (b) CR-39 detectors analysis.
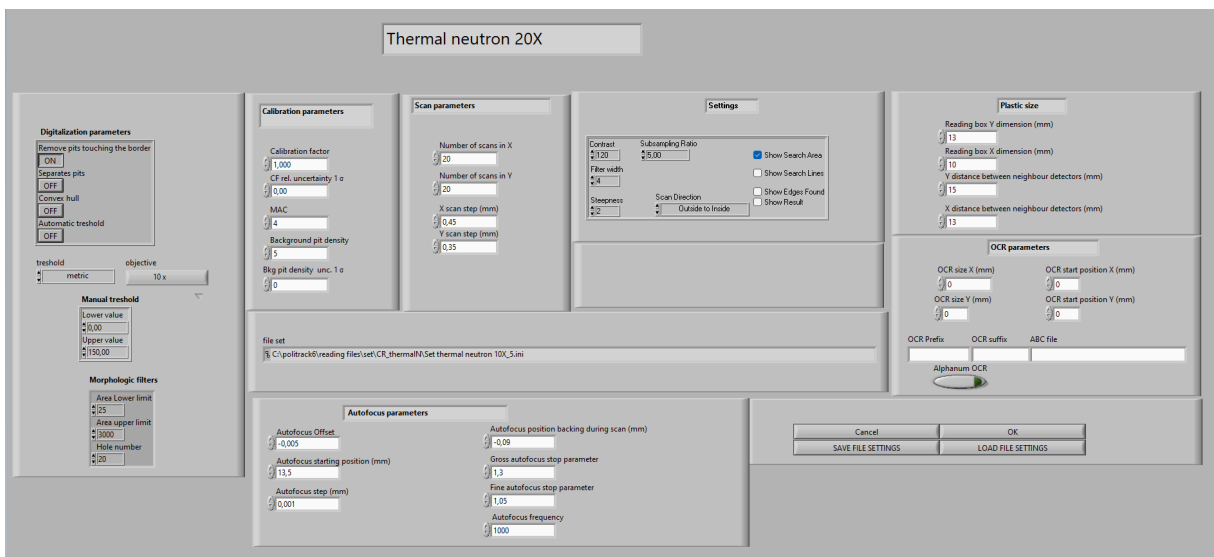
Figure 2.22: Politrack interface showing the *Settings* used for the analysis of RTP detectors.
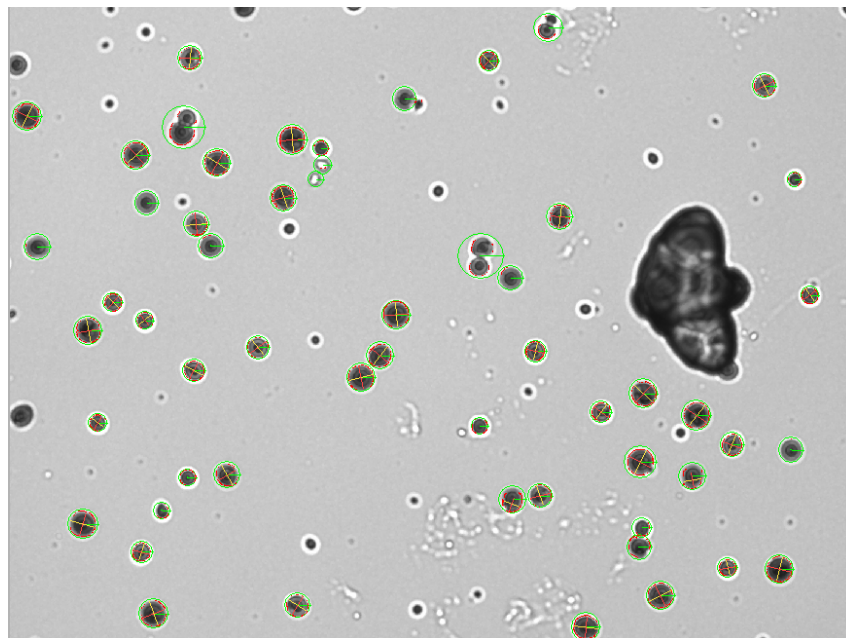
Figure 2.23: Image frame taken during the scanning of an irradiated CR39. In particular, objects that are identified as tracks have a red outline and the two major and minor axes are marked respectively in yellow and red.

5. Reduced χ^2 Test result;

6. Dose H*(10) in µSv;

7. Dose H*(10) uncertainty in µSv (95% confidence level);

8. Cluster corrected tracks (see below Statistics);

9. Possible out of focus (1 means that a wrong focus point could be occurred);

10. Wrong code reading (1 means that a wrong code reading has occurred);

11. Date and time of reading;

12. Path of the *.trk file;

- *out.dat format file*: stores all the scanner's activities, i.e. scan date, scan time, type of scan etc.

The morphological track analysis

In order for the software to perform the morphological analysis of the tracks, it must first calculate a series of parameters the values of some of which will then be compared with those set by the user as limits, lower and upper, in the *Filter* page. First of all, to do so, a binary image is produced in which all those pixels that exceed a preset threshold in terms of greyscale are placed at '1' and the rest at '0'. Then the software identifies the tracks among the objects and calculates the following variables [77]:

1. **coordinates of the center of mass**;

2. **track perimeter**;

3. **convex hull perimeter**: the perimeter of the smallest convex polygon containing the pit;

4. **holes perimeter**: sum of the perimeter of the holes inside a pit;

5. **Feret diameter**: the longest distance between two pixels belonging to the pit;

6. **equivalent ellipse major and minor axes**: the major and minor axis of an ellipse with equal area and perimeter as the pit;

7. **equivalent rectangle major and minor sides**: the major and minor sides of a rectangle with equal area and perimeter as the pit;

8. **hydraulic radius**: ratio between the area and perimeter of the pit;

9. **Waddell disk diameter**: diameter of a disk with an area equal to that of the pit;

10. **area**;

11. **holes area**;

12. **convex hull area**;

13. **number of holes** (inside a pit);

14. **track area to image area percentage ratio**;

15. **elongation factor**: ratio between the Feret diameter and equivalent ellipse minor axis;

16. **compactness factor**: ratio between pit area and the area of the bounding rectangle;

17. **Heywhood factor**: ratio between the pit area and the circumference of a disk with an area equal to that of the pit;

18. **Hu moments** from 1 to 7: image moments, i.e. the weighted average of the image pixels intensities, invariant for shift, scale, and rotation.;

The analysis proceeds with the calculation of the parameters reported below starting from the grayscale image. A circular region of interest (ROI) surrounding the track's center of mass and with a radius equal to the Feret one is set and the software starts a scan from the inner side of the ROI to the edge. The latter is defined as the locus of points with a specific contrast in terms of greyscale. An elliptical fit is then performed and the following parameters are computed:

1. **coordinates of the center of the fitted ellipse**: it is the ellipse that best fits the outline of the track opening;

2. **major and minor axes of the fitted ellipse**;

3. **area and perimeter of the fitted ellipse**;

4. **grayscale mode and mean inside the track**;

5. **residual**: it is an estimate of the goodness of fit since it is given by the difference between the actual track contour points and the ones of the fitted ellipse;

6. **sharpness**: ratio between the area at point 3 and the one obtained through the same procedure but setting a threshold equal to half the previous one.

Statistics

Since tracks are generated randomly on the detector surface, their distribution per unit area must follow the Poisson statistic. This is easily understood if we see as n sub-detectors the frames that compose the scan of a detector that observe the same radioactive decay phenomenon.

The software then performs a reduced chi-square test to verify the hypothesis that the data follows the expected distribution [76]:

$$\chi^2 = \frac{\sum_{i=1}^{n}(Tr_i - \overline{Tr})^2}{\overline{Tr}} \qquad (2.9)$$

where Tr_i indicates the number of tracks in the i-th frame, n is the total number of scanned frames, while $\overline{Tr}$ is the average number of tracks per frame. When n goes to infinity, the value of the χ^2 should reach unity. For this study, I chose to accept χ^2 values in the range $0.7 \div 1.3$, except for rare outliers (for which, however, it was checked that the scanning occurred correctly).

Overlap correction

If two or more tracks on the detector surface are superimposed (i.e. the distance between their centers is less than the sum of their radii) they would not be counted as they do not respect the required morphological parameters. In Politrack® software a function is implemented to correct the track density for this effect. Hence:

$$\text{Tracks}_\text{corrected} = \frac{\text{Tracks}_\text{measured}}{(1 - K \cdot A_c)} \qquad (2.10)$$

where the parameter K is set to 4 for circular tracks, while A_c is the covered area. The latter is obtained by summing the areas of all objects identified during the scan, including those that are not recognized as tracks.

2.5. The Monte Carlo Method applied to the radiation transport problem

The Monte Carlo (MC) method is a mathematical numerical technique used to estimate the outcome of a stochastic problem. It consists in repeatedly random sampling from probability distribution functions describing the problem under investigation.

Event Log

1. Neutron scatter, photon production
2. Fission, photon production
3. Neutron capture
4. Neutron leakage
5. Photon scatter
6. Photon leakage
7. Photon capture

Incident Neutron

Void   **Fissionable Material**
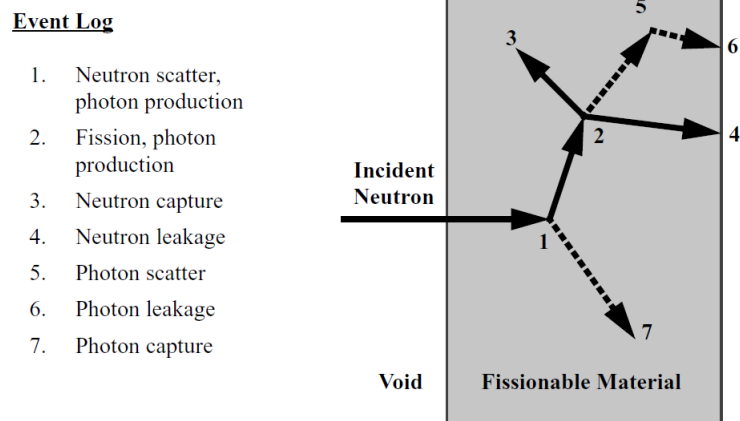
Figure 2.24: On the right, the image illustrates the ways in which the life of a neutron could be described by means of a Monte Carlo code. At the tip of each arrow a possible interaction event takes place which will randomly modify its history and may lead to the birth of further particles whose path will in turn be followed until their death. On the left, some of the possible interaction events are listed [78].

The MC approach has been widely used to solve problems in several different fields, from Economics to Physics and so on. In this section, we will see how it was applied to a radiation transport problem, which is typically encountered when the distribution of radiation emitted from a clinical LINAC is under investigation.

The basic idea of the MC method applied to radiation transport is that from the moment a particle is born up to its death it may undergo interactions with the surrounding environment with a certain probability. Therefore, the entire path (or history) of the primary and secondary particles has to be followed and, each time an interaction site is encountered, the probability distribution functions physically describing the interaction are sampled to define the outcome at that step of the particle's life (e.g. absorption, scattering etc.). In doing so, the complex problem of radiation transport will be split into a series of interaction events which will be analyzed in sequence and which will eventually lead to determining the particle distribution in the simulation environment.

For example, Figure 2.24 illustrates what has been explained above considering a neutron impinging on a slab of fissionable material. If any and what kind of interaction will took place is determined by the random numbers selected from the probability distributions defining the process listed on the left.

2.5.1.   MCNP 6.2

The Monte Carlo approach is at the basis of the Monte Carlo Neutral Particles (MCNP, version 6.2) code, developed by Los Alamos National Laboratory and which was used in this study to improve and validate the computational model of an Elekta Synergy linear accelerator. In general, the code can be used to simulate the transport of neutrons, photons and electrons alone, or coupled (neutron-photon-electron, photon-electron, or electron-photon). The energy range of such particles can extend from 10^{-11} MeV, for neutrons, up to 100 GeV, for photons. At the Los Alamos National Laboratory, a further version of the code was developed, known as MCNPX (Monte Carlo N-Particle eXtended) and through which it is possible to simulate interactions between 34 different types of particles (nucleons and ions) and over 2000 heavy ions at almost all energies. Note that MCNP version 6 also incorporates MCNPX.

The structure around which the entire input file is built is made up of four main sections, each of which can be expanded in order to obtain a model of the phenomenon to be simulated with the desired degree of detail:

Title Card: it contains a title or a brief description of the problem addressed.

Cell Cards: all the objects that make up the 3D simulation environment are defined through the cells in terms of *geometry*, as the union, complement or intersection of regions and volumes bounded by surfaces, *material* and *importance* to the simulated particles. The code structure to define a cell will therefore be the following:

num	mat	dens	geom	params
101	1	-11.35	$(4:6:5)$	$\mathrm{imp:e,n,p=1}$

where *num* is a random number defined by the user identifying the cell (101), *mat* is the number associated to the material from which the cell is made and whose composition is specified in the 'data cards' (1), *dens* is the cell material density (-11.35 g/cm^3. The minus sign indicates that the following value is a mass density in units of g/cm^3; on the other hand, if there is a '+' sign, the following value is an atomic density in units of 10^{24} atoms/cm^3, i.e. atoms/b-cm), *geom* indicates the surfaces that are combined to shape the cell and defines their relationships using Boolean operators (in this example, cell 101 is the union of cells 4,6 and 5), *param* contains other cell parameters, such as the importance of the specified cell for one or more particles (in this example, electrons, photons and neutrons). The last entry tells MCNP what weight to attribute to the particle in that specific region of space so that if this is equal to 0 its history is interrupted. It is also necessary to define a

'macrocell' that is outside the union of all the others defined previously. This cell is usually referred to as 'graveyard' and inside it the importance of each particle is set to 0 so that if they cross the outermost surface of the model and fall inside it they will be killed. Greater importance is given to the areas of interest by increasing the number of simulated particles within them. For example, if the importance of a particle in a cell is set to 2, then it will be split into two new different particles that will independently contribute to the simulation. It should be noted, however, that the weight of these is consequently reduced, when calculating the outputs, to keep the physics of the problem unaltered.

Surface Cards: they contain all the surfaces from which each previously defined cell is composed. In MCNP each point of the space is defined through three coordinates (x, y, z) of the Cartesian space, therefore the surfaces are described through functions of the type f (x, y, z). Hence, the input code contains a mnemonic that specifies the type of surface (e.g. C/Z represents a cylinder parallel to the z-axis) and the coefficients of the respective terms of the equation. The alternative way to define surfaces and cell is the use of *macrobodies*. These are 'standard' solid geometric structures, such as the rectangular parallelepiped or the right circular cylinder, which the user can exploit by writing their mnemonics and a series of parameters defining their dimensions.

Data Cards: in the 'data' section the materials filling the cells, the radiation sources, the physics of the problem, the quantities of interest to be tallied, the variance reduction techniques, the cross section libraries etc. are specified and described in detail.

It should be specified, as it could be useful for what is described below, that in MCNP a *tally* is a sort of counter or virtual detector that allows to estimate the quantities of interest in a region by summing the individual contributions given by the simulated particles.

The MCNP output file contains a summary of how the code run along with the required tallies, normalized per starting particle, and their respective relative errors. The latter are defined as the ratio between the standard deviation of the mean and the estimated mean and they are proportional to $1/\sqrt{N}$, where N is the number of simulated primary particles.

For more detailed and exhaustive information refer to the user's manual [78].

2.5.2.   Monte Carlo Model

In this work we extended the Monte Carlo model previously developed by the University of Trieste of an Elekta Synergy medical accelerator and the treatment room where it is installed (at ASUGI, Trieste), including the presence of a phantom. To do so, we implemented the model of a cylindrical phantom with an elliptical base. The simulations were performed using MCNP, version 6.2, and validated with experimental data. This software is particularly suitable for the present work as it allows the transport of electrons-photons-neutrons, to simulate photonuclear reactions (of particular importance in the frame of this work as we are investigating the neutron contamination of the high energy photon beam) as well as the moderation of fast and epithermal neutrons [79].

Let us now briefly describe the model setup, although it is not possible to go into much detail of the materials and geometry of the components due to a non-disclosure agreement with the University of Trieste. The entire geometry of the LINAC head and bunker has been drawn using the computer-aided design software *AutoCad*. Then, the compatible tool *MCNP Visual Editor* (MCNPXVised, version 22S) allowed to convert it into the format of an MCNP input file. In Figure 2.25b the main components of the accelerator's gantry modeled can be visualized and it is possible to distinguish the *target*, *primary collimator*, *flattening filter*, *ionization chamber* and the *jaws* along with their shielding structure.

Once the geometry of each cell was implemented, data cards were defined using information provided by the manufacturer and reported in literature to specify the material compositions. To simulate the presence of the patient, we added a geometry similar to the one of the phantom shown in Figure 2.13 used in the experimental sessions. A cylinder with an elliptical base simulates the patient's trunk. Inside it, we created measurement volumes in which the neutron fluence was studied. They are cylinders having the same radius as the phantom's channels (1 cm), a height of 3 cm Figure 2.26) and they were centered in the same points where, during the experiments, detectors were allocated. All volumes were filled with water.

Finally, two additional cells were included in the model to carry out further checks on the validity of the code. They consist in a sphere with a volume of 1 cm^3 centered about the LINAC isocenter and a cube made of air. The first one was used to estimate the photon absorbed dose at the isocenter and it was placed inside the phantom in correspondence with the actual isocenter set during the experiments. The second one, instead, was employed to verify if the energy spectrum of photon emerging from the target had the expected behaviour.

In the 'Data' section of the MCNP input file it was necessary to specify the desired outputs, i.e. the *tallies*, and the regions where they had to be computed. For the purpose of this work, we used:

- the **F4 neutron tally (f4:n)** to calculate the *neutron fluence* inside the volumes at the detectors' positions. The scored quantity had the units of particles·cm^{-2}·pr^{-1}, where *pr* stands for *primary particle simulated*;

- the **F4 photon tally (f14:p)** in order to verify if the photon spectrum in the cube located under the ionization chamber had physical sense;

- the **F6 electron tally (f6:e)** to estimate the *absorbed dose* at the isocenter. Specifically, it computes the electron energy deposition within a cell providing a more accurate result with respect to F6 photon tallies as it also includes the electrons produced close to the cell boundary and which could carry significant energy [78]. The result was expressed in MeV·g^{-1}·pr^{-1}.

Furthermore, to improve the statistical precision of the results and reduce the computational cost, the following variance reduction techniques were implemented: energy cut-off, cell importance and bremsstrahlung biasing. The lower energy cut-off was set to 10 keV for photons and 700 keV for electrons using the commands 'CUT:p j 0.01' and 'CUT:e j 0.7'. Hence, whenever a photon falls below 10 keV or an electron below 700 keV, they are killed by the simulation.

The second 'trick' is included in the category of *population control* methods. This means that the number of particles in cells where the importance was modified with respect to unit can be artificially increased/reduced. In our case, the neutron importance in the cells simulating the detectors was set to 10^6 and to 10^3 in the phantom. Most of the photons generated during the bremsstrahlung process have low energies and therefore have no relevant interest in the production of phototoneutrons. The use of the 'BBREM' card allows to bias the sampling of a bremsstrahlung photon between a specified energy range [78], and it was used to generate more high-energy photons, leading to a higher number of photoneutrons. It is important to remark that the code normalizes the particle weight in order to "cancel" the effect of these non-physical biases.

Note that MCNP normalizes the results for the total number of simulated primary particles (9×10^8 in our case). In this way the physics of the problem when these variance reduction techniques are applied is not altered.

(a)

(b)
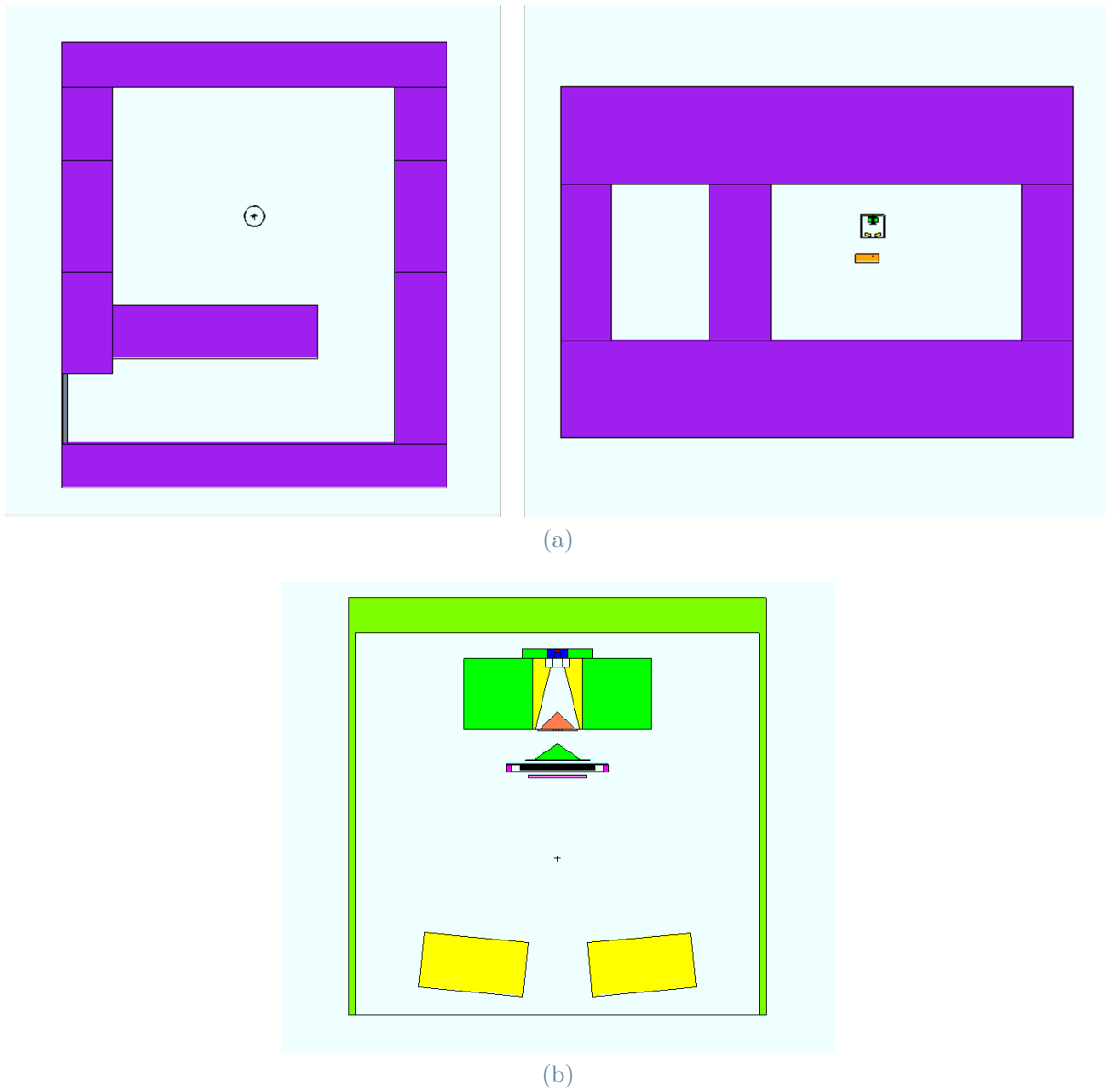
Figure 2.25: 2D visualization of the treatment room in the xy and xz planes (a) and the model of the LINAC head components in the xz plane.

(a)   (b)
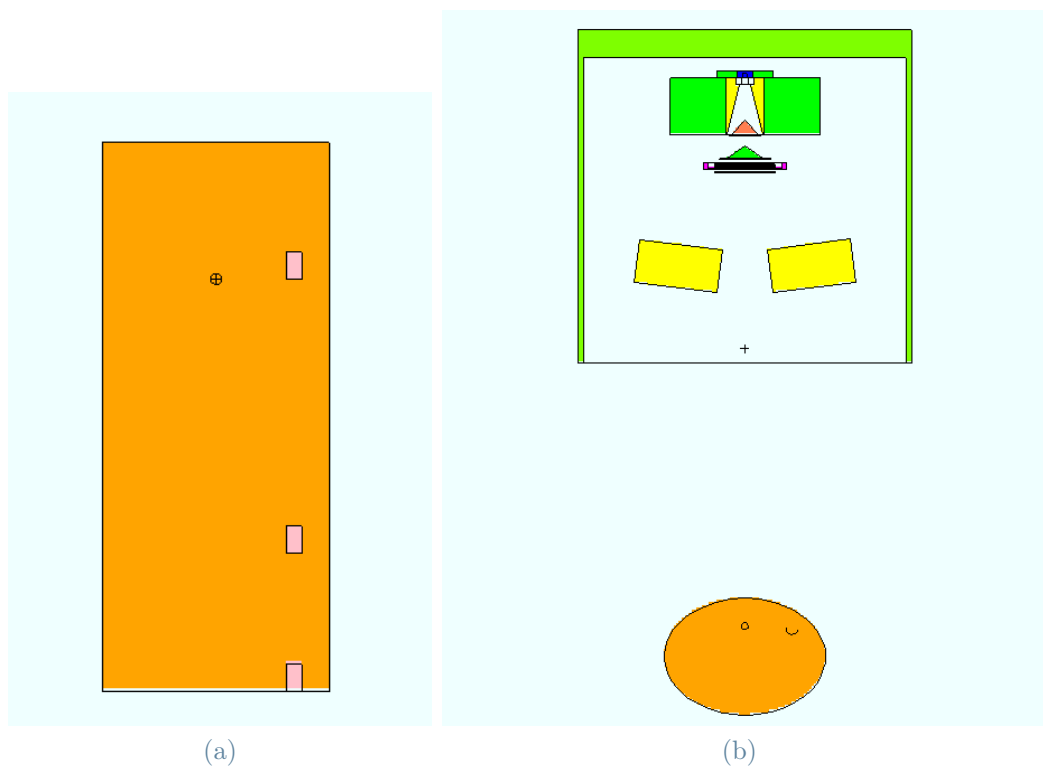
Figure 2.26: 2D visualization of the phantom geometry in the yx and yz plane. In particular, the pink rectangles in figure (a) represent the locations of the detectors used for the experimental measurements in the configuration used at ASUGI.

3 | Results and discussion

The purpose of this chapter is to describe the experimental sessions that were carried out at Politecnico di Milano, first, and in the various hospitals, afterwards, and to discuss the results obtained. In particular, attention will be paid to the calibration procedure of the devices involved in this work and to the measurement set-up that were used during the irradiation with the LINACs.

3.1. Calibration procedure of CR39 $+^{10}$B detectors

Before proceeding with the experimental measurements in the radiation field produced by the clinical LINACs it is essential to study the characteristics of the devices that will be involved. For the purposes of this work, as previously anticipated in Section 2.4, CR39 detectors from two manufacturers coupled to a thermal neutron converter made of ^{10}B were used and a series of measurements was performed in the thermal irradiation facility ESTHER at Politecnico di Milano to verify the linearity in the response of the detectors and assess their sensitivity to thermal neutrons. Since the PADC detectors came from two different manufacturers, it was necessary to repeat the procedure described below for each of them, but without substantial differences.

The exposures were performed by placing 25 RTP detectors and 12 TASL detectors on the lead plate located above the source of AmBe along a circumference in such a way that they were at an equal distance from the central axis and therefore were exposed to the same thermal neutron flux (φ_{th}) of 492 cm^{-2}s^{-1}. The uncertainty associated with this value is approximately 2%. The neutron spectrum of the source also has an epithermal component, while we are interested only in the thermal one, therefore among the exposed detectors there were 8 sandwiched between cadmium plates.

After 4, 8, 16 and 60 minutes an equal number of detectors (5 RTP and 3 TASL) were removed in order to evaluate the dependence of their response, in terms of *track density* [trk·cm^{-2}] on the thermal neutron fluence. They were subsequently chemically etched for 40 minutes and then analyzed using the Politrack® reader.

The *average background track density* was measured with 6 unexposed CR39 from RTP producer and 3 CR39 from TASL producer which were etched and analyzed together with the exposed ones. It is equal to, respectively, 237 ± 17 trk·cm^{-2} and 195 ± 24 trk·cm^{-2}.

The results are reported in Table 3.1, Table 3.2 and shown graphically in Figure 3.1. Note that the average background track density has already been subtracted from the ones reported in the tables.

TASL detectors

Time [min]	Fluence [cm^{-2}]	Detector code	Track density [trk·cm^{-2}]	Relative uncertainty
8	236160	5344	1953	7%
		5349	1813	7%
		5385	2260	6%
16	472320	5335	4346	3%
		5353	4335	3%
		5332	3954	3%
60	1771200	5351	14923	2%
		5383	14683	2%
		5354	13815	2%
		5348*	731	13%
		5382*	896	11%
		5379*	1055	9%

*The detectors were covered with Cd plates.

Table 3.1: Data for TASL detectors calibration.

The relative uncertainty reported in the table corresponds to one standard deviation, 1σ. The error bar refers to the sampling uncertainty of a given group of detectors composed with the background uncertainty (standard deviation of the non-irradiated CR39). Instead, the uncertainties on the fictitious calibration factors are returned by the LINEST function, summed in quadrature with the uncertainty of the calibration source and, finally, compounded to obtain those of the final calibration factor.

It can be noted that the hypothesis of a linear dependence between the detectors' response and the neutron fluence is satisfied, taking into account data uncertainties, for the detectors of both batches.

The calibration factor $f_{c,th}$ [n·trk^{-1}], to pass from track density to thermal neutron fluence, was then estimated through the Excel function *LINEST* which uses the method of *least squares* when fitting data. The devices used for the experimental measurement campaign provide a response in terms of track density therefore, we will have to multiply this value by the empirical coefficient $f_{c,th}$ in order to obtain the quantity of interest, that is the fluence of thermal neutrons to which they have been exposed.

The procedure followed for the calculation of the calibration factor consists of two steps:

RTP detectors

Time [min]	Fluence [cm⁻²]	Detector code	Track density [trk·cm⁻²]	Relative uncertainty
4	118080	M157244	912	6%
		M157214	610	9%
		M157198	749	7%
		M157245	797	7%
		M157226	705	8%
8	236160	M157234	1768	4%
		M157236	1751	4%
		M157248	1493	5%
		M157219	1965	4%
		M157209	1806	4%
16	472320	M157295	2829	4%
		M157287	3077	4%
		M157260	3037	4%
		M157277	3481	3%
		M157294	3303	3%
60	1771200	M157237	12166	4%
		M157201	13745	4%
		M157216	14361	4%
		M157249	13283	4%
		M157227	11593	4%
		M157275*	551	4%
		M157293*	487	4%
		M157269*	524	4%
		M157266*	529	4%
		M157286*	516	4%

* The devices were covered with two cadmium plates

Table 3.2: Data for RTP detectors calibration.

at first, data from detectors exposed to thermal and epithermal neutrons, i.e. the ones without cadmium cover, are fitted using the least squares method by a straight line. The inverse of its angular coefficient gives a fictitious estimate of the CR39 detectors' sensitivity to thermal and epithermal neutrons, $f_{c,th+epi}$. Then, data from detectors which were covered with cadmium during the exposure are analyzed likewise and a fictitious calibration factor to epithermal neutrons is derived, $f_{c,epi}$. Finally, the actual thermal calibration factor, $f_{c,th}$, is calculated by subtracting the previous two. It is only the latter that represents a real physical quantity, since the previous coefficients ($f_{c,th+epi}$ and $f_{c,epi}$) are obtained as the ratio between a track density, from exposure to thermal and epithermal neutrons the former and only thermal neutrons the latter, and a purely thermal fluence ($\frac{\text{Track density}_{th+epi}}{\varphi_{th}}$ and $\frac{\text{Track density}_{epi}}{\varphi_{th}}$).

This procedure yielded a calibration factor (f_c) for the RTP and TASL detectors of respectively 142.57 ± 3.9 n·trk⁻¹ and 129.52 ± 3.4 n·trk⁻¹.

RTP detectors calibration curve

(a)

TASL detectors calibration curve

(b)
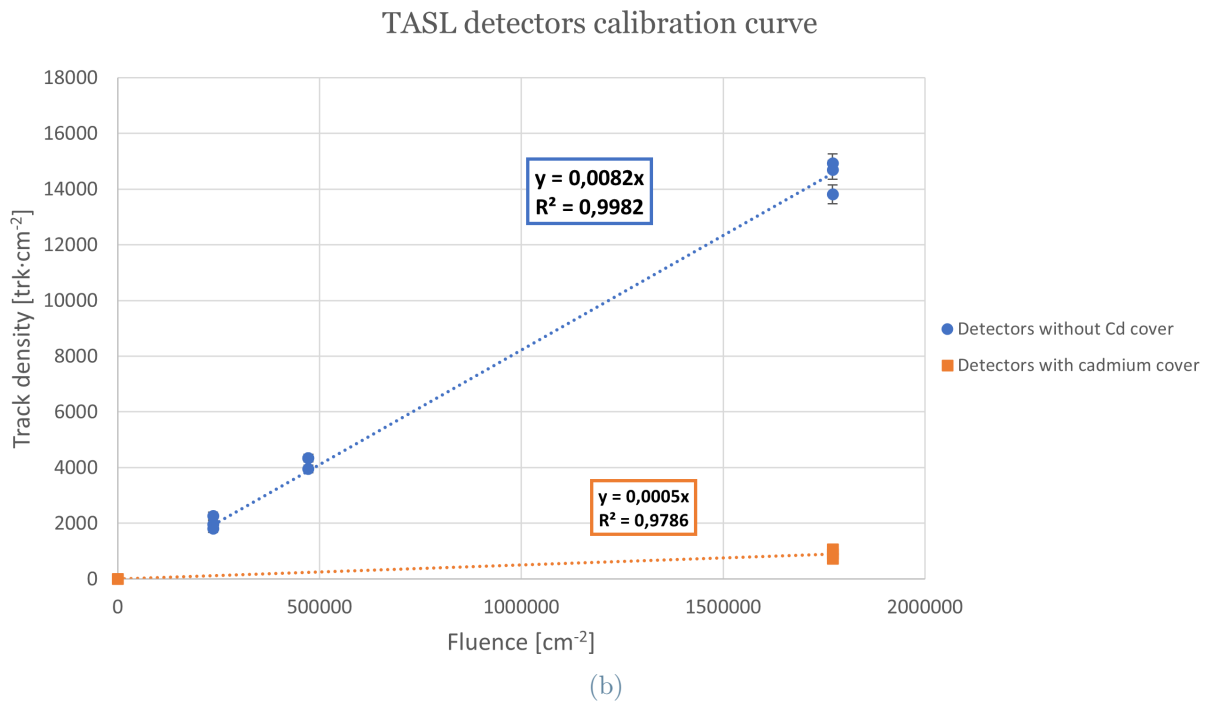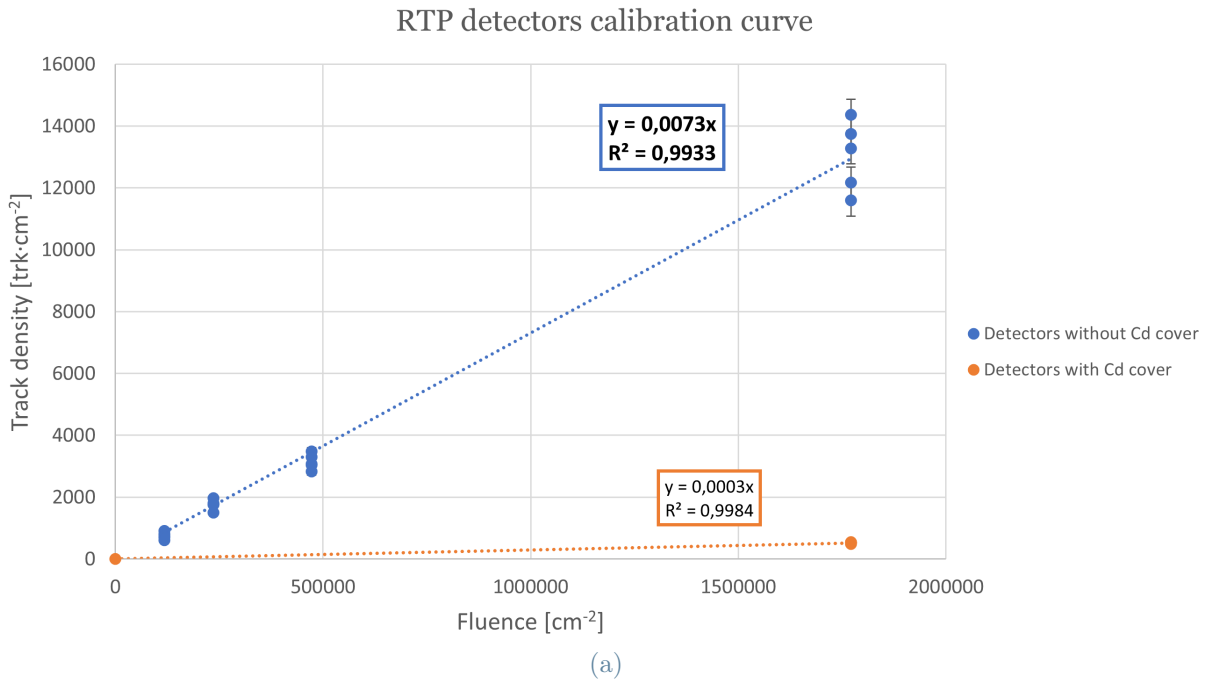
Figure 3.1: Calibration curves for RTP and TASL detectors. It is possible to observe, in blue, the data from detectors exposed without the Cd cover and the curve which best fits them, while, in orange, are shown data from detectors exposed with the Cd cover and their fitting curve. The inverse of the angular coefficients of the curves shown in the graphs are $f_{c,th+epi}$ (curve in blue) and $f_{c,epi}$ (curve in orange).

3.2. Experimental measurements campaign

The main goal of the present work was to assess the thermal neutron fluence to which patients undergoing high-energy RT treatments, involving X-rays beams with energies higher than 10 MV, are exposed. Specifically, the area where a CIED device is usually implanted had to be investigated. It was achieved by inserting the detectors inside the channels of the BOMAB-like phantom and delivering realistic RT treatment plans to it.

3.2.1. Ospedale di Circolo e Fondazione Macchi (ASST-VA)

The RT treatments simulated at ASST-VA are reported in Table 3.3, while Figure 3.2 shows how they were planned using the TPS. Those were chosen in agreement with the medical physicist working in the hospital where the experimental campaign was carried out as they involve radiation beams with very high energies (18 MV) and the area to be treated, i.e. a vertebra, is very close to the one of our interest. The *Clinac DHX Varian* hosted at ASST-VA hospital was used in clinical mode and the field size was set to 10x10 cm^2. During the experiments, the BOMAB-like phantom filled with water simulated the

Treated area	MU delivered at isocenter	Energy [MV]	Measuring position
Vertebra	20	18	Channel no. 1, *CIED* position
	40		
	100		

* The devices were covered with two cadmium plates

Table 3.3: RT treatments investigated at ASST-VA

human trunk and the detectors were inserted inside the channel no. 1 (Figure 2.13), 16 cm from the upper base. In particular, to improve the statistics, a single boron sheet sandwiched between two CR39 at a time was used. In the channels there were PMMA spacers to define more precisely the position of the detectors and fill the remaining empty space.

It is important to notice that during those experiments it was not possible to perform measurements using the Cd plates in order to subtract the contribute associated to the epithermal component of the neutron spectrum from the total one, because they were not available. However, the results obtained are still meaningful for two main reasons:

- the boron absorption cross section is considerably reduced in the range of epithermal energies (it decreases following the *1/v* law) making, *de facto*, the device less sensitive to epithermal neutrons;

- the thermal component of the neutron spectrum inside the water phantom prevails over the epithermal one; it was also confirmed by MCNP simulations.
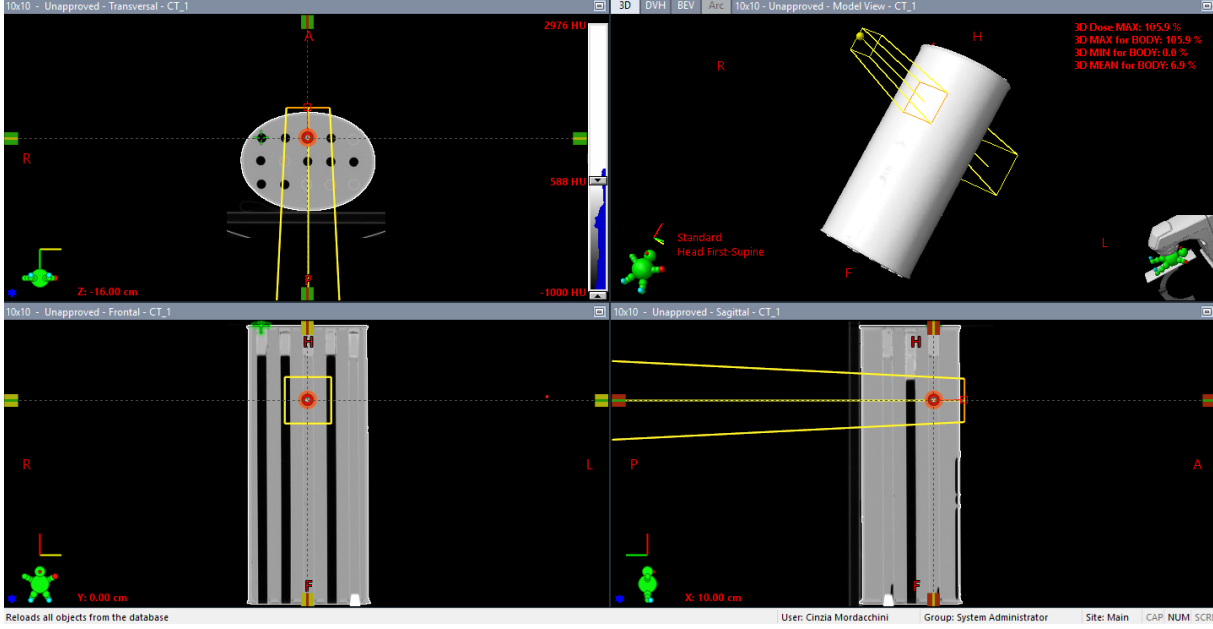
Figure 3.2: User interface of the TPS used at ASST-VA to plan the treatment delivered during the experiments.

Results are reported in Table 3.4: they show the thermal neutron fluence ($\Phi_{n,th}$) per MU delivered during the treatment.

Energy [MV]	MU delivered at isocenter	$\frac{\text{Track density}}{\text{MU}}[\frac{\text{trk}}{\text{cm}^2\text{MU}}]$	$\frac{\Phi_{n,th}}{\text{MU}}$ $[\frac{1}{\text{cm}^2\text{MU}}]$	Relative uncertainty
	20	1225	1.75×10^5	4%
18	40	1143	1.63×10^5	5%
	100	634	9.03×10^4	3%

Table 3.4: Results obtained at ASST-VA for the 18 MV vertebra treatment at CIED site in terms of track density and thermal neutron fluence per MU.

The uncertainties associated to the thermal neutron fluence was estimated using the error propagation formula (Equation (3.1)) to combine the uncertainty related to the density of tracks of a detectors couple - computed as the sample standard deviation - and the uncertainty on the calibration factor:

$$\sigma_u^2 = \left(\frac{\partial u}{\partial x}\right)^2 \cdot \sigma_x^2 + \left(\frac{\partial u}{\partial y}\right)^2 \cdot \sigma_y^2 \tag{3.1}$$

(a)   (b)   (c)
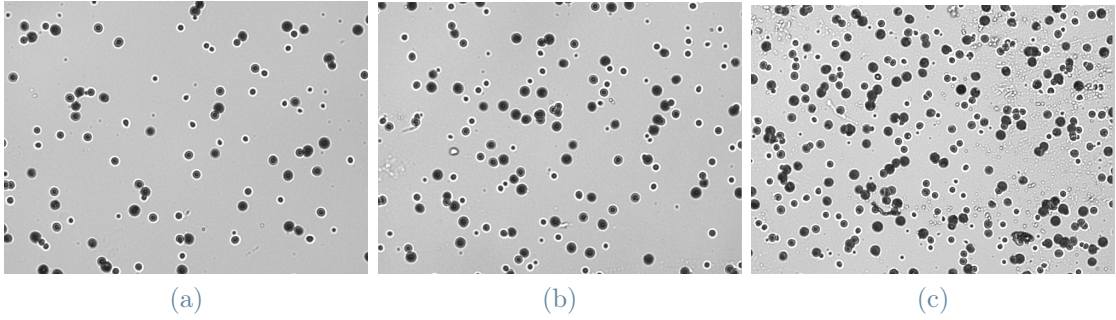
Figure 3.3: Image frame acquired using the Politrack® system of CR39 exposed during a 20, 40 and 100 MU treatment.

where x and y are independent variables and σ_x and σ_y their standard deviations.

It can be observed that the order of magnitude of the estimated fluence is almost the same ($\sim 10^5 \frac{n}{cm^2 MU}$), except for the one, measured by the detector labelled with the code C, which is slightly lower. This is due to CR39 saturation that occurs at very high track density levels ($> 60,000 \ tr/cm^2$), e.g. Figure 3.3c, where the built-in correction algorithm of the reader for track overlapping corrections becomes less effective.

3.2.2.   Azienda Sanitaria Universitaria Giuliano Isontina (ASUGI)

Table 3.5 includes the information about the RT treatments delivered at ASUGI. The area to be treated was chosen to be the iliac wing since it is located in a distal region with respect to the one where a CIED is implanted and requires high-energy photon beams. Indeed, the purpose in this experiment was to study the thermal neutron fluence when the CIED area is outside the primary radiation beam.

The detector was placed inside the channel no.1 of the BOMAB-like phantom, which was filled in paraffin, along with PMMA spacers in the channel to hold it in place. The measuring position chosen was the same of the experiments carried out at ASST-VA, that is a few centimeters from the upper base of the phantom ('CIED position' in Table 3.5). In addition to this, two more measurements were performed placing the detectors along the same channel, but the first one near the isocenter ('isocenter position' in Table 3.5) and the other at an equal distance from the first two ('intermediate position' in Table 3.5), as it can observed in Figure 3.4. This choice aims to study the spatial distribution of thermal neutron fluence in the phantom, which goes outside the present work, but could be further investigated in the future.

During those experiments the *Elekta Sinergy* LINAC was used in photon mode and the

isocenter was set inside the hypothetical tumor region (Figure 3.5).

Treated area	MU delivered at isocenter	Energy [MV]	Measuring position
Iliac wing	50	15	Channel no.5, *CIED* position (detector code: 14)
			Channel no. 5, *isocenter* position (detector code: M)
			Channel no. 5, *intermediate* position (detector code: A)
	300		Channel no. 5, *CIED* position (detector code: N)*
			Channel no. 5, *isocenter* position (detector code: 8)*
			Channel no.5, *intermediate* position (detector code: G)*

* The devices were covered with two cadmium plates

Table 3.5: RT treatments investigated at ASUGI (TS).
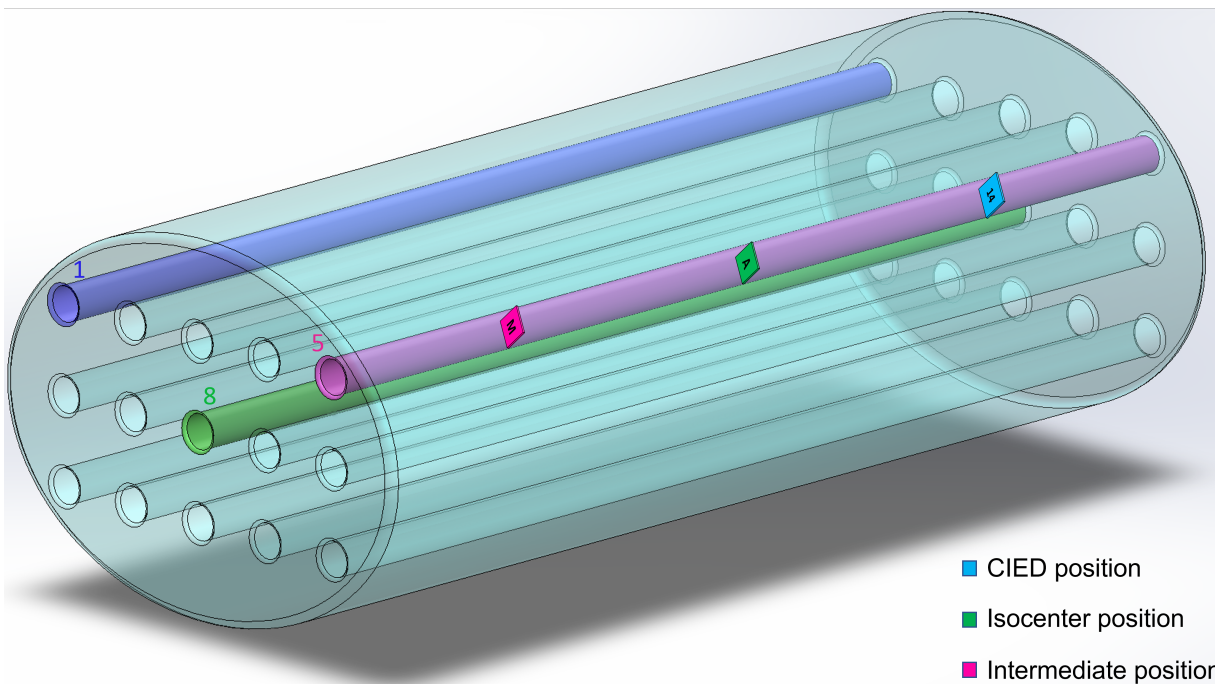
Figure 3.4: Schematic representation of the BOMAB-like phantom simulating the human trunk which was used during the experimental campaign with the detectors placed inside the channel no.5. Detectors are identified by a code and associated with it to their position.

The results of this measurements are reported in Table 3.6. From a direct comparison with data in Table 3.4 it is possible to notice a reduction of approximately a factor of 2 in the thermal neutron fluence measured at ASUGI at the CIED position.

Moreover, it is important to observe that there are not major variations of the fluence along the phantom's channel, although it is higher near the isocenter.

It is worth mentioning that during these experiments a single CR39 was used per measurement, therefore it was not possible to estimate uncertainties as the sample standard deviation. Therefore, only the uncertainty associated with the Poisson distribution of the track density, composed as usual with the one of the calibration factor, was taken into account.

Energy [MV]	Measuring position	$\frac{\text{Track density}}{\text{MU}}$ $[\frac{\text{trk}}{\text{cm}^2\text{MU}}]$	$\frac{\Phi_{n,th}}{\text{MU}}$ $[\frac{\text{n}}{\text{cm}^2\text{MU}}]$	Relative uncertainty
15	Channel no. 5, *intermediate* position	220	2.85×10^4	3%
	Channel no. 5 *isocenter* position	613	7.94×10^4	3%
	Channel no. 5, *CIED* position	482	6.24×10^4	3%

Table 3.6: Results obtained at ASUGI for the iliac wing treatment in terms of track density and thermal neutron fluence per MU. The highlighted row refers to the CIED position and it has to be compared to the corresponding one in Table 3.9.

3.2.3. Ospedale San Luca

At Ospedale San Luca, the RT treatments in Table 3.7 and Table 3.8 were investigated. For the first experiment the same measurement conditions described in Section 3.2.2 were reproduced since we wanted to verify if accelerators of the same manufacturer and model (placed in similar bunkers/treatment rooms) produced the same thermal neutron fluence. However, detectors were placed in a slightly different way: the one of interest for this work was collocated at the CIED position in channel no.1, analogously to the experiments carried out at ASUGI. While the others were disposed in channel no. 8 according to the set-up illustrated in Figure 3.4. This choice was made because channel 8 is the one that intercepts the isocenter and therefore allows to study the neutron fluence in the regions closest to it and therefore are supposed to be more contaminated by neutrons. Furthermore, it was possible to evaluate the fluence distribution along the axis of the phantom.

In the second experiment a RT treatment to the left breast was simulated. Nowadays, in clinical practice, attempts are made to avoid using high-energy radiation beams (> 6MV) if the patient has a CIED and needs to undergo such treatments. However, in some cases, such as for example that of a thick breast, this is necessary and the measures we carried

out are of interest in this regard. For the reasons explained above, the *Elekta Sinergy* accelerator was used in clinical mode and X-ray beams at two energies, 10 and 15 MV, were used. The devices were placed in channels no. 1 (directly underneath the irradiated breast) and no. 5 (below the contralateral breast with respect to the treated one) a few centimeters deep from the upper base of the phantom, in the CIED position. Two breasts made of tissue equivalent material were placed on the phantom.

Treated area	MU delivered at isocenter	Energy [MV]	Measuring position
Iliac wing	50	15	Channel no. 5, *CIED* position (detector code: F)
			Channel no. 8, *isocenter* position (detector code: E)
			Channel no. 8, *intermediate* position (detector code: 7)
			Channel no. 8, *CIED* position (detector code: 12)
	200		Channel no. 5, *CIED* position (detector code: B)*
			Channel no. 8, *isocenter* position (detector code: G)*
			Channel no. 8, *intermediate* position (detector code: H)*
			Channel no. 8, *CIED* position (detector code: L)*

* The devices were covered with two cadmium plates

Table 3.7: RT treatments investigated at San Luca Hospital (LU).

Treated area	MU delivered at isocenter	Energy [MV]	Measuring position
Breast	80	10	Channel no. 1, *CIED* position (detector code: M)
			Channel no. 5, *CIED* position (detector code: C)
	400		Channel no. 1, *CIED* position (detector code: D)*
			Channel no. 5, *CIED* position (detector code: 8)*
	40	15	Channel no. 1, *CIED* position (detector code: 13)
			Channel no. 5, *CIED* position (detector code: A)
	200		Channel no. 1,*CIED* position (detector code: F)*
			Channel no. 5, *CIED* position (detector code: 14)*

* The devices were covered with two cadmium plates

Table 3.8: RT treatments investigated at San Luca Hospital (LU).
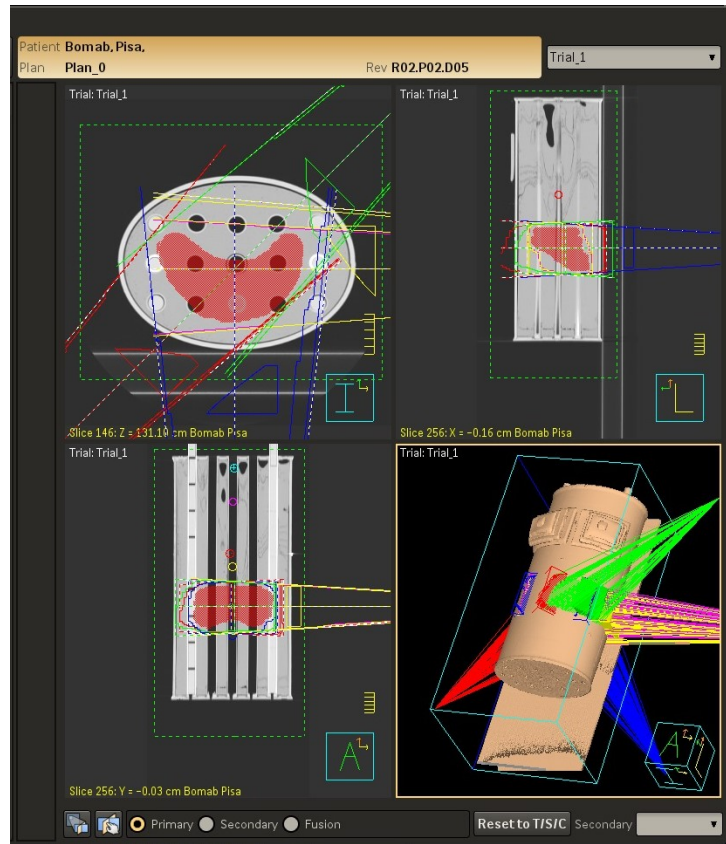
Figure 3.5: User interface of the TPS used at Ospedale San Luca and ASUGI to plan the iliac wing treatment delivered during the experiments.

Results are reported in Table 3.9 and Table 3.10 together with their uncertainty, corresponding to 1σ, calculated ad explained in Section 3.2.2.

Energy [MV]	Measuring position	$\frac{\text{Track density}}{\text{MU}}[\frac{\text{trk}}{\text{cm}^2\text{MU}}]$	$\frac{\Phi_{n,th}}{\text{MU}}[\frac{\text{n}}{\text{cm}^2\text{MU}}]$	Relative uncertainty
15	Channel no. 5, *CIED* position	526	6.81×10^4	9%
	Channel no. 8, *CIED* position	253	3.28×10^4	3%
	Channel no.8, *isocenter* position	384	4.98×10^4	3%
	Channel no. 8, *intermediate* position	286	3.70×10^4	3%

Table 3.9: Results obtained at Ospedale San Luca for the iliac wing treatment in terms of track density and thermal neutron fluence per MU. The highlighted row contains data that have to be compared to their corresponding ones in Table 3.6.

The results follow the same trend as those previously described in Section 3.2.2. In detail, it has been verified that the same treatment delivered using accelerators of the same

Energy [MV]	Measuring position	$\frac{\text{Track density}}{\text{MU}}[\frac{\text{trk}}{\text{cm}^2\text{MU}}]$	$\frac{\Phi_{\text{n,th}}}{\text{MU}}$ $[\frac{\text{n}}{\text{cm}^2\text{MU}}]$	Relative uncertainty
10	Channel no. 1, CIED position	84	$1.09{\times}10^4$	2%
	Channel no. 5, CIED position	57	$7.38{\times}10^3$	4%
15	Channel no. 1, CIED position	280	$3.62{\times}10^4$	3%
	Channel no. 5, CIED position	185	$2.39{\times}10^4$	7%

Table 3.10: Results obtained at Ospedale San Luca for the breast treatment in terms of track density and thermal neutron fluence per MU.

manufacturer and model generates a completely comparable neutron fluence ($6.24{\times}10^4 \pm$ 1162 n·cm^{-2}·MU^{-1} vs $6.81{\times}10^4 \pm$ 1554 n·cm^{-2}·MU^{-1}).

While the measurements performed placing the detectors in channel no. 8 highlighted an increasing trend of the thermal neutron fluence as we get closer to the isocenter, even if the order of magnitude is the same in each case and to the one observed at ASUGI.

Finally, data related to the breast treatment, once again, confirm what has been said so far: the CIED is exposed to a thermal neutron fluence of the order of $\sim 10^5$ n·cm^{-2}·MU^{-1} and it is always a little bit higher at the isocenter.

3.3. Validation of the computational model

In this section we will show the results of the measurements carried out during the experiments aimed at validating the computational model described in Section 2.5 and we will compare them with data obtained in the simulations.

To fulfill this purpose a benchmark treatment (Table 3.11) was delivered by the accelerators at ASUGI and Ospedale San Luca [1]. The thermal neutron fluence was measured using the same detectors described before which were placed inside the phantom according to the configuration illustrated in the previous sections (3.2.2 and 3.2.3) and shown in Figure 3.6. The photon dose at the isocenter, instead, was calculated with the Treatment Planning System *Oncentra*.

The main results obtained through our code and which demonstrated that it is able to reproduce the physics of the problem quite accurately are:

---

[1]It should be noted that in the simulations the differences between the bunkers of the two hospitals are assumed to be negligible as the two have a similar structure.

Detection system	Energy [MV]	Field size [cm²]	Isocenter	SSD [cm]	MU
CR39+^{10}B	15	30x30	15 cm from the bottom of the phantom 4.5 cm deep from the surface	95.5	50
CR39+^{10}B+Cd					200

Table 3.11: Summary of the information about the experiment for the validation of the Monte Carlo code held in Trieste and Lucca hospitals.
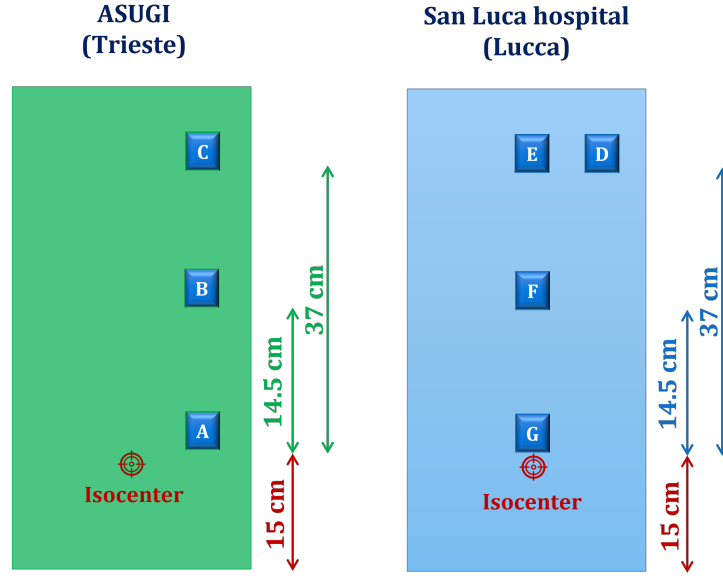
Figure 3.6: Schematic representation of the detectors' arrangement inside the phantom during the experimental measurements for the validation of the computational code. This set-up is the one simulated in MCNP.

- the *photon fluence spectrum* measured before they cross the jaws inside the LINAC's head, shown in Figure 3.7. Since photons are mainly produced by Bremmstrhlung within the tungsten target, the spectrum is shifted towards lower energies and decreases to zero up to the maximum achievable energy via the simulated accelerator (15 MV). Furthermore, an annihilation peak can be observed at around 511 keV.

- the *photoneutrons spectra* calculated at different positions located inside the phantom and that are illustrated in Figure 3.8. They are both characterized by two main peaks, the first one at thermal energies ($\sim 10^{-1}$ eV) and the second one, quite smaller, in the fast energy region (~ 1 MeV) demonstrating that the thermal component of the neutron field inside the patient body prevails over the epithermal and fast ones. Besides, the results of the simulations show that this spectrum is not subject to major changes if measured at different points along the major axis of the phantom, confirming what was observed experimentally, except for a slight increase at the isocenter.

In both cases the trend is confirmed by studies reported in literature, e.g. [67] and [80].
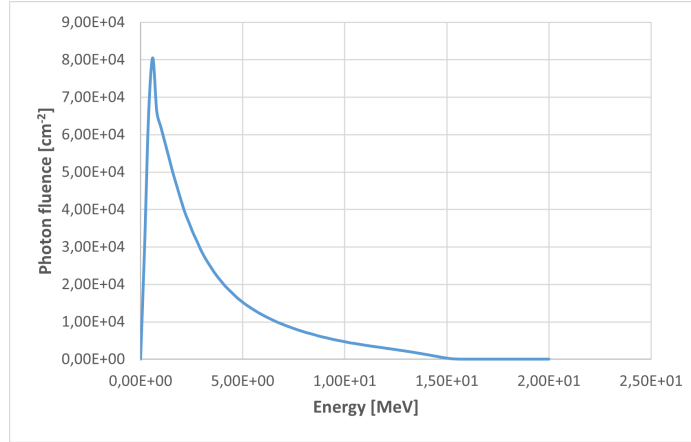
Figure 3.7: Photon fluence spectrum produced by a 15 MV Elekta Sinergy linear accelerator, measured before crossing the jaws.

In addition to this, a comparison between the experimental and simulated data was done by considering the ratio of the thermal neutron fluence ($\Phi_{n,th}$) to the absorbed photon dose at the isocenter ($dose_{ph}$). Results are summarized in Table 3.12, and Figure 3.9.

MCNP vs ASUGI (Trieste)

Measuring position	$\frac{\Phi_{n,th}^{exp}}{dose_{ph}^{exp}}\left[\frac{n}{cm^2 \cdot Gy}\right]$	Relative uncertainty (1σ)	$\frac{\Phi_{n,th}^{MCNP}}{dose_{ph}^{MCNP}}\left[\frac{n}{cm^2 \cdot Gy}\right]$	Relative uncertainty (1σ)	Error % $\left[\frac{data_{exp} - data_{MCNP}}{data_{exp}}\right]$
A	3.84×10^6	3%	9.98×10^6	2%	62%
B	1.27×10^6	3%	5.05×10^6	3%	75%
C	1.60×10^6	3%	1.97×10^6	3%	19%

MCNP vs San Luca Hospital (Lucca)

Measuring position	$\frac{\Phi_{n,th}^{exp}}{dose_{ph}^{exp}}\left[\frac{n}{cm^2 \cdot Gy}\right]$	Relative uncertainty (1σ)	$\frac{\Phi_{n,th}^{MCNP}}{dose_{ph}^{MCNP}}\left[\frac{n}{cm^2 \cdot Gy}\right]$	Relative uncertainty (1σ)	Error % $\left[\frac{data_{exp} - data_{MCNP}}{data_{exp}}\right]$
G	6.35×10^6	3%	8.29×10^6	2%	23%
F	5.03×10^6	3%	5.97×10^6	2%	16%
E	2.26×10^6	4%	3.03×10^6	2%	32%
D	1.07×10^6	5%	9.37×10^5	6%	-14%

Table 3.12: Comparison between the results obtained by Monte Carlo simulations and through experimental measures at ASUGI (Trieste) and San Luca Hospital (Lucca). The measuring positions refer to detectors code in Figure 3.6.

The MC code generally overestimates the calculated ratios: for example, we can observe that between the ratios referring to measurement positions A and B there is a difference

of a factor 3. However, for the remaining points considered, the agreement is quite good and in any case the order of magnitude is the same. Moreover, it predicts the expected decreasing trend of the quantities under investigation when we move away from the isocenter. The relative uncertainty corresponding to 1σ is about 3% for 9×10^8 primary electrons simulated.

(a)

(b)
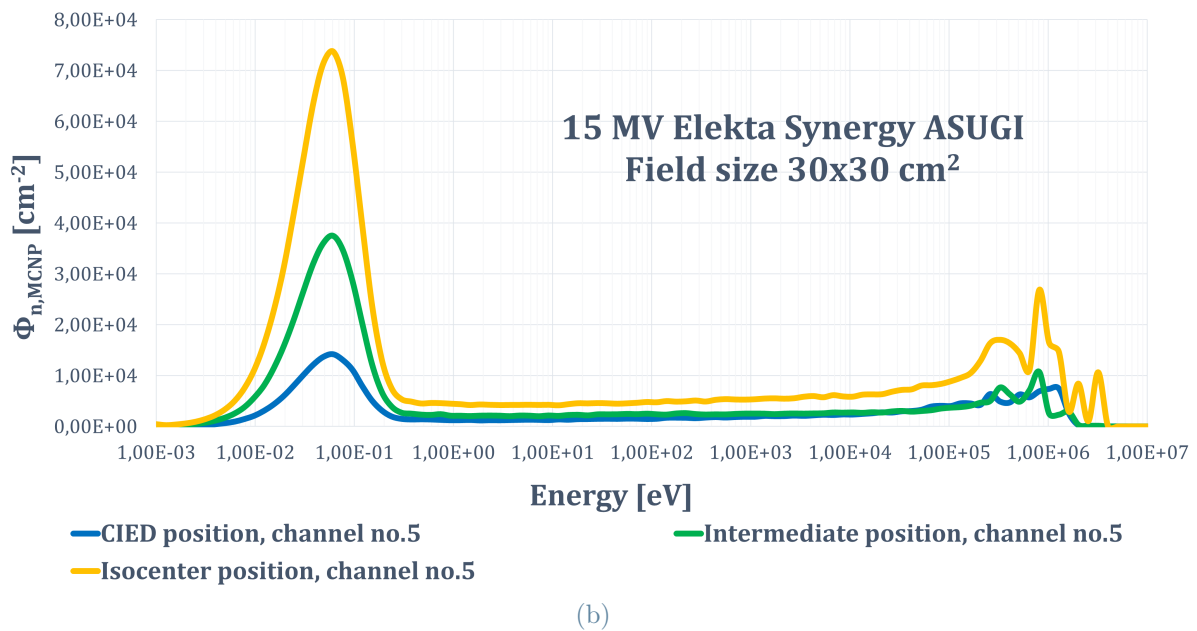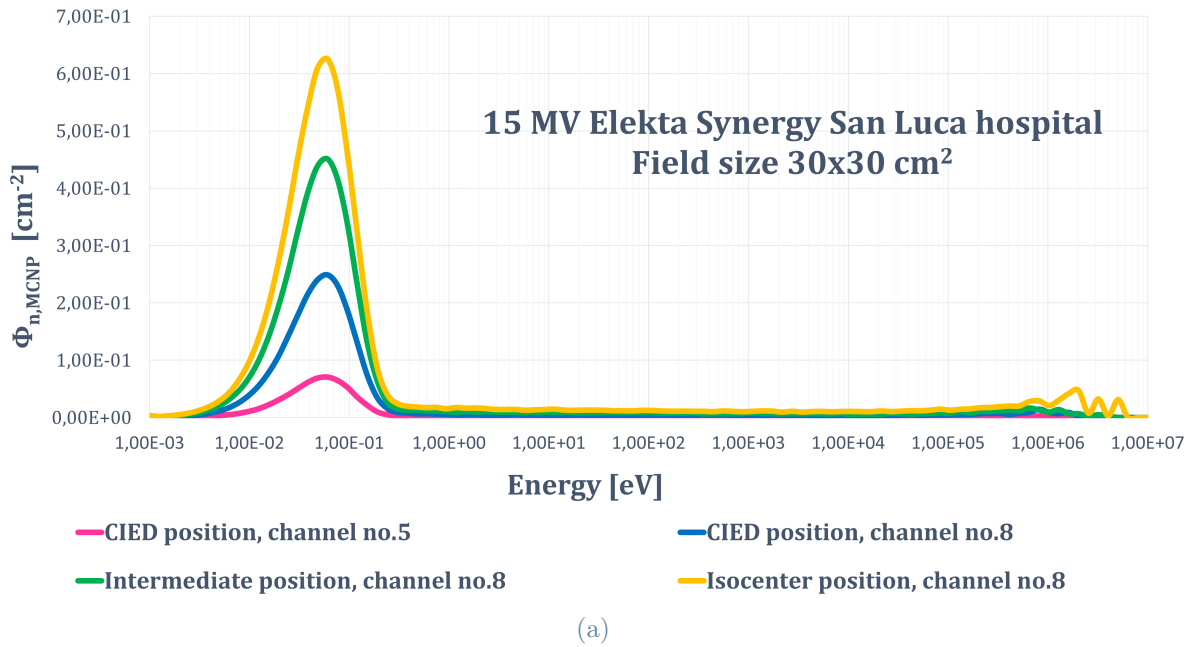
Figure 3.8: Photoneutron spectra computed at different position inside the patient's body obtained using MCNP.
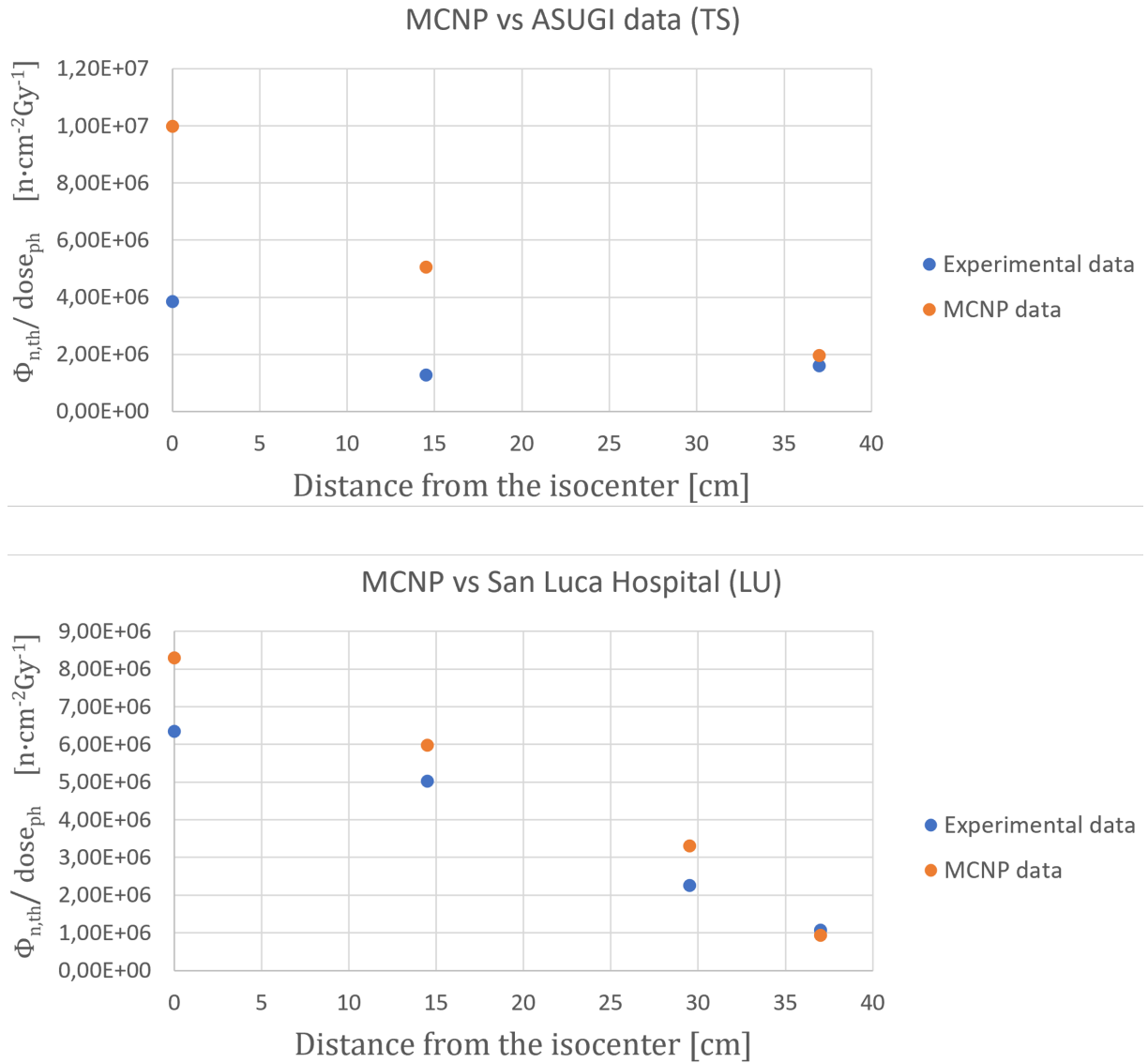
Figure 3.9: The figure contains two graphs that illustrate the comparison between data obtained through experimental measurements in different points of the phantom and those calculated in the same points through Monte Carlo simulations. Error bars not shown because they would hardly visible.

4 | Conclusions and developments

The aim of the present work was to measure the thermal neutron fluence that contaminates the primary radiation field produced by a LINAC and to which a patient can be exposed if he were to undergo a radiotherapy treatment with high-energy X-ray beams. Specifically, we wanted to estimate its value in the area where a CIED is implanted to make a comparison with the one above which it has been experimentally tested that damages to the devices can be induced ($\sim 10^9 \ \frac{\text{n}}{\text{cm}^2}$) [53].

The study was subdivided into two parts, an experimental one and a computational one. During the experimental measurement campaign, real treatment plans were simulated on a phantom within which the previously described neutron detectors were arranged.

Our results showed that the measured value of the quantity of interest is of the order of $\sim 10^5 \ \frac{\text{n}}{\text{cm}^2 \text{MU}}$ for the case examinated. Therefore, considering that in a normal course of radiotherapy a patient receives a dose of about 30 Gy (100 MU = 1Gy) in fractions of 2 Gy each, the thermal neutron fluence is below the one indicated above as certainly critical.

From the study of the spatial distribution of neutron fluence along the axis of the phantom, it emerged that this is approximately constant, although an increase is observed at the position where the isocenter is located.

This work lays the foundations for several possible future studies, the most important of which would certainly be the investigation of the direct damages to cardiac devices when exposed to thermal neutrons fluences of the same order of magnitude we measured. In addition to this, it would be interesting to investigate the effects of the most modern techniques for administering radiotherapy treatments on electronic devices, e.g. IMRT, VMAT or hadrontherapy. Specifically, the latter is very often used to treat tumors in pediatric patients with various types of electronic implants, therefore a study in this sense assumes considerable importance.

In the second part of the work, the computational model of a LINAC head was optimized to include a phantom simulating the presence of a patient in the treatment room, using

the MCNP software. The code was validated by means of experimental thermal neutron fluence measurements inside the phantom along its major axis. They were performed in two different hospitals where accelerators of the same model as the one simulated are installed. The obtained results look very promising as the simulation describes quite faithfully the radiation transport problem, specifically for the electron-photon-neutron case as we observed in Section 3.3.

Among the future developments of this Monte Carlo model there is the possibility of improving the phantom's model. For example, it could be done by simulating an anthropomorphic voxel phantom through which it would be possible to model the patient with a high degree of detail. Furthermore, the detectors used for the experimental measurements should be reproduced with greater fidelity to verify if there is an improvement in the results obtained in this work. Finally, one of the most ambitious goal is to use the code to simulate real treatment plans with the aim of performing risk analysis to which a patient could be exposed as well as to estimate desired dosimetric quantities either inside the treatment room or in the patient's body.

Bibliography

[1] "World Health Organization (WHO) main page," Accessed March 27, 2022. Available at: `https://www.who.int/`.

[2] M. G. Fradley *et al.*, "How to Manage Patients With Cardiac Implantable Electronic Devices Undergoing Radiation Therapy," *JACC Cardio Oncology*, vol. 3, pp. 447–451, September 2021.

[3] G. Stefano Luigi Maria, "Lecture notes from the course *Medical application of radiation fields*," 2020.

[4] J. J. Duderstadt and L. J. Hamilton, *Nuclear Reactor Analysis*. Wiley New York, 1976.

[5] E. M. A. Hussein, *Radiation Mechanics - Principles Practice*. Elsevier Science, 2007.

[6] J. R. Lamarsh, A. J. Baratta, and H. Prentice, *Introduction to Nuclear Engineering Third Edition*.

[7] G. F. Knoll, *Radiation detection and measurement*. John Wiley Sons Inc, 2010.

[8] "Nuclear Energy Agency (NEA) - JANIS," Accessed February 2022. Available at: `https://www.oecd-nea.org/jcms/pl_39910/janis`.

[9] E. J. Hall *et al.*, *Photoneutrons From Medical Linear Accelerators-Radiobiological Measurements And Risk Estimates*, vol. 33. 1995.

[10] *Handbook on Photonuclear Data for Applications Cross-sections and Spectra*. No. 1178 in TECDOC Series, Vienna: International Atomic Energy Agency, 2000.

[11] Hashemi *et al.*, "A study of the photoneutron dose equivalent resulting from a Saturne 20 medical linac using Monte Carlo method," *Nukleonika*, vol. 52, pp. 39–43, 01 2007.

[12] I. Gudowska, "Photonuclear processes in the treatment room and patient during radiation therapy with 50 mv photons," 1997.

[13] A. Zanini *et al.*, "Monte carlo simulation of the photoneutron field in linac radiother-

apy treatments with different collimation systems," *Physics in Medicine and Biology*, vol. 49, pp. 571–582, January 2004.

[14] "NCRP Report 116 - Limitation of exposure to ionizing radiation," tech. rep., National Council on Radiation Protection and Measurements, 1993.

[15] P. Allen and M. Chaudhri, "Photoneutron production in tissue during high energy bremsstrahlung radiotherapy," *Physics in Medicine and Biology*, vol. 33, pp. 1017–1036, September 1988.

[16] S. Guo and P. L. Ziemer, *An evaluation of the activation products in a 25 MV linear accelerator and the potential for personnel doses Health Physics Aspects of Neutron Activated Components in a Linear Accelerator*. Health Phys.86(Supplement 2):S94–S102, 2004.

[17] A. Alem-Bezoubiri *et al.*, "Monte carlo estimation of photoneutrons spectra and dose equivalent around an 18mv medical linear accelerator," *Radiation Physics and Chemistry*, vol. 97, pp. 381–392, 4 2014.

[18] B. Ishkhanov and I. Kapitonov, "Giant dipole resonance of atomic nuclei. Prediction, discovery, and research," *Physics-Uspekhi*, vol. 64, pp. 141–156, may 2021.

[19] "Radiation Therapy for Cancer - National Cancer Institute," Accessed February 2022. Available at: `https://www.cancer.gov/about-cancer/treatment/types/radiation-therapy`.

[20] *Radiation Oncology Physics*. Non-serial Publications, Vienna: International Atomic Energy Agency, 2005.

[21] S. Gianfaldoni *et al.*, "An overview on radiotherapy: from its history to its current applications in dermatology," *Open Access Macedonian Journal of Medical Sciences*, vol. 5, pp. 521–525, 2017.

[22] *Radiotherapy in Cancer Care: Facing the Global Challenge*. Non-serial Publications, Vienna: International Atomic Energy Agency, 2017.

[23] I. I. C. on Radiation Units and Measurements), "Report 85: Fundamental quantities and units for ionizing radiation," tech. rep., October 2011.

[24] ICRP (International Commission on Radiation Protection), "Annals of the ICRP Published on behalf of the international Commission on Radiological Protection," tech. rep., 2007.

[25] K. Prasad, *Handbook of radiobiology (2nd ed.)*. CRC Press, 1995.

[26] M. Mariani, "Lecture notes from the course *Radiochimica Applicata*," 2021.

[27] "Structure and function of rna | microbiology," Accessed April,10 2022. Available at: `https://courses.lumenlearning.com/microbiology/chapter/structure-and-function-of-rna/`.

[28] E. M. Zeman, "The Biological Basis of Radiation Oncology PART A Radiobiology," 2021.

[29] "Institute of Nuclear and Particle Physics main page," Accessed February 2022. Available at: `https://inpp.ohio.edu/~inpp/`.

[30] "Cell Survival Curves | Radiology Key," Accessed February 2022. Available at: `https://radiologykey.com/cell-survival-curves/`.

[31] T. T. Puck and M. Philip I., "Action of x-rays on mammalian cells," *Journal of Experimental Medicine*, vol. 103, pp. 653–666, 05 1956.

[32] J. Coderre, "Principles of Radiation Interactions," Fall 2004. License: Creative Commons BY-NC-SA.

[33] Bogart, A. Jeffrey, *et al.*, *Clinical Radiation Oncology*. Elsevier, fourth edition ed., 2016.

[34] R. G. Syljuåsen, *Cell Cycle Effects in Radiation Oncology*. Cham: Springer International Publishing, 2019.

[35] G. Schwarz, "über desensibiliserung gegen röntgen- und radiumstrahlen," 1909.

[36] B. M. Sutherland *et al.*, "Clustered dna damages induced by high and low let radiation, including heavy ions," *Physica Medica*, vol. 17, no. SUPPL. 1, pp. 202–204, 2001.

[37] H. Paganetti, "Significance and implementation of rbe variations in proton beam therapy," *Technology in Cancer Research & Treatment*, vol. 2, no. 5, pp. 413–426, 2003.

[38] ICRP (International Commission on Radiation Protection), "Relative Biological Effectiveness (RBE), Quality Factor (Q), and Radiation Weighting Factor (wR)," tech. rep., 2003.

[39] J. M. Søbstad, "Monte carlo based comparison of constant vs. variable rbe for proton therapy patients," 2017.

[40] E. J. Hall and A. J. Giaccia, *Radiobiology for the radiologist*. Hagerstown, Md, 1973.

[41] J. van der Veen, A. Laenen, and S. Nuyts, "Modern radiotherapy techniques versus three-dimensional conformal radiotherapy for head and neck cancer," *The Cochrane Database of Systematic Reviews*, vol. 2017, December 2017.

[42] B. Urbański, "The future of Radiation Oncology: Considerations of Young Medical Doctor," *Reports of practical oncology and radiotherapy: journal of Greatpoland Cancer Center in Poznan and Polish Society of Radiation Oncology*, vol. 17, pp. 288–293, oct 2012.

[43] S. Vatnitsky and E. Rosenblatt, *Transition from 2-D radiotherapy to 3-D conformal and intensity modulated radiotherapy.* International Atomic Energy Agency, 2008.

[44] A. C. Hartford *et al.*, "American College of Radiology (ACR) and American Society for Radiation Oncology (ASTRO) - Practice Guideline for Intensity-modulated Radiation Therapy (IMRT).," *American journal of clinical oncology*, vol. 35, pp. 612–617, December 2012.

[45] J. a. R. Sveistrup *et al.*, "Improvement in toxicity in high risk prostate cancer patients treated with image-guided intensity-modulated radiotherapy compared to 3d conformal radiotherapy without daily image guidance," *Radiation Oncology*, vol. 9, no. 44, 2014.

[46] "About arrhythmia - American Heart Association page," Accessed March 24, 2022. Available at: `https://www.heart.org/en/health-topics/arrhythmia/about-arrhythmia`.

[47] "Heart arrhythmia - Care at Mayo Clinic - Mayo Clinic page," Accessed March 24, 2022. Available at: `https://www.mayoclinic.org/`.

[48] S. Ebnesajjad, *Expanded PTFE Applications Handbook (1st Ed.).* William Andrew Publishers, 1st ed., 2016.

[49] "Pacemaker Insertion | Johns Hopkins Medicine," Accessed March 26, 2022. Available at: `https://www.hopkinsmedicine.org/health/treatment-tests-and-therapies/pacemaker-insertion`.

[50] M. D. Falco *et al.*, "A randomized in vitro evaluation of transient and permanent cardiac implantable electronic device malfunctions following direct exposure up to 10Gy," *Strahlentherapie und Onkologie*, vol. 197, pp. 198–208, 3 2021.

[51] M. Zecchin *et al.*, "Malfunction of cardiac devices after radiotherapy without direct exposure to ionizing radiation: Mechanisms and experimental data," *Europace*, vol. 18, pp. 288–293, 2 2016.

[52] F. Rodriguez *et al.*, "Radiation-Induced Effects in Multiprogrammable Pacemakers and Implantable Defibrillators," *Radiation oncology treatments, PACE*, vol. 14, 1991.

[53] C. Ferrante, "Study of Neutron-induced Damage to Cardiac Implantable Electronic Devices in Radiation Therapy," Master's thesis, A.A. 2019-2020.

[54] "Phoenix web page," Accessed March 24, 2022. Available at: `https://phoenixwi.com/neutron-radiography/`.

[55] "Neutron reference radiations fields — Part 1: Characteristics and methods of production," tech. rep., ISO (International Standardization Organization) - Reference Neutron Radiations, 2021.

[56] T. P. Wangler, *RF Linear Accelerators, 2nd edition.* John Wiley Sons, Ltd, 2008.

[57] R. WidERöe, "Über ein neues prinzip zur herstellung hoher spannungen," *Archiv für Elektrotechnik*, vol. 21, pp. 387–406, 7 1928.

[58] M. Chodorow, E. Ginzton, W. Hansen, R. Kyhl, R. Neal, W. Panofsky, and T. STAFF, "Stanford high-energy linear electron accelerator (mark iii)," *Review of Scientific Instruments*, vol. 26, no. 2, pp. 134–204, 1955.

[59] J. Matney, "High Energy X-ray Generators: Linear Accelerators," Accessed April 1, 2022. Available at: `https://ccah.vetmed.ucdavis.edu/sites/g/files/dgvnsk4586/files/local_resources/pdfs/rad-onc-matney-x-ray-generators.pdf`.

[60] "Elekta web page," Accessed March 31, 2022. Available at: `https://www.elekta.com/products/radiation-therapy/`.

[61] E. B. Podgoršak, *Particle Accelerators in Medicine*, pp. 1041–1099. Berlin, Heidelberg: Springer Berlin Heidelberg, 2014.

[62] F. M. Khan, *The physics of radiation therapy.* Lippincott Williams Wilkins, 2003.

[63] H. Romeijn *et al.*, "A column generation approach to radiation therapy treatment planning using aperture modulation," *SIAM Journal on Optimization*, vol. 15, pp. 838–862, 01 2005.

[64] L. Quintieri, R. Bedogni, B. Buonomo, A. Esposito, M. D. Giorgi, G. Mazzitelli, P. Valente, and J. M. Goméz-Ros, "Photoneutron source by high energy electrons on high z target: Comparison between monte carlo codes and experimental data," *TRANSACTIONS OF FUSION SCIENCE AND TECHNOLOGY*, vol. 61, 2012.

[65] "A review on photoneutrons characteristics in radiation therapy with high-energy photon beams," *Reports of Practical Oncology and Radiotherapy*, vol. 15, pp. 138–144, 2010.

[66] A. Zanini *et al.*, "Neutron spectra in a tissue equivalent phantom during photon radiotherapy treatment by linacs," *Radiation Protection Dosimetry*, vol. 110, pp. 157–160, 2004.

[67] A. Alem-Bezoubiri *et al.*, "Monte Carlo estimation of photoneutrons spectra and dose equivalent around an 18MV medical linear accelerator," *Radiation Physics and Chemistry*, vol. 97, pp. 381–392, 4 2014.

[68] *Radiation Protection in the Design of Radiotherapy Facilities.* No. 47 in Safety Reports Series, Vienna: INTERNATIONAL ATOMIC ENERGY AGENCY, 2006.

[69] C. Richmond, "ICRP Publication 23," *International Journal of Radiation Biology and Related Studies in Physics, Chemistry and Medicine*, vol. 48, no. 2, pp. 285–285, 1985.

[70] A. Di Fulvio, L. Tana, M. Caresana, E. D'Agostino, M. de San Pedro, C. Domingo, and F. d'Errico, "Clinical simulations of prostate radiotherapy using bomab-like phantoms: Results for neutrons," *Radiation Measurements*, vol. 57, pp. 48–61, 2013. Proceedings of the Workshop: Dosimetry for Second Cancer Risk Estimation EURADOS Annual Meeting Vienna 2012.

[71] L. Tommasino and K. Harrison, "Damage track detectors for neutron dosimetry: I. registration and counting methods," *Radiation Protection Dosimetry*, vol. 10, pp. 207–217, 01 1985.

[72] R. Fleischer, P. Buford Price, and R. M. Walker, *Nuclear tracks in solids: Principles and Applications.* University of California Press, 1975.

[73] D. Nikezic and K. N. Yu, "Formation and growth of tracks in nuclear track materials," *Materials Science and Engineering R: Reports*, vol. 46, pp. 51–123, 12 2004.

[74] M. Caresana, M. Ferrarini, L. Garlati, and A. Parravicini, "About ageing and fading of CR-39 PADC track detectors used as air radon concentration measurement devices," *Radiation Measurements*, vol. 45, no. 2, pp. 183–189, 2010.

[75] "Politrack® - strumenti per la misura del Radon," Accessed April 10, 2022. Available at: `https://miam.it/prodotti/politrack/`.

[76] "Politrack® user manual - Version 6.5," June 2019.

[77] M. Caresana, M. Ferrarini, and A. Parravicini, "Analisi Morfologica delle Tracce nucleari su rivelatori CR-39," AIRP – Atti del Convegno Nazionale di Radioprotezione "Cinquantenario AIRP: Storia e Prospettive della Radioprotezione", 6 June 2008.

[78] C. J. Werner *et al.*, *MCNP Users Manual - Code Version 6.2.* Los Alamos National Security, LLC, 2017.

[79] I. M. Frankl, *Variance Reduction in Calculations of Non-Target Photon and Neutron Doses from High Energy Photon Beam Radiation Therapy via Monte Carlo Simulations.* PhD thesis, Technische Universität München, 2018.

[80] C. H. Choi *et al.*, "Monte Carlo simulation of neutron dose equivalent by photoneutron production inside the primary barriers of a radiotherapy vault," *Physica Medica*, vol. 48, pp. 1–5, 4 2018.

List of Figures